FACULTY OF ENGINEERING AND ARCHITECTURE

# Computational Biomechanics Modeling of the Cerebrospinal Fluid: Model Development and Application to Chiari Type 1 Malformation

**Sarah Vandenbulcke**

Doctoral dissertation submitted to obtain the academic degree of
Doctor of Biomedical Engineering

**Supervisors**

Prof. Patrick Segers, PhD* - Prof. Joris Degroote, PhD**

* Department of Electronics and Information Systems
Faculty of Engineering and Architecture, Ghent University

** Department of Electromechanical, Systems and Metal Engineering
Faculty of Engineering and Architecture, Ghent University

August 2024

GHENT UNIVERSITY

ISBN 978-94-6355-864-8
NUR 954
Wettelijk depot: D/2024/10.500/69

## Members of the Examination Board

### Chair

Prof. Sabine Wittevrongel, PhD, Ghent University

### Other members entitled to vote

Prof. Edward Baert, PhD, Ghent University
Prof. Bryn Martin, PhD, University of Idaho, USA
Selene Pirola, PhD, Technische Universiteit Delft, the Netherlands
Soroush Safaei, PhD, Ghent University

### Supervisors

Prof. Patrick Segers, PhD, Ghent University
Prof. Joris Degroote, PhD, Ghent University

# Preface

The seed for pursuing a PhD in cerebrospinal fluid modeling was planted during a meeting with Patrick in April 2019. Between the topics on cardiovascular and lymphatic modeling, Patrick brought up this neurological disorder characterized by brain tissue descending into the vertebral column and he mentioned that researchers of the UZ Ghent neurosurgery department had proposed a novel hypothesis about this disorder. This topic directly caught my attention, leading to a second meeting where Frank Dewaele and Tim De Pauw explained their novel hypothesis linking sudden actions to fluid accumulation in the spinal cord, with cerebrospinal fluid playing a vital role. It was this second meeting that convinced me to pursue a PhD in this topic. I was motivated to understand the complexity of the system better and advance my understanding of computational biomechanics. That was how cerebrospinal fluid, previously just one of many components of the brain anatomy, became a central part of my life over the past five years.

First, I would like to thank the members of my thesis committee for reading my dissertation, providing valuable feedback, and asking insightful questions. I would not describe my PhD journey as a bike trip on some flat (Belgian) planes, but rather a challenging mountain climb, with some steep middle sections. While those steeper sections were not always easy to conquer, I am glad that I embraced these challenges as the views from a mountain top are (in my opinion) far more breathtaking than those from a flat landscape. In overcoming these steeper sections, a number of people played an essential role. First, I would like to express my gratitude to my two supervisors **Professor Patrick Segers** and **Professor Joris Degroote** for their continuous feedback and support allowing me to keep improving and ask the right questions. It was **Patrick** who first told me about Chiari type 1 malformation and the interesting new hypothesis and in that way convinced me to start a PhD at BioMMedA. I want to thank **Patrick** for giving me the opportunity to work on this fascinating topic and

for continuing to support me on the way. With the development of complex models also came the challenges of successfully implementing them. I want to thank **Joris** for brainstorming and giving me excellent advice when setting up these models.

The topic of my PhD was not only numerically challenging but also involved modeling a highly complex system. Therefore, the clinical input of **Professor Frank Dewaele** and **Tim De Pauw** has been crucial right from the start of my PhD. The numerous brainstorming sessions with **Tim** helped me to understand the complex mechanisms governing cerebrospinal fluid dynamics and make adequate modeling choices. I also want to acknowledge them for initiating this research and presenting their novel hypothesis. Furthermore, I would like to thank **Dr. Soroush Safaei** for being the catalyst for my research stay at the Auckland Bioengineering Institute in New Zealand and for introducing me to the researchers of M$\bar{a}$tai Medical Research Institute. I want to especially thank **Professor Samantha Holdsworth**, **Paul Condron**, and **Dr. Haribalan Kumar** for their hospitality and help during and after my stay in Gisborne, which has been critical when transforming simplified models into subject-specific models. I extend my thanks to the colleagues at the Auckland Bioengineering Institute for the insightful discussions and the (adventurous) trips in and around Auckland. My thanks should also go to **Professor Charlotte Debbaut** for her practical advice and her role in facilitating the exchange to Auckland. In addition, I wish to acknowledge **Dr. Henri Dolfen** for brainstorming and his help when implementing ventricular wall motion.

Throughout my PhD, I relied on several people who supported me and helped me to keep going. I was lucky to do my PhD in a group of great colleagues that even made the grey block B a unique and warm working environment. I valued a lot the open door of **Saskia**'s office and the help of **Jurgen** with a wide range of technical and computer problems. Furthermore, I want to thank my PhD-long office mates, **Amith** for his advice and numerous brainstorming sessions that helped me to unravel the great mysteries of Fluent and the HPC, and **Lise** for always being a bit of a mentor to me throughout the PhD trajectory. I also want to thank **Simeon** for 'willingly' accepting the office window policy and **Jellis** for making our former block B office a bit greener in the last months. I also appreciated co-supervising with the always in a good mood and extremely helpful, **Matthias**, and guiding 'Modelleren, Maken, en Meten' together with **Lise**, **Simeon**, **Saar**, and **Tim**. **Saar** also made a great (cheerful) companion during our research stay in New Zealand. Moreover,

I want to extend my gratitude to all current and past BioMMedA and MEDISIP colleagues for the nice lunch conversations, afterworks and the random talks in the hallway. I will not easily forget the greasy pizza and the for some people (guess who) too long walk in the Rocky Mountains, the wandering around of **Yousof**, **Hooman** and **Wouter**'s more and less subtle sense of humor, the occasional lunches with the restaurant gang, **Samaneh**'s directness, **Annette**'s useful suggestions, **Mohammad**'s 'Goede morgen', the hallway talks with **Ashkan**, **Paulo**'s enthusiasm, **Bhawna**'s 'short' travel times, **Jolan** and **Tim**'s weird questions, **Emma**'s British accent, **Amir**'s two minutes when going for sandwiches, **Carlos** asking to turn on his computer, and sharing a kayak with **Jens** and then loosing against team **Maya**. A special acknowledgment should also go to **Melissa** for her support and for bringing a real Austrian cowbell, and **Ghazal** and **Federico** for the valuable advice that they gave at the beginning of my PhD that guided me in the right direction. In the last year, we did not only move to new building(s), but also multiple new colleagues joined the lab, each of them bringing a fresh wind to the office. It was a pleasure to meet **Ariana**, **Bea**, **Elias**, **Jessie**, **Jellis**, **Nicole**, **Sina**, **Boris**, **Rabia** and **Zoé** and I wish them the best of luck for the rest of their PhD/Postdoc.

Finally, I would like to extend my thanks to anyone who I might not have named here but who has contributed to this research or just has been great company in the past five years. Een speciale bedanking moet wel nog gaan naar mijn naaste familie die een belangrijke rol hebben gespeeld om dit doctoraat tot een goed einde te brengen. Ik wil zeker mijn ouders en broer Frederik bedanken omdat een weekend 'thuis' door hen altijd zeer relaxerend was en mijn grootouders voor hun interesse in mijn onderzoek. Belangrijk is dat hun interesse me heeft geleerd mijn onderzoek op een begrijpelijke manier uit te leggen. Ten slotte wil ik mijn zus Caroline bedanken voor haar to the point feedback op mijn teksten en presentaties en mij te motiveren om moeilijke uitdagingen niet uit de weg te gaan.

# Table of contents

# Abbreviations and symbols

The following list summarizes the most commonly used abbreviations and symbols in this dissertation.

## Abbreviations

| | |
|---|---|
| 0D | Zero-dimensional |
| 1D | One-dimensional |
| 2D | Two-dimensional |
| 3D | Three-dimensional |
| 4D | Four-dimensional |
| Al | Cerebral arterioles |
| aMRI | Amplified MRI |
| av | Arachnoid villi |
| C2 | Level of the second cervical vertebra |
| CFD | Computational fluid dynamics |
| CMI | Chiari type 1 malformation |
| Cp | Cerebral capillaries |
| CSF | Cerebrospinal fluid |
| DENSE | Displacement Encoding with Stimulated Echoes |
| FL | Foramina of Luschka |
| FM | Foramen of Magendie |
| FSI | Fluid structure interaction |
| ICP | Intracranial pressure |
| int | Interstitium |
| LV | Lateral ventricles |
| lym | Lymphatic |
| MR | Magnetic resonance |
| MRI | Magnetic resonance imaging |
| PC | Phase-Contrast |
| PC-MRI | Phase-Contrast Magentic Resonance Imaging |
| Pss | Sagittal sinus pressure |
| sp | Spinal |

| | |
|---|---|
| SAS | Subarachnoid space |
| SSS | Superior sagittal venous sinus |
| TBI | Traumatic brain injury |
| UDF | User-defined function |
| V3 | Third ventricle |
| V4 | Fourth ventricle |

## Symbols

| | |
|---|---|
| $\alpha$ | Permeability $[1/m^2]$ |
| $\overrightarrow{a}$ | Acceleration vector $[m/s^2]$ |
| $A$ | Cross-sectional area $[m^2]$ |
| $A_{csas}$ | Cross-sectional area of cranial subarachnoid space inlet $[m^2]$ |
| $A_{lv}$ | Cross-sectional area of the lateral ventricles inlet $[m^2]$ |
| $A_{v4}$ | Cross-sectional area of fourth ventricle inlet $[m^2]$ |
| $C$ | CSF compliance $[ml/mmHg]$ |
| $C_{av}$ | Compliance of the arachnoid villi outlet $[ml/mmHg]$ |
| $c_i$ | Contribution of outlet i to total compliance [%] |
| $C_i$ | Compliance of outlet i $[ml/mmHg]$ |
| $C_{int}$ | Compliance of the interstitium outlet $[ml/mmHg]$ |
| $C_{lym}$ | Compliance of the lymphatic outlet $[ml/mmHg]$ |
| $C_{sp}$ | Compliance of the spinal outlet $[ml/mmHg]$ |
| $C_{tot}$ | Total compliance $[ml/mmHg]$ |
| $Cl^-$ | Chloride-ion |
| $d$ | Length of porous zone $[m]$ |
| $\delta$ | Pressure perturbation $[Pa]$ |
| $\Delta t$ | Timestep size $[s]$ |
| $dP$ | Pressure difference $[mmHg]$ |
| $dP_{min-max}$ | Pressure difference $[mmHg]$ |
| $dP_{OBS}$ | Peak pressure difference for cases with obstruction $[mmHg]$ |
| $dP_{control}$ | Peak pressure difference for control case $[mmHg]$ |
| $dt$ | Timestep difference $[s]$ |
| $\overrightarrow{f}$ | Body forces acting on fluid volume $[N/kg]$ |
| $\overrightarrow{F}$ | Forces acting on a fluid volume $[N]$ |
| $f_{arterial}$ | Arterial frequency $[1/s]$ |
| $f_{venous1}$ | Venous frequency $[1/s]$ |
| $\overrightarrow{g}$ | Gravitational acceleration $[m/s^2]$ |
| $I2$ | Inertia component of CSF flow $[kgm^2]$ |
| $ICP_{avg}$ | Average intracranial pressure $[mmHg]$ |

| | |
|---|---|
| $[J]$ | Jacobian matrix of flow over pressure differentials $[ml/s/mmHg]$ |
| $k$ | Coupling iteration counter |
| $K^+$ | Potassium-ion |
| $m$ | Mass $[kg]$ |
| $\mu$ | Dynamic viscosity $[kg/m/s]$ |
| $\mu_n$ | Mean value of negative Gaussian peak $[s]$ |
| $\mu_p$ | Mean value of positive Gaussian peak $[s]$ |
| $n$ | Timestep counter |
| $Na^+$ | Sodium-ion |
| $p$ | Pressure imposed by surrounding fluid $[Pa]$ |
| $P$ | pressure $[mmHg]$ |
| $P_{ext}$ | External pressure $[mmHg]$ |
| $P_i$ | Pressure at outlet i $[mmHg]$ |
| $P_{i,k}$ | Pressure at outlet i for timestep n and coupling iteration k $[ml/s]$ |
| $P_{i,k-1}$ | Pressure at outlet i for timestep n and coupling iteration k-1 $[ml/s]$ |
| $P_{i,n}$ | Pressure at outlet i for timestep n $[mmHg]$ |
| $P_{i,n-1}$ | Pressure at outlet i for timestep n-1 $[mmHg]$ |
| $P_{mean}$ | Mean intracranial pressure $[mmHg]$ |
| $P_n$ | Pressure at timestep n $[mmHg]$ |
| $P_{n-1}$ | Pressure at timestep n-1 $[mmHg]$ |
| $Q$ | Volumetric flow rate $[ml/s]$ |
| $Q_{aq}$ | Flow through the cerebral aqueduct $[ml/s]$ |
| $Q_{arterial1}$ | Amplitude of inflow lateral ventricles $[ml/s]$ |
| $Q_{arterial2}$ | Amplitude of inflow basilar artery region $[ml/s]$ |
| $Q_{basilar}$ | Flow induced by volume changes at the anterior side of the brainstem $[ml/s]$ |
| $Q_c$ | Targeted amplitude of flow through spinal subarachnoid space $[ml/s]$ |
| $q_i$ | Percentage of the total net outflow passing through the outlet i [%] |
| $Q_i$ | Flow rate through outlet i $[ml/s]$ |
| $Q_{i,k}$ | Flow rate through outlet i for timestep n and coupling iteration k $[ml/s]$ |
| $Q_{i,k-1}$ | Flow rate through outlet i for timestep n and coupling iteration k-1 $[ml/s]$ |
| $Q_{i,n}$ | Flow rate through outlet i for timestep n $[ml/s]$ |
| $Q_{in}$ | Inflow in 0D model $[ml/s]$ |
| $Q_{production}$ | Production flow rate $[ml/s]$ |
| $Q_{sas}$ | Flow through the spinal subarachnoid space $[ml/s]$ |

| | |
|---|---|
| $Q_{v3}$ | Targeted amplitude of flow in the third ventricle $[ml/s]$ |
| $Q_{venous1}$ | Amplitude of inflow occipital region $[ml/s]$ |
| $r$ | Flow residual of timestep n and coupling iteration k $[ml/s]$ |
| $R$ | CSF absorption resistance $[mmHg.s/ml]$ |
| $r_0$ | Flow residual of timestep n and coupling iteration 1 $[ml/s]$ |
| $R_{av}$ | Absorption resistance of arachnoid villi outlet $[mmHg.s/ml]$ |
| $\rho$ | Density $[kg/m^3]$ |
| $R_i$ | Resistance of outlet i $[mmHg.s/ml]$ |
| $R_{int}$ | Absorption resistance of interstitium outlet $[mmHg.s/ml]$ |
| $r_k$ | Flow residual of previous coupling iteration $[ml/s]$ |
| $R_{lym}$ | Absorption resistance of lymphatic outlet $[mmHg.s/ml]$ |
| $R_{sp}$ | Absorption resistance of spinal outlet $[mmHg.s/ml]$ |
| $R_{tot}$ | Total absorption resistance $[mmHg.s/ml]$ |
| $R_{viscous}$ | Viscous resistance of the porous zone $[1/m^2]$ |
| $SA$ | Scaling factor for source term corresponding to a single cough $[kg/m^3s]$ |
| $S_{basilar}$ | Source term imposed in the region anterior to the brainstem $[kg/m^3s]$ |
| $S_{cough}$ | Source term imposed in the spinal canal corresponding to a single cough $[kg/m^3s]$ |
| $\sigma$ | Standard deviation of Gaussian curve $[s]$ |
| $t$ | Time $[s]$ |
| $t_n$ | Time at timestep n $[s]$ |
| $t_{n-1}$ | Time at timestep n-1 $[s]$ |
| $\overrightarrow{\overrightarrow{\tau}}$ | Viscous stress tensor $[Pa]$ |
| $u$ | X-component of velocity $[m/s]$ |
| $v$ | Y-component of velocity $[m/s]$ |
| $\overrightarrow{v}$ | velocity vector $[m/s]$ |
| $V$ | Volume $[ml]$ |
| $V_{basilar}$ | Volume of the region anterior to the brainstem $[m^3/s]$ |
| $v_{csas}$ | Flow velocity at cranial subarachnoid space inlet $[m/s]$ |
| $v_{lv}$ | Flow velocity at the lateral ventricles inlet $[m/s]$ |
| $V_n$ | Volume at timestep n $[ml]$ |
| $V_{n-1}$ | Volume at timestep n-1 $[ml]$ |
| $v_{production}$ | Flow velocity at the choroid plexus inlet (= production site) $[m/s]$ |
| $v_{v4}$ | Flow velocity at the fourth ventricle inlet $[m/s]$ |
| $w$ | Z-component of velocity $[m/s]$ |

# Summary


## Introduction

Cerebrospinal fluid (CSF) surrounds and closely interacts with the neural tissues of the brain and spinal cord. Cardiac pulsations, breathing, and physical actions such as posture changes or coughing are responsible for the movement of this fluid. Rapid CSF displacement during coughing is without harm in healthy subjects but is thought to lay at the origin of spinal cord damage in patients with Chiari type 1 malformation. This research aims to advance our understanding of CSF dynamics and unravel the impact of coughing on CSF dynamics in patients with Chiari type 1 malformation. Computational fluid dynamics (CFD) models are suitable tools for investigating CSF dynamics because of their ability to simulate fluid flow in complex fluid spaces and to easily introduce input and domain changes. The overall objectives of this research are:

**Objective 1**: Development of computational biomechanics models to simulate physiological pressures and velocities within the anatomical CSF spaces

**Objective 2**: Application of the computational models to assess the impact of coughing in Chiari type 1 malformation

## Part I: Cerebrospinal fluid physiology and modeling

### Chapter 1: CSF in the central nervous system

CSF is situated in the subarachnoid space (SAS) lined by the pia and arachnoid mater, the ventricles in the brain, and the central canal in the spinal cord. These spaces are all interconnected. The dynamical behavior of CSF is determined by its turnover (production and absorption), and mechanical interaction with venous volumes, arterial volumes, and the surrounding soft tissues. Each of these processes is responsible for the regulation of CSF pressure and flow, with blood

and soft tissue volumes either inducing displacements or providing buffering. Chiari type 1 malformation is a neurological disorder where the normal flow of CSF is partially obstructed at the level of the skull base. Chiari type 1 malformation often appears together with syringomyelia, a neurological disorder characterized by fluid accumulation in the spinal cord. Nevertheless, the exact link between the two disorders is not understood. Multiple studies have aimed to reveal the mechanism between these two disorders through in vivo investigation, which is challenging because of the difficult accessibility of CSF spaces and the limited spatial and/or temporal resolution of intracranial pressure recordings and magnetic resonance imaging (MRI). Another way to study CSF dynamics is through computational modeling.

**Chapter 2: State-of-art in computational modeling of CSF dynamics**

Computational models have been widely used to study CSF dynamics and can be divided into three main groups: lumped parameter (0D) models, simplified 1D and 2D axisymmetric models of the spine, and subject-specific 3D models. 3D models allow capturing CSF flows in the complex cranial (and spinal) CSF spaces and CFD models have demonstrated their use among others for the analysis of central nervous system drug delivery and Chiari type 1 malformation. The implementation of boundary conditions in these models is diverse, and currently, no standard approach exists for modeling CSF dynamics. Where CFD models have combined the intracranial and spinal CSF flow, they only provided information regarding spatial pressure differences and a system-wide approach has not been applied to study Chiari type 1 malformation.

Part II: Computational fluid dynamics models of the cerebrospinal fluid

**Chapter 3: Implementing physiological boundary conditions**

This chapter presents the setup of a CFD model to simulate CSF dynamics. In this model, fluid pressures and flows were simulated within the 3D cranial and upper spinal CSF space through the implementation of boundary conditions mimicking CSF production, absorption, and the effects of arterial pulsations, breathing, and buffering. Where CSF production was considered constant, venous and arterial volume changes were imposed as simplified sinusoidal inflows

and source terms. Windkessel boundary conditions were imposed at the outlets to model absorption and buffering and the corresponding resistance and compliance parameters were tuned using a 0D model. This approach yielded CSF pressures and velocities within the physiological range and enabled the evaluation of the impact of the magnitude and distribution of compliance. We found that the magnitude of the total compliance determined the amplitude of pressure pulsations, whereas the distribution of compliance defined the amount of buffering by each of the outlets.

**Chapter 4: Implementing amplified MRI acquired motion**

In this chapter, we evaluated the use of an amplified MRI (aMRI) dataset, which contains information about the non-uniform motion of the ventricular surfaces, to more accurately predict physiological CSF dynamics in a CFD model. To this end, we deduced the amplified deformations of the cerebral ventricles from aMRI and used these deformations as inputs for our CFD model. We compared the resulting flow rates with those obtained with phase-contrast (PC) MRI measurements in the cerebral aqueduct and found a similar pulsatile behavior with dominantly caudal flow in the first half of the cardiac cycle and cranial flow in the second half. However, the comparison of aMRI and PC-MRI measurements was not trivial because the derived aMRI flow rates were subject to noise. Nevertheless, this study demonstrated the feasibility of using aMRI motion in CFD models and motivates the application of the presented approach to multiple subjects in future work.

Part III: Application of computational fluid dynamics models to study Chiari type 1 malformation

**Chapter 5: Modeling Chiari type 1 malformation as a porous zone obstruction**

In this chapter, we evaluated whether changing the permeability of a porous zone adequately captures the pressure differences induced by Chiari type 1 malformation. Therefore, we compared pressure differences for three different porous zones occupying only the posterior side (OBS-1) and both sides (OBS-2 and OBS-3) of the spinal SAS with those for four physical obstructions. We found peak pressures in the same range between OBS-1 and 70 % obstruction, OBS-2 and 91 % obstruction, and OBS-3 and 99 % obstruction. This also gave an indication to which area of obstruction each of these porous zones corresponded. However, the pressure-flow relationship was found to

be more linear when introducing a posterior and anterior porous zone compared to the matching physical obstruction.

**Chapter 6: Studying the effects of coughing on CSF dynamics in Chiari type 1 malformation**

In this chapter, the model presented in chapter 3 was updated based on a comprehensive dataset containing anatomical images and subject-specific PC-MRI flow measurements. These flow measurements were actively used when calibrating the inputs and parameters of the outlet boundary conditions. In this updated model, we evaluated the effects on pressure and pressure distribution of a single cough, three levels of obstruction, and a reduced spinal compliance. The most severe obstruction, corresponding to 99 % obstruction, induced a decoupling between the spinal and intracranial compartments, with as a consequence an elevation of the amplitude of the intracranial pressure pulsations. We also found that the obstructions and the reduction of the spinal compliance caused a larger increase in pressure difference between the spinal and intracranial compartment during coughing than during the arterial peak flow. This indicated that the combination of an obstruction, coughing, and a reduced compliance caused the highest elevation of pressure differences, which might be critical for spinal cord damage.

Part VI: Conclusion

**Chapter 7: Conclusion and outlook**

The aim of this research was to quantitatively assess the impact of Chiari type 1 malformation on CSF dynamics. Therefore, we developed a CFD modeling framework to simulate CSF dynamics through the implementation of boundary conditions based on physiological CSF production, absorption, buffering, and effects of arterial, venous, and tissue volume changes. For implementing tissue volume changes, we explored the use of PC-MRI and aMRI-based inputs. The modeling approach presented in chapter 3 allowed us to not only model relative pressures but also absolute pressures, making the model suitable for studying neurological disorders where intracranial pressure is implicated. In this framework, we introduced Chiari type 1 malformation and found that the physical changes in Chiari type 1 malformation have a greater impact on pressure distribution during coughing than during arterial peak flows. The results also emphasized the importance of considering distributed

compliance in computational models, which is an important improvement over previous CFD models. This research demonstrated the value of incorporating in vivo MRI measurements and lumped parameter models in subject-specific 3D models. Meanwhile, further validation and evaluation of the sensitivity of the input parameters should be the focus of future work.

# Samenvatting

## Introductie

Cerebrospinaal vocht of hersenvocht (CSF) omringt en heeft een nauwe interactie met de neurale weefsels van de hersenen en het ruggenmerg. Hartpulsaties, ademhaling en fysieke handelingen zoals houdingsveranderingen of hoesten zijn verantwoordelijk voor de beweging van deze vloeistof. Snelle CSF-verplaatsingen tijdens hoesten zijn niet schadelijk bij gezonde mensen, maar zouden aan de basis liggen van ruggenmergschade bij patiënten met Chiari type 1 malformatie. Dit onderzoek heeft als doel onze kennis van de CSF-dynamiek te vergroten en de invloed van hoesten op de CSF-dynamiek bij patiënten met Chiari type 1 malformatie te ontrafelen. Computationele vloeistofdynamica (CFD) modellen zijn geschikt om de CSF-dynamiek te onderzoeken vanwege hun vermogen om vloeistofstromingen in complexe vloeistofruimtes te simuleren en eenvoudig input- en domeinveranderingen te introduceren. De algemene doelstellingen van dit onderzoek zijn:

**Doelstelling 1**: Ontwikkeling van computationele biomechanicamodellen om fysiologische drukken en snelheden binnen de anatomische CSF ruimtes te simuleren

**Doelstelling 2**: Toepassing van computationele modellen om de impact van hoesten bij Chiari type 1 malformatie te onderzoeken

## Deel I: Fysiologie en modellering van het cerebrospinaal vocht

### Hoofdstuk 1: CSF in het centraal zenuwstelsel

CSF bevindt zich in de subarachnoïdale ruimte, die wordt omgeven door de pia mater en de arachnoïdea, de ventrikels in de hersenen en het centraal kanaal in het ruggenmerg. Deze ruimtes zijn allemaal met elkaar verbonden. Het dynamische gedrag van CSF wordt bepaald door de CSF-productie, absorptie en de mechanische interactie

van CSF met veneuze volumes, arteriële volumes en de omliggende zachte weefsels. Elk proces is verantwoordelijk voor de regulatie van de drukken en stroming van deze vloeistof, waarbij de bloedvolumes en zachte weefsels ofwel verplaatsingen veroorzaken ofwel buffering bieden. Chiari type 1 malformatie is een neurologische aandoening waarbij de normale stroming van CSF gedeeltelijk belemmerd wordt ter hoogte van de schedelbasis. Chiari type 1 malformatie komt vaak samen voor met syringomyelie, een neurologische aandoening die gekenmerkt is door vochtophoping in het ruggenmerg. Het precieze verband tussen deze twee aandoeningen is echter onbekend. Meerdere studies hebben geprobeerd het mechanisme tussen deze twee aandoeningen te onthullen door in vivo onderzoek, wat een uitdaging is vanwege de moeilijke toegankelijkheid van de CSF-ruimtes en de beperkte resolutie in ruimte en/of tijd van intracraniële drukmetingen en MRI-metingen. Een andere manier om de vloeistofdynamica van het CSF te bestuderen is door middel van computermodellen.

**Hoofdstuk 2: State-of-art in computationele modellering van CSF-dynamica**

Computationele modellen worden vaak gebruikt om de CSF-dynamica te bestuderen en kunnen worden onderverdeeld in drie groepen: 0D modellen, vereenvoudigde 1D en 2D axisymmetrische modellen van de spinale CSF-ruimtes, en patiënt-specifieke 3D modellen. 3D-modellen maken het mogelijk om CSF-stromingen in de complexe intracraniale (en spinale) CSF-ruimtes te simuleren en CFD-modellen zijn in het verleden gebruikt voor de analyse van geneesmiddelentoediening in het centrale zenuwstelsel en het bestuderen van Chiari type 1 malformatie. De implementatie van randvoorwaarden in deze modellen is divers en momenteel bestaat er geen standaardaanpak voor het modelleren van de 3D CSF-dynamica. Waar CFD-studies CSF-stroming al zowel in de intracraniële als in spinale ruimtes hebben bestudeerd, gaven ze enkel informatie over ruimtelijke drukverschillen en een systeemwijde aanpak was nog niet toegepast om Chiari type 1 malformatie te bestuderen.

Deel II: Computationele vloeistofdynamica modellen van de cerebrospinale vloeistof

**Hoofdstuk 3: Implementatie van fysiologische randvoorwaarden**

Dit hoofdstuk toont de ontwikkeling van een CFD-model om de CSF-dynamica te simuleren. In dit model werden vloeistofdrukken en

stromingen gesimuleerd binnen de 3D intracraniële en de bovenste spinale CSF-ruimtes door het implementeren van randvoorwaarden die CSF-productie, absorptie en de effecten van arteriële pulsaties, ademhaling en buffering nabootsten. Waar de productie van CSF als constant werd beschouwd, werden veneuze en arteriële volumeveranderingen opgelegd als vereenvoudigde sinusvormige instromen en brontermen. Windketel randvoorwaarden werden opgelegd aan de uitlaten om absorptie en buffering te modelleren en de corresponderende weerstands- en compliantieparameters werden gekalibreerd met behulp van een 0D model. Deze aanpak resulteerde in CSF-drukken en CSF-snelheden binnen het fysiologische interval en maakte het evalueren van de impact van de grootte en verdeling van compliantie mogelijk. We observeerden dat de totale compliantie de amplitude van drukpulsaties bepaalde, terwijl de verdeling van de compliantie de hoeveelheid buffering door elke uitlaat bepaalde.

**Hoofdstuk 4: Implementatie van geamplificeerde beweging gemeten met MRI**

In dit hoofdstuk, evalueerden we het gebruik van MRI-beelden met bewegingsamplificatie (aMRI), die informatie bevatten over de niet-uniforme beweging van de ventrikeloppervlakken, om op een accuratere manier de CSF-dynamieken te voorspellen in een CFD-model. Daarom haalden we vervormingen van de hersenkamers (ventrikels) uit aMRI beelden en gebruikten we deze vervormingen als input voor ons CFD-model. Vervolgens, vergeleken we de aMRI debieten met fase contrast (PC) MRI-debietmetingen in het aquaduct en vonden een vergelijkbaar pulsatiel gedrag met voornamelijk caudale stroming in de eerste helft van de hartcyclus en craniale stroming in de tweede helft. Dit gaf ook aan dat het schalen van de aMRI-beweging nodig was om fysiologische debieten te verkrijgen. Een schaalfactor van 1/8 resulteerde in debieten met dezelfde grootteorde. De vergelijking van aMRI en PC-MRI debietmetingen was echter niet triviaal omdat de afgeleide aMRI-debieten meer onregelmatig waren. Deze studie toonde de haalbaarheid aan van het gebruik van aMRI data in CFD-modellen en motiveert de toepassing van de voorgestelde aanpak op meerdere proefpersonen in toekomstig werk.

## Deel III: Toepassing van computationele vloeistofdynamica modellen om Chiari type 1 malformatie te bestuderen

### Hoofdstuk 5: Modellering van Chiari type 1 malformatie als een poreuze zone obstructie

In dit hoofdstuk evalueerden we of het veranderen van de doorlaatbaarheid van een poreuze zone kan leiden tot drukverschillen in lijn met deze veroorzaakt door Chiari type 1 malformatie. Daarom vergeleken we de drukverschillen voor drie verschillende poreuze zones, die ofwel enkel de achterste zijde (OBS-1) of beide zijden (OBS-2 en OBS-3) van de spinale subarachnoïdale ruimte bezetten, met de drukverschillen ten gevolge van vier fysieke blokkades. We vonden piekdrukken van dezelfde grootteorde tussen OBS-1 en 70 % obstructie, OBS-2 en 91 % obstructie en OBS-3 en 99 % obstructie. Dit gaf ook een indicatie met welke graad van obstructie elke poreuze zone overeenkwam. De druk-debiet verhouding bleek echter meer lineair te zijn bij het introduceren van een poreuze zone aan beide zijden in vergelijking met de overeenkomstige fysieke obstructies.

### Hoofdstuk 6: Onderzoek naar de effecten van hoesten op de CSF-dynamiek bij Chiari type 1 malformatie

In dit hoofdstuk werd het in hoofdstuk 3 gepresenteerde model geüpdatet op basis van een uitgebreide dataset bestaande uit anatomische beelden en PC-MRI debietmetingen. Deze debietmetingen werden actief gebruikt bij het kalibreren van de parameters die inlaat en uitlaat randvoorwaarden beschreven. In dit bijgewerkte model evalueerden we de effecten op drukken en drukverdeling van een enkele hoest, drie obstructieniveaus en een gereduceerde compliance van het spinale compartiment. De ernstigste obstructie, overeenkomend met 99 % obstructie, leidde tot een ontkoppeling tussen het spinale en intracraniale compartiment, met als gevolg een verhoging van de amplitude van de intracraniële drukpulsaties. We observeerden ook dat de obstructies en de vermindering van de compliantie in het spinale compartiment een grotere toename van het drukverschil tussen het spinale en intracraniale compartiment veroorzaakten tijdens hoesten dan tijdens de arteriële piekstroom. Dit gaf aan dat de combinatie van een obstructie, hoesten en een verminderde compliantie de grootste verhoging van de drukverschillen veroorzaakte. Deze verhoging zou van cruciaal belang kunnen zijn bij de ontwikkeling ruggenmergschade.

## Deel VI: Conclusie

### Hoofdstuk 7: Conclusie and vooruitblik

Het doel van dit onderzoek was om de impact van Chiari type 1 malformatie op de CSF-dynamica kwantitatief te beoordelen. Daarom ontwikkelden we een CFD-modelleringskader om de CSF-dynamieken te simuleren door het implementeren van randvoorwaarden gebaseerd op fysiologische CSF-productie, absorptie, buffering en effecten van arteriële, veneuze en weefsel volumeveranderingen. Voor het implementeren van volumeveranderingen van de weefsels onderzochten we zowel de toepassing van PC-MRI en op aMRI. Met de aanpak die was geïntroduceerd in hoofdstuk 3, konden we niet alleen relatieve drukken modelleren, maar ook absolute drukken, waardoor het model geschikt kan zijn voor het bestuderen van verschillende neurologische aandoeningen waarbij intracraniële drukken een rol spelen. In de resulterende modellen introduceerden we Chiari type 1 malformatie en ontdekten we dat de fysieke veranderingen in Chiari type 1 malformatie een grotere invloed hebben op de drukverdeling tijdens hoesten dan tijdens arteriële piekstromen. De resultaten benadrukten ook het belang van het beschouwen van een verdeelde compliantie in computermodellen, wat een belangrijke verbetering was ten opzichte van eerdere CFD-modellen. Dit onderzoek toonde de meerwaarde aan van het integreren van in vivo MRI-metingen en 0D modellen in patiënt-specifieke 3D-modellen. Toekomstig werk zou zich moeten richten op de verdere validatie en evaluatie van de sensitiviteit van de invoerparameters.

# Introduction

## Motivation

The study of the central nervous system and specifically the brain has sparked the interest of people for centuries. As the control system of our body, the brain steers our actions and shapes our thinking. Healthy brain function requires an environment that is chemically and mechanically stable with controlled pressures, and a sufficient supply of nutrients and the removal of waste products. In keeping this homeostasis, cerebrospinal fluid (CSF) plays a critical role. This clear, water-like fluid surrounds and closely interacts with the neural tissues of the brain and spinal cord. Because of this close interaction, changes in the CSF circulation and/or pressures can directly cause damage and also disturb the equilibrium state necessary to maintain normal neurological functioning [1].

An obstruction of the CSF circulation is characteristic of the neurological disorder Chiari type 1 malformation. In this disorder, the lower part of the cerebellum (cerebellar tonsils) extends through the foramen magnum and in that way partially blocks CSF exchange between the compartments encased by the skull and the vertebral column. Despite being relatively unknown to the general public, Chiari type 1 malformation has a reported incidence of at least 0.4 % on magnetic resonance imaging (MRI) [2]. The most prevalent complications are cough-related headaches, and the development of a secondary disorder in the spinal cord, named syringomyelia [3].

Syringomyelia is characterized by a fluid-filled cavity in the spinal cord. It is syringomyelia that leads to sensory and motor symptoms and can severely impair the quality of life of patients. Despite its reported incidence between 12 and 80 % in patients with Chiari type 1 malformation, the exact mechanism leading to syrinx development in patients with Chiari type 1 malformation is unclear [4]. Interestingly, studies have indicated that daily life actions such as coughing might trigger or aggravate syrinx development and progression [5, 6].

The question we want to answer in this research is how daily life actions such as coughing, which are without harm in healthy subjects, could act as triggers for spinal cord damage in patients with Chiari type 1 malformation. We hypothesize that fluid accumulation in the spinal cord is associated with a significant distortion of the normal CSF pressure distribution and that such distortion might present as large pressure differences across the partial obstruction in patients with Chiari type 1 malformation. Hence, to understand how coughing might act as a trigger we investigate how CSF pressure and pressure differences change in patients with Chiari type 1 malformation compared to healthy subjects.

One way to evaluate CSF pressure is through in vivo measurements. This is, however, challenging because of the difficult accessibility of the complex CSF spaces, which are encased by the vertebral column and the skull. Measuring pressure in vivo requires inserting a physical measurement device, making acquisition invasive and limited to a discrete number of locations [7]. In contrast, non-invasive measurement of CSF velocities is possible using MRI. However, none of the currently available MRI techniques provide information about pressure, and besides being an expensive technique the MRI outputs are constrained by the spatial and temporal resolution of MRI [8]. On the other hand, MRI measurements are ideal inputs for setting up and validating computational fluid dynamics (CFD) models.

CFD models have been widely used as tools to study CSF dynamics both in healthy subjects and patients [9]. CFD models make suitable tools for studying CSF dynamics because they allow simulating fluid flow in complex fluid spaces and are adaptable with introduction and/or removal of inputs and domain changes. In these models, we can either directly impose in vivo flow measurements or implement the actual processes impacting CSF dynamics as inputs. These processes include CSF production, absorption, buffering and blood and tissue volume changes resulting from cardiac pulsations and breathing. By introducing these physiological processes in computational models, we can mimic their physiological variations and evaluate their impact on CSF dynamics with or without domain changes. Hence, such a CFD modeling approach allows us to represent Chiari type 1 malformation as a combination of domain and physiological changes and coughing as an additional physiological process and was therefore selected for answering our research question.

## Research objectives

This research aims to advance our understanding of CSF dynamics and unravel the impact of coughing on CSF dynamics in patients with Chiari type 1 malformation. The overall objectives of this research are:

**Objective 1**: Development of computational biomechanics models to simulate physiological pressures and velocities within the anatomical CSF spaces

**Objective 2**: Application of the computational models to assess the impact of coughing in Chiari type 1 malformation

The first objective involves the setup of CFD models, which provide pressures and velocities in the complex CSF spaces. These pressures and flows should lay in the physiological range and at the same time, the computational models should be adaptable to investigate the impact of changes in physiology (i.e. in patients with Chiari type 1 malformation). While the resulting models have broad applications, we apply them to study Chiari type 1 malformation and therefore implement coughing and the changes characteristic of Chiari type 1 malformation.

## Outline of the dissertation

The dissertation is subdivided into five main parts.

Part I provides the general background necessary to understand the computational modeling studies presented in part II and III. Chapter 1 introduces the general CSF physiology and the implications of Chiari type 1 malformation. In this chapter, we also briefly discuss the general modalities to investigate CSF dynamics. In Chapter 2, the different approaches for modeling CSF are discussed and an overview is provided of the state-of-art in CFD modeling of the CSF.

Part II focuses on the development of CFD models of the CSF and thus the realization of the first objective. In chapter 3, we present the computational framework where CSF velocities and pressures are simulated through the implementation of boundary conditions inspired by physiological processes. We specifically evaluate the impact of the magnitude and distribution of compliance assuming simplified sinusoidal inlet boundary conditions. In chapter 4, we incorporate the

physical displacements of brain tissue and compare the results with those obtained by imposing simplified inflow boundary conditions.

In Part III, we assess the impact of Chiari type 1 malformation to realize the second objective. First, a porous zone approach for modeling the obstruction present in Chiari type 1 is evaluated in a cropped CFD model as discussed in chapter 5. Then, chapter 6 focuses on the impact of coughing in patients with Chiari type 1 malformation. In this chapter, the model presented in chapter 3 was first updated by including a subject-specific geometry and flow measurements. In this model, the effects of coughing and different degrees of obstruction were introduced.

Finally, part IV summarizes the main findings of the research and suggests possible next steps for the future, and part V constitutes the appendices.

## List of publications

### First-author peer-reviewed papers

Vandenbulcke S, Condron P., Dolfen H., Safaei S., Holdsworth S., Degroote J., Segers P., Evaluating amplified MRI as an input for computational fluid dynamics models of the cerebrospinal fluid (in preparation).

Vandenbulcke S, Condron P., Safaei S., Holdsworth S., Degroote J., Segers P., A computational fluid dynamics study to assess the impact of coughing on cerebrospinal fluid dynamics in Chiari type 1 malformation, *Scientific Reports*, vol. 14, no. 1, 2024.

Vandenbulcke S, De Pauw T, Dewaele F, Degroote J, Segers P., Computational fluid dynamics model to predict the dynamical behavior of the cerebrospinal fluid through implementation of physiological boundary conditions, *Frontiers in Bioengineering and Biotechnology*, vol. 10, 2022.

### Co-author peer-reviewed papers

De Backer, P., Vermijs, S., Van Praet, C., De Visschere, P., Vandenbulcke, S., Mottaran, A., Bravi C., Berquin C., Lambert E., Dautricourt S., Goedertier W., Mottrie A, Debbaut C., Decaestecker, K., A novel three-dimensional planning tool for selective clamping during partial nephrectomy: validation of a perfusion zone algorithm, *EUROPEAN UROLOGY*, vol. 83, no. 5, 2023.

**Conference contributions**

Vandenbulcke, S., Condron, P., Kumar, H., Safaei, S., Holdsworth, S., Degroote, J., and Segers, P. (2023). Computational fluid dynamics study to investigate the impact of sudden physiological actions on cerebrospinal fluid pressure and flow. Podium presentation at the Summer Biomechanics, Bioengineering and Biotransport Conference in Vail, Colorado, USA.

Vandenbulcke, S., Matcovich, P., Van Impe, M., and Segers, P. (2022). Poroelastic models to investigate the impact of cerebrospinal fluid dynamics on mass transport in the spinal cord. Presentation at the 9th World Congress of Biomechanics, Taipei, Taiwan (online).

Vandenbulcke, S., De Pauw, T., Dewaele, F., Degroote, J., and Segers, P. (2022). Impact of physiologically inspired boundary conditions on fluid pressure and flow in a computational fluid dynamics model of the cerebrospinal fluid. Conference proceeding with podium presentation at the 7th international conference on Computational and Mathematical Biomedical Engineering in Milan, Italy.

Vandenbulcke, S., De Pauw, T., Dewaele, F., and Segers, P. (2021). Implementing physiological processes in computational fluid dynamics models of the cerebrospinal fluid. Presentation at the 26th Congress of the European Society of Biomechanics in Milan, Italy (online).

Vandenbulcke, S., De Backer, P., Babin, D., Segers, P., Decaestecker, K., and Debbaut, C. (2019). Development of a planning tool for robot-assisted partial nephrectomy surgery based on 3D reconstructions of kidneys. Poster at the 18th National Day on Biomedical Engineering: Artificial Intelligence in Medicine in Brussels, Belgium.

# I

# Cerebrospinal fluid physiology and modeling

Chapters

Chapter 1

# Cerebrospinal fluid in the central nervous system

Cerebrospinal fluid (CSF) circulates within the intracranial and spinal compartments encased by the skull and the vertebral column. These rigid structures also house the cerebral vasculature and the neural tissues of the brain and spinal cord, making up the central nervous system. In this chapter, we first explore the general anatomy of the central nervous system and introduce the spaces where CSF resides. Then, the role and dynamics of the CSF in the central nervous system are discussed, to end with the clinical significance of CSF in Chiari type 1 malformation.

## 1.1 Anatomy of the central nervous system

### 1.1.1 Brain and spinal cord

The central nervous system corresponds to the brain and spinal cord. The brain consists of the cerebrum, brainstem, and cerebellum with its anatomy depicted in figure 1.1. About 70-80% of the brain's volume is occupied by neurons, the functional units of the nervous system, and glial cells. The remaining space is filled by the cerebral vasculature, the extracellular matrix, and interstitial fluid [10]. Neurons receive signals through short extensions of the cell body, named dendrites, and in turn a single long extension, called the axon, conducts signals from the cell body to another cell. The visual difference

between gray and white matter comes from the organization of the neural tissues with white matter consisting of axons insulated with white myelin sheaths and gray matter being densely packed with cell bodies of the neurons [11].

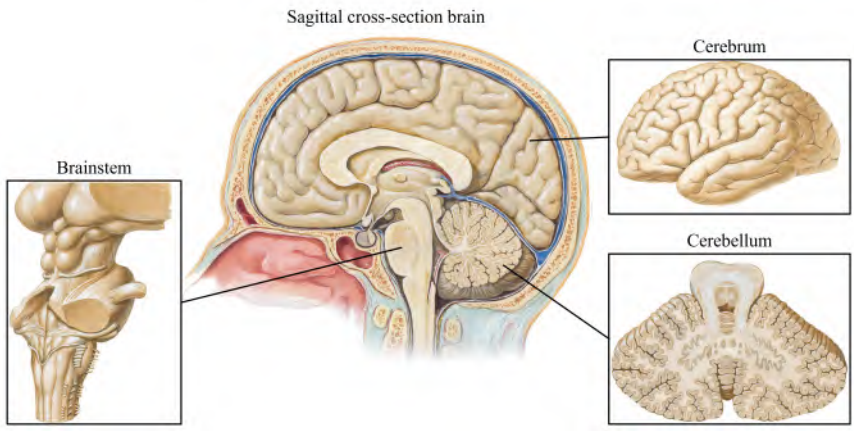


**Figure 1.1:** 3D visualization of the brain anatomy showing the cerebrum, brainstem, and cerebellum. This figure was adapted from Netter et al. [12].

The spinal cord extends from the brainstem through the opening in the base of the skull, the foramen magnum, into the spinal canal surrounded by the vertebral column. Similar to the brain, its tissue is composed of neurons, glial cells, blood vessels, and the extracellular matrix and interstitial fluid in between with neurons organized in gray and white matter regions. The spinal cord anatomy is depicted in figure 1.2.

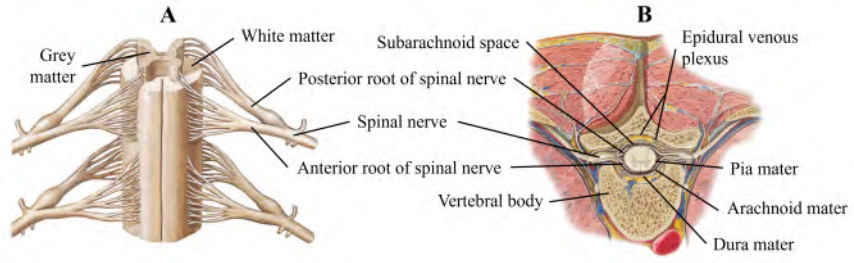


**Figure 1.2:** Spinal cord anatomy with (A) 3D section depicting the gray and white matter of the spinal cord and the spinal nerves and (B) axial section at thorax level. These figures were adapted from Netter et al. [12].

The soft neural tissues of the brain and spinal cord are protected by the rigid skull and the vertebral column composed of intervertebral

discs and vertebrae. A second layer of protection and support is provided by the meninges, which are three membranes containing collagenous and elastic fibers covering and insulating the brain and spinal cord. Figure 1.3 visualizes the locations of these meninges. The outermost membrane is the dura, which is the thickest and strongest membrane. De Kegel et al. reported an average sample thickness of $1.05 \pm 0.22$ mm based on measurement of five post-mortem samples of the intracranial dura mater [13]. The dura is composed of an endosteal dura (becomes periosteum in the spinal compartment) and a meningeal layer (cranial and spinal dura). These layers separate at the level of the dural venous sinuses (e.g. superior sagittal sinus) and below the foramen magnum to form in between the spinal epidural space. Beneath the dura mater the arachnoid and finally pia mater are situated, which are thin and delicate membranes (thickness in the order of $\mu m$ ) with the arachnoid lining the dura and the pia following the spinal cord and the highly convoluted brain surface [14].

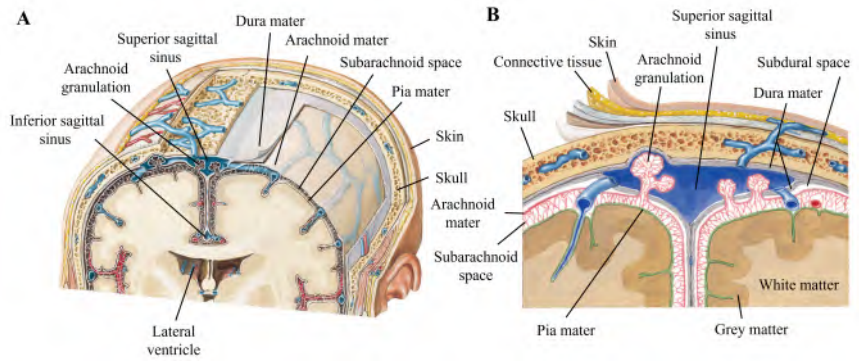


**Figure 1.3:** (A) Coronal view of the head showing a resection of the skull, meninges, and brain and (B) zoomed in on the superior sagittal sinus. These figures were adapted from Netter et al. [12].

### 1.1.2 CSF spaces

Situated between the pia and arachnoid mater is the subarachnoid space (SAS), which is occupied by CSF, blood vessels, and a web-like multitude of trabaculae connecting the pia and arachnoid mater [15, 16]. By following the interior surface of the dura, the arachnoid does not adhere as close to the brain (with grooves and fissures) and spinal cord surface as the pia does. As a result, the thickness of the SAS is not constant, rather the SAS locally enlarges to form cisterns (referred to as CSF pockets) with some of the cisterns depicted in figure 1.4 [17].

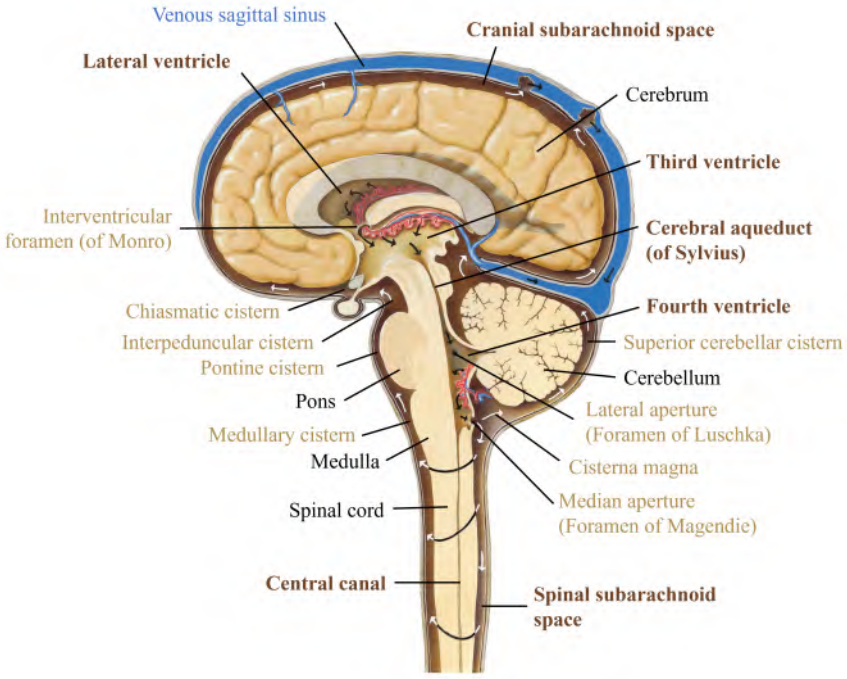


**Figure 1.4:** Sagittal view of the CSF spaces with CSF spaces (light and dark brown), neural tissues (black), and the intracranial veins (blue). CSF spaces include the ventricles, cisterns, foramina, and subarachnoid spaces (cranial and spinal). This figure was adapted from Netter et al. [12].

As shown in figure 1.4, the SAS is connected with the ventricular system, which is a CSF-filled system of four interconnected cavities in the brain, named the ventricles. The two lateral ventricles and the third ventricle are situated in the cerebrum, the largest component of the brain. Each hemisphere has one lateral ventricle connecting via an intraventricular foramen (also called the foramen of Monro) with the narrow third ventricle. The third ventricle is located between the thalami, which are usually connected by the interthalamic adhesion creating a hole in the center of the third ventricle (see figure 1.5). CSF flows from the third ventricle through the narrow cerebral aqueduct of Sylvius into the fourth ventricle, which is located between the brainstem (pons and medulla oblongata) and the cerebellum. The fourth ventricle narrows down into the central canal of the spinal cord and is connected to the SAS via the median aperture (Foramen of Magendie) and the lateral apertures (Foramina of Luschka) [18].

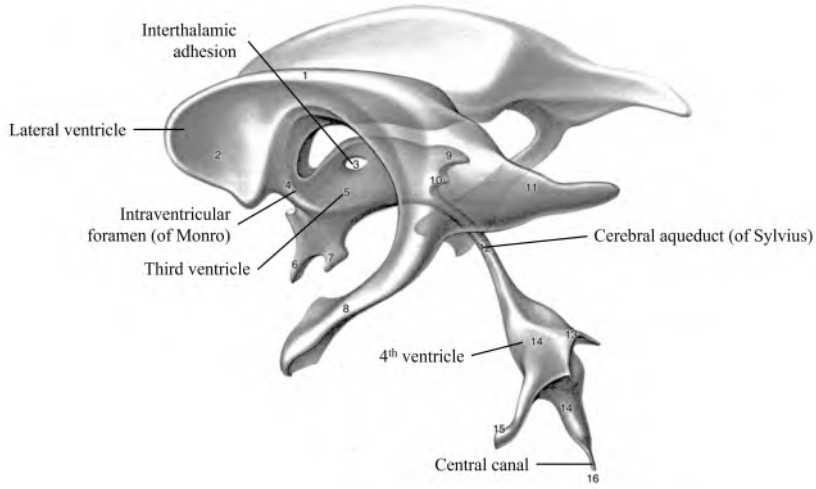


**Figure 1.5:** 3D figure of the ventricular system. This figure was adapted from Nieuwenhuys et al. [19].

The total CSF volume is typically stated to be around 150 ml [20] based on historical measurements using casts. However, recent studies have questioned whether this value is correct and indicated that a larger volume between 250 to 400 ml measured with magnetic resonance imaging (MRI) might be a better approximation of the total CSF volume. [21–23].

### 1.1.3 Cerebral vasculature

Besides the CSF and the brain parenchyma, cerebral arteries and veins occupy the intracranial compartment. The supply of oxygen-rich blood is essential for sustaining normal brain function and happens through the two internal carotid and two vertebral arteries. Figure 1.6 shows how the left and right common carotid arteries branch off from the aorta (left) and the brachiocephalic trunk (right) and split into the internal and external carotid arteries. The vertebral arteries separate from the subclavian arteries, which in turn transport blood coming from the aorta (left) and the brachiocephalic trunk (right). After entering the skull through the foramen magnum, the vertebral arteries merge into the basilar artery, which lies inside the CSF space anterior to the brainstem. The internal carotid arteries enter the intracranial compartment through the carotid canals on both sides (left and right) of the skull. The basilar artery and internal carotid arteries guide blood into the circle of Willis at the base of the brain from where arteries supplying different regions of the

brain branch off [24]. Although a full circle of Willis can help maintain blood supply in case one of the supplying arteries is blocked, a full circle of Willis is not present in all people [25]. The spinal cord is perfused by tiny vessels branching from three longitudinal spinal arteries: a single anterior and two posterior spinal arteries. These spinal arteries also receive blood from segmental arteries entering the vertebral column at each level (cervical, thorax, and lumbar) [24].

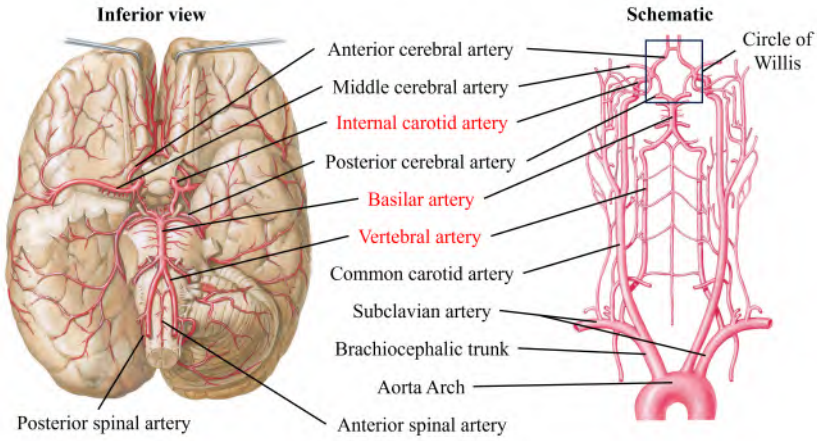


**Figure 1.6:** Cerebral arterial system. These figures were adapted from Netter et al. [12].

Figure 1.7 depicts the cerebral venous system. The cerebral veins do not have valves and have thin walls, making them collapsible. Within the intracranial cavity, venous blood is collected in large venous channels contained between the two layers of the dura, named dural sinuses. The large sinus following the longitudinal fissure between the cerebral hemispheres is the superior sagittal sinus. This sinus collects blood from regions close to the brain and interior skull surface, including the superior cerebral, diploic, and emissary veins. Diploic veins run within the skull whereas emissary veins cross through the skull. Blood coming from the deep cerebral structures and the choroid plexuses of the lateral and third ventricles is drained via the straight sinus which joins the superior sagittal sinus in the confluence of sinuses. This point connects with occipital and transverse sinuses. The latter continues as the sigmoid sinuses and transports blood to the main drainage pathway, the internal jugular veins. To a lesser extent, blood is also drained via the external jugular veins and the intravertebral venous plexus [19].

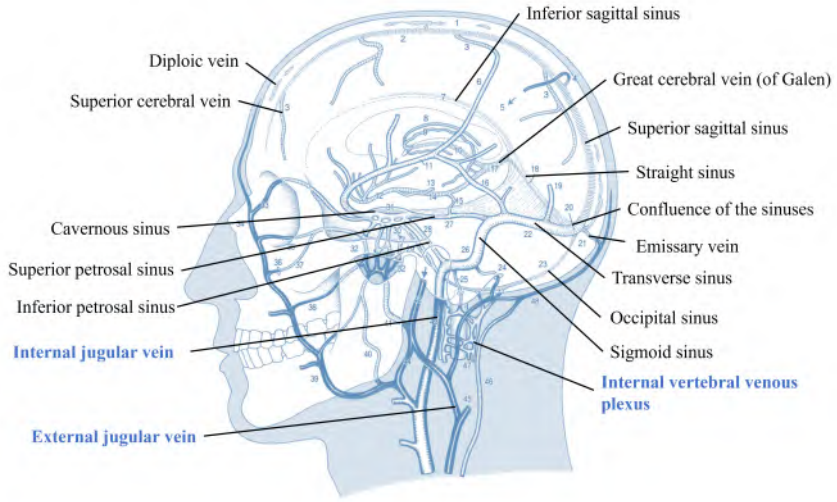


**Figure 1.7:** Cerebral venous system. This figure was adapted from Nieuwenhuys et al. [19].

Similar to the arterial blood supply, venous drainage from the spinal cord happens through a combination of longitudinal and segmental vessels, but the segmental vessels are fewer and there is only a single (longitudinal) posterior spinal vein. Importantly, within the epidural space, we find a dense network of interconnected veins, named the internal vertebral venous plexus (Batson's veins), also depicted in 1.8. The epidural plexus is in turn connected to the external vertebral venous plexus located outside of the vertebral column.

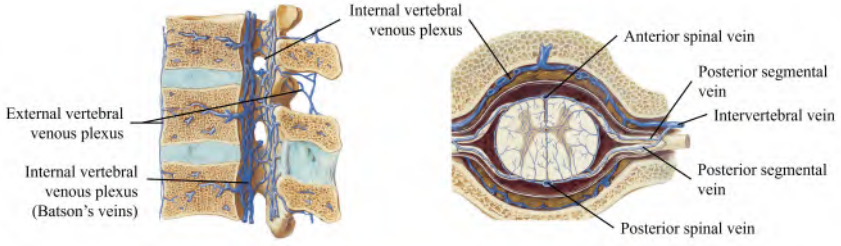


**Figure 1.8:** Spinal veins. These figures were adapted from Netter et al. [12].

## 1.2 Role of CSF in the central nervous system

The location of CSF in the central nervous system allows CSF to protect and sustain a stable central nervous system environment. First, CSF forms a protective layer cushioning against shocks, which is critical to avoid brain and/or spinal cord injuries during high-velocity impacts. Being submerged in CSF, the brain floats and, as a result, the brain's weight is distributed (effect of buoyancy). This is important to avoid local high stresses, which would otherwise appear in lower brain regions supported by the skull. Moreover, CSF helps maintain a chemically stable central nervous system environment through its role in the transportation and clearance of substances from the central nervous system [1, 26]. CSF has a water content of 99 %, which is higher than the 92 % water in blood plasma. The remaining CSF components are ions (e.g. $Na^+$, $Cl^-$,$K^+$), proteins, lipids, hormones, glucose, and many other molecules and metabolites [27]. The exchange of solutes and fluids between the CSF and the brain parenchyma is possible because of the presence of perivascular or Virschow-Robin spaces, which surround arteries and veins perforating the pia mater, allowing bi-directional motion of fluids between the CSF and interstitial fluid. The glymphatic system has been recently proposed as a mechanism for clearance of waste products, where the influx of CSF via perivascular spaces around arteries drives the convective flow of interstitial fluid across the brain into perivenous spaces, perivascular spaces surrounding large deep veins. Through these perivenous spaces, interstitial fluid and solutes can drain from the brain. This mechanism is depicted in figure 1.9. Impaired clearance of amyloid beta proteins at an older age might contribute to protein aggregation in Alzheimer's disease [28, 29].

Finally, the CSF helps maintain a stable intracranial pressure (ICP), which is essential to allow proper blood supply and avoid neural tissue damage. The rigid skull ensures that the combined volume of CSF, blood, and brain tissue remains relatively constant, as stated by Kellie [30]. Consequently, an expansion of one element, i.e. expansion of arteries during systole, needs to be compensated by displacement of another, which is typically CSF. The consequent displacement of CSF to a location with higher buffering capacity avoids pressure build-up in the skull, which might lead to brain tissue damage [1]. This motion of CSF also explains the pulsatile character of the CSF flow, which will be discussed in more detail in the next section.

In general, the dynamical behavior of CSF is the result of a complex interplay between different physiological mechanisms including the production and absorption of CSF, and interaction with the neurological tissues, the lymphatic and the cardiovascular system [1, 31]. Tight regulation of these dynamics is critical to preserve and protect central nervous system functioning.

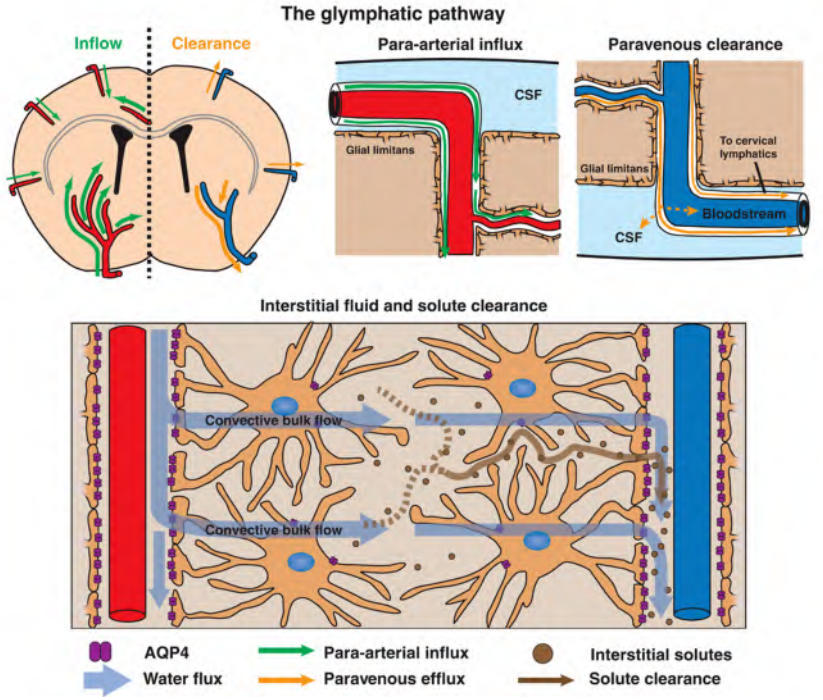


**Figure 1.9:** Glymphatic system with influx of CSF via the peri-arterial spaces into the brain parenchyma, and outflow via the peri-venous spaces. The exchange between the perivascular spaces and the brain parenchyma is facilitated by glial water channels. This figure was obtained from Iliff et al. [28].

### 1.2.1 CSF production and absorption

CSF is primarily produced by the choroid plexuses in the cerebral ventricles, which are estimated to account for 80-90 % of the production [1]. The choroid plexuses are composed of a single layer of epithelial cells connected by tight junctions and surrounding leaky capillaries. Passage of water from the blood into the cerebral ventricles happens through aquaporin-1 water channels and is driven by osmotic gradients, which are created by the exchange of ions across these epithelial cells. Hence, the choroid plexuses tightly control the

transfer of solutes and water from the blood to the CSF and their production should be relatively constant [29, 32]. The remaining production is expected to come from the exchange between CSF and the interstitial fluid. Within the brain, interstitial fluid is secreted via the blood-brain barrier between the cerebral arteries and the interstitial space. Where it is generally believed that the choroid plexuses are the primary contributors to CSF production, Klarica et al. suggested that CSF formation is driven by the flow of fluids through the walls of capillaries in the brain [33]. The total production is estimated to be around 0.4 ml/min [34, 35].

CSF absorption should happen at the same rate as CSF production to avoid CSF accumulation and the rise of CSF pressures. The arachnoid granulations were historically thought to be the primary CSF absorption pathway [1]. The arachnoid granulations or arachnoid villi are protrusions of the arachnoid mater into the dural sinus, allowing flow into the superior sagittal sinus and preventing backflow [20, 36]. Welch and Friedman performed experiments on the arachnoid villi of a green monkey and found that this one-directional flow only started around 50 mm $H_2O$ [37]. In humans, the minimal pressure difference necessary for absorption into the arachnoid villi might vary between 3 and 5 mmHg [36]. The assumption of arachnoid villi as the primary absorption pathway already stems from the 18th century and is mostly supported by anatomical evidence rather than physiological measurements. Interestingly, arachnoid villi only occur after birth implying that there should be alternative pathways for CSF drainage [1].

Injection of tracers in the CSF space of different animals, including rabbits, cats, and sheep, has indicated lymphatic drainage with routes along the olfactory nerves crossing the cribriform plate to eventually end up in the cervical lymph nodes. This theory was later confirmed in sheep by sealing their cribriform plate and removing their olfactory nerves, which led to elevated CSF pressures. Cserr found that between 14 and 47 % of the tracers injected in the CSF ended up in the lymphatic system [38]. There is, however, no consensus on the exact contribution of the lymphatic and arachnoid villi routes. While it was originally believed that the brain does not contain lymphatic vessels, recent discoveries of lymphatic vessels in the dura, also referred to as meningeal lymphatics, have supported alternative lymphatic pathways besides the cribriform plate [39, 40].

Next to absorption in the intracranial compartment, spinal drainage has been estimated to contribute to at least 25 % of the absorption

[36]. It is, however, unclear what percentage would be absorbed into the lymphatic system along the spinal nerves and what percentage into the veins via spinal arachnoid villi. Indeed, similar to the cranial compartment, arachnoid villi have been observed protruding through the dura at the spinal nerve ganglia (thickening of the spinal nerve) [36]. Figure 1.10 depicts the different sites of absorption draining in the venous and lymphatic system including the arachnoid villi, cribriform plate, and spinal nerves. After entering the neural parenchyma via the perivascular spaces, CSF might eventually become absorbed by small interstitial vessels, return to the CSF space, or leave the intracranial cavity by following the walls of the draining veins after being collected by the perivenous spaces [28, 29].

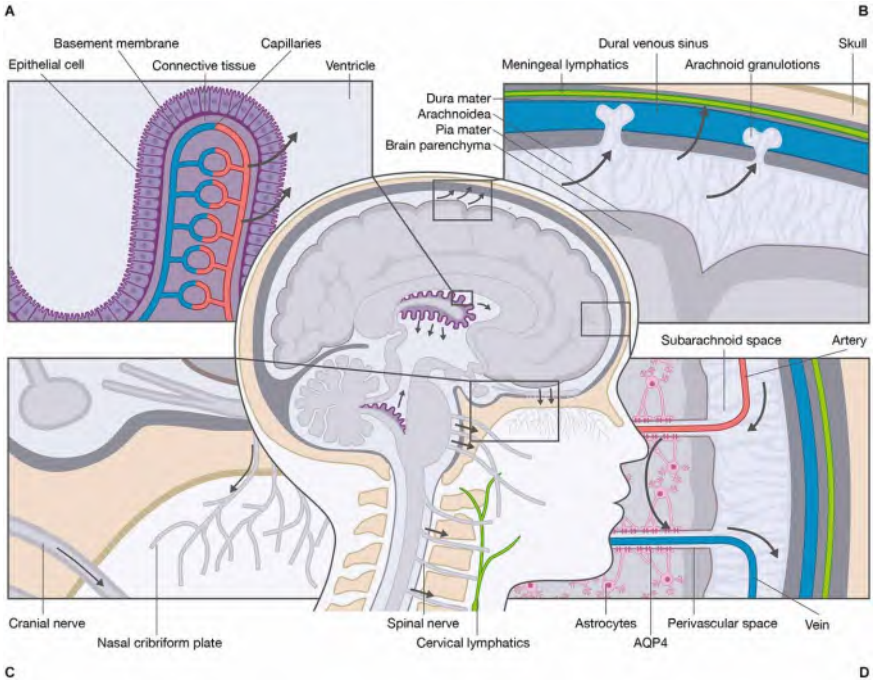


**Figure 1.10:** Schematic of CSF turnover with visualization of (A) CSF production by the choroid plexuses composed of epithelial cells surrounding capillaries and regulating secretion of CSF, absorption pathways via (B) arachnoid villi protruding in the superior sagittal sinus and (C) the cervical lymph nodes via the nasal cribriform plate, and (D) exchange between the CSF and the interstitium via the perivascular spaces. This figure was obtained from Wichmann et al. [41].

Where it was traditionally assumed that the CSF circulation is defined by a directed bulk flow from the choroid plexus to the arachnoid villi, newer findings have demonstrated more complex dynamics.

Indeed, rather than a constant flow, CSF dynamics are the result of the combination of directed bulk flow, pulsatile and irregular motion, and fluid exchange between the blood, CSF and interstitial fluid [35].

### 1.2.2 Pulsatile dynamics

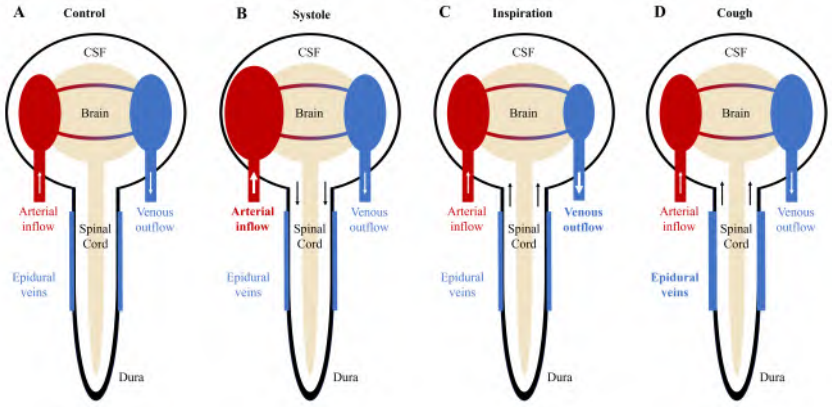


**Figure 1.11:** Schematic to explain how volume changes of arteries and veins cause CSF displacement during systole, inspiration, and coughing. (A) The baseline state depicting cerebral arteries, veins, and epidural venous plexus with original volumes. (B) Expansion of the total volume of the cerebral arteries during systole moves CSF in the caudal direction. (C) Inspiration requires a reduction of the intrathoracic pressure. This causes a reduction in intracranial venous volume and should lead to spinal CSF flow in the cranial direction (shown here). However, the combination of changes in intrathoracic pressure and consequent movement of venous blood might also induce volume changes of the epidural venous plexus, which also impacts the direction of the spinal CSF flow as indicated by Lloyd et al. [42]. (D) During coughing, CSF is forced in the cranial direction as a result of an expansion of the spinal epidural venous plexus.

The pulsatile motion of CSF is linked to changes in arterial and intrathoracic pressure, which are responsible for volume changes of cerebral arteries and veins, respectively [31]. These volume changes cause displacement of CSF, which explains pulsatile and bidirectional CSF motion as depicted in figure 1.11. CSF motion in the SAS is most pronounced in the central brain regions, and specifically in the CSF space at the ventral side of the brainstem, where the large supplying arteries enter the skull. In the mid-brain, where the cerebral ventricles are located, important tissue motion has been observed. It has been hypothesized that this motion is in part induced by the expansion and contraction of small capillaries inside the neurological tissues [31], but might as well originate from CSF pulsations in the SAS [43].

The volume of CSF that is moved into the spinal compartment per cardiac cycle depends on the total arterial volume change and the compliance of the spinal and intracranial compartments. CSF compliance is calculated as the volume change divided by the corresponding change in pressure. The cranial dura is non-distensible as it closely adheres to the skull. Consequently, intracranial compliance mainly comes from the capacity of veins and soft tissues to reduce in size. Meanwhile, the spinal dura can be distended in the radial direction perpendicular to the cord [44]. It has been estimated that, in a lying position, the spinal compartment contributes 63% - 73% to compliance in CSF buffering, but posture and changes in physiology can change these values [45, 46].

Respiratory effects have recently gained more interest. Yamada et al. [47] used a noninvasive MRI spin labeling technique to measure CSF motion in a person and observed significant movement of CSF during deep respiration with CSF flowing rostral (upward) during inspiration and caudal (downward) during expiration. These movements are considered to be a direct result of volume changes of the veins in the cranium. These volume changes are induced by changes in venous return with a decreased intrathoracic pressure during inspiration leading to increased return (see figure 1.11C) and an increased intrathoracic pressure during expiration causing a decreased venous return [47, 48]. However, Lloyd et al. found through a real-time MRI investigation that not only intracranial veins but also the communication of the internal and external vertebral venous plexus impact CSF motion during respiration. They indicated that volume changes of the epidural venous plexus might lead to local flow in the caudal direction in the spinal canal [42].

### 1.2.3 Effects of physical actions

Besides rhythmic effects induced by cardiac and normal respiration, more irregular are the effects on CSF flow of physical maneuvers, such as coughing [42, 49] or changing body position (e.g. going from a lying to an upright position) [50]. Coughing causes a rapid rise in intrathoracic pressure leading to volume expansion of the veins lying around the dura and spinal cord (i.e. epidural venous plexus). This venous volume expansion locally reduces the CSF space and in that way forces CSF through the foramen magnum to the intracranial compartment (see figure 1.11D), to return after. The impact of coughing has been observed as a peak in ICP [49] and a cranial peak flow through the foramen magnum [42].

Although we (humans) spend most of our day in an upright position, CSF dynamics are almost exclusively measured and described for subjects in supine (lying) positions. Nevertheless, changing from a supine to an upright position has been demonstrated to induce differences in both ICP [51] and flow [52, 53]. In supine position, ICP has an average value between 7 and 15 mmHg but undergoes a significant reduction (until negative values) when tilting to a sitting position [51]. Interestingly, a two-phase decrease of ICP was observed when performing a gradual transition from supine to sitting position with first a fast decrease in ICP followed by stabilization as depicted in figure 1.12.

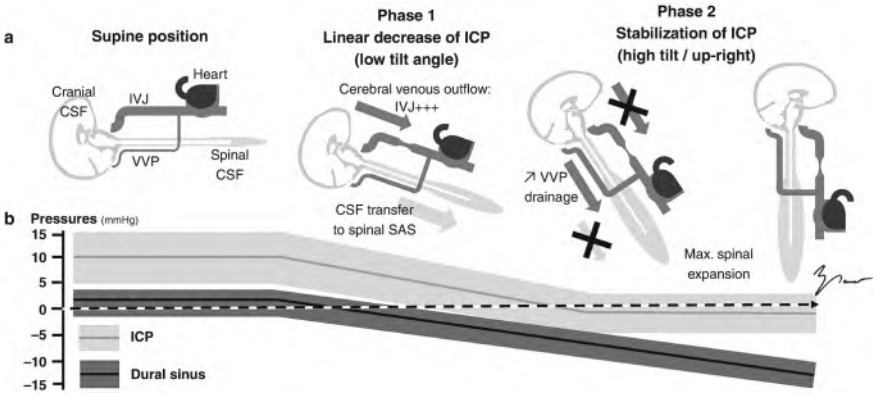


**Figure 1.12:** (A) Schematic of the postural regulation of ICP showing the CSF compartments and venous outflow pathways while increasing the tilt angle corresponding to supine to sitting position. (B) Graph of intracranial and dural sinus pressure for different tilt angles. This figure was obtained from Gergelé et al. [44].

The first factor that might influence this two-phase reduction is the redistribution of compliance. As previously mentioned, the spinal compartment contributes more to the total CSF compliance in a supine position because the spinal dura is distensible. Thus, when tilting to a sitting position, CSF is transferred to the spinal compartment, until the maximal spinal expansion is reached and thus the ICP stabilizes [44]. A second factor is the result of the interaction of the CSF with the intracranial venous sinuses, which are drained by the internal jugular veins. Holmlund et al. hypothesized that ICP in different body positions depends on the hydrostatic gradients in the venous system, but that these hydrostatic gradients are interrupted at higher tilting angles (closer to a sitting position) by the collapse of the internal jugular veins in the neck. The collapse of the internal jugular veins follows the mechanism of collapsible flexible tubes, in which a

flexible tube collapses when the pressure outside of the tube is higher than the pressure inside. This (partial) collapse avoids overdrainage of venous blood and more importantly hydrostatically decouples the cranial veins from the rest of the venous system. This prevents large hydrostatic heights (head and neck instead of head and venous reference point at thorax level) and thus stabilizes the pressures at higher tilt angles [51]. The latter theory, however, underestimates the role of the vertebral venous plexus in draining blood and venous pressure might not show this stabilization for larger tilt angles. Thus, postural regulation to date is not completely understood [44].

## 1.3 Chiari type 1 malformation

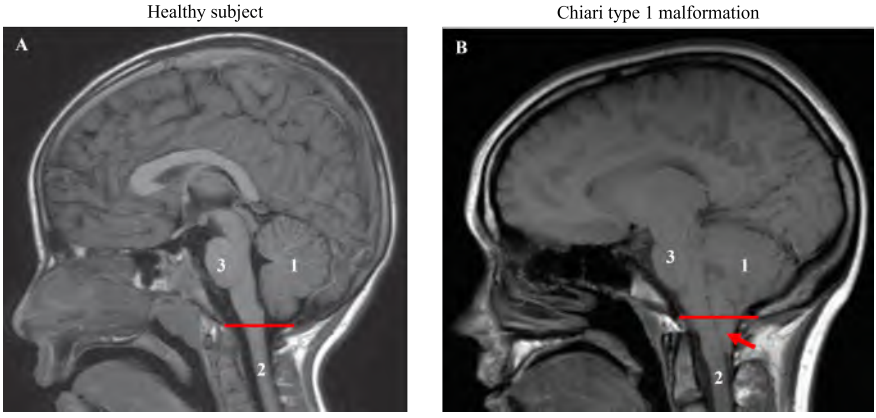


**Figure 1.13:** Sagittal MRI of the head with (1) cerebellum, (2) spinal cord, and (3) brainstem of (A) healthy subject (image adapted from Netter et al. [12]) and (B) patient with Chiari type 1 malformation (image adapted from Zisakis et al. [54]) depicting the herniated tonsils with red arrow.

As explained in previous sections, CSF normally circulates around the brain and spinal cord and moves freely between the spinal and intracranial compartments with the periodic expansion and contraction of the cerebral arteries and respiratory actions [30, 55, 56]. This CSF motion is, however, seriously hampered in Chiari type 1 malformation [57, 58]. In Chiari type 1 malformation, the cerebellar tonsils (lower part of the cerebellum) are herniated through the foramen magnum forming an obstruction. Chiari type 1 malformation has a prevalence between 0.56 to 0.75 % on MRI and is the type of hindbrain herniations, referred to as Chiari malformations, that is most commonly appearing in clinical practice [3]. The diagnosis is typically based on the depth of herniation of the tonsils, as observed

using MRI, whereby clinical guidelines suggest a threshold value of 5 mm or more below the level of the foramen magnum to diagnose Chiari type 1 malformation. However, this criterion has been questioned because of the poor correlation between depth of herniation and disease severity [3].

The exact cause leading to the tonsil herniation is unknown. However, the herniation has been associated with a reduced volume of the posterior cranial fossa, the part of the cranial cavity containing the cerebellum [3]. Other possible mechanisms include increased ICP (e.g. hydrocephalus), tumor formation within the posterior cranial fossa, and negative pressures in the spinal compartment due to lumbar shunts, which all could force the hindbrain downwards [59]. The abnormal location of the tonsils extending into the spinal canal causes three major problems:

- Local compression of the parenchyma of the brain and spinal cord, which can lead to local neural tissue damage [60]
- Disturbance of the normal movement of CSF between the spinal and intracranial compartments [57], which has been associated with headache (reported in 81% of the patients)[3]
- Formation of a secondary disorder named syringomyelia, where fluid accumulates within the spinal cord thereby creating a fluid-filled cavity [61]

Syringomyelia occurs in 12 to 80 % of the patients with Chiari type 1 malformation and has been associated with severe motor and sensory symptoms, and even paralysis [62–64]. During the last century, multiple studies investigated the link between Chiari type 1 malformation and syringomyelia and postulated theories on the origin of the latter. However, the exact mechanism behind this fluid accumulation is unclear [55]. Williams et al. hypothesized that large pressure differences between the intracranial and spinal compartments drive CSF into the spinal canal and as such lead to syrinx development. They suggested that these pressure differences appear during coughing and Valsalva maneuvers, and are amplified in patients with an obstruction due to a one-way valve mechanism depicted in figure 1.14. These ideas were supported by measurements in subjects with [65] and without obstruction [49], which serve as important references. This theory, however, assumes the exchange of CSF between the syrinx and the central canal, creating a so-called communicating

syrinx, which has not been seen in all patients with Chiari type 1 malformation [66].

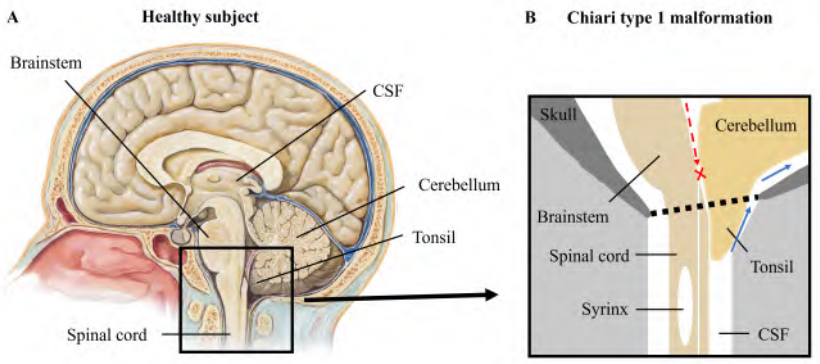


**Figure 1.14:** (A) Geometry of the hindbrain as in a healthy subject (figure adapted from Netter et al. [12]) and (B) Schematic of tonsillar herniation in Chiari type 1 malformation. This occlusion acts as a one-way valve by allowing cranial flow and blocking caudal flow.

Ball and Dayan also suggested that syrinx fluid comes from CSF but enters the spinal cord via perivascular spaces. They proposed that when flow through the foramen magnum is blocked CSF is forced into the cord during dilation of the epidural veins, e.g. during respiratory actions such as coughing [67]. Oldfield and Heiss also proposed a perivascular pathway but suggested the cerebellar tonsils act as a piston causing pressure waves in the caudal direction that drive CSF into the spinal cord [68, 69]. Interestingly, Heiss presented the results of a clinical study including MRI, ultrasound, and invasive pressure measurements in healthy subjects and patients with Chiari type 1 malformation and found a reduction of the compliance of the spinal SAS [70].

More recently, scientists have proposed theories with syrinx fluid originating from extracellular fluid rather than CSF [71]. For instance, Carpenter et al. proposed the elastic jump theory, which assumes that the pressure wave created by a Valsalva maneuver is reflected by the obstruction formed by the herniated tonsils, thereby creating a local high-pressure zone. This high-pressure zone would be the site of accumulation of extracellular fluid and eventually syrinx formation [6]. Elliot et al. later indicated that elastic jumps or any shock-like mechanisms caused by the reflection of waves against stenosis are too weak and even reduced by viscous damping in the

spinal canal, to be at the origin of syrinx formation [72]. Greitz proposed that the reduced diameter at the level of the herniation caused suction of the spinal cord as a result of the venturi effect, but this effect is likely negligible [73].

In current clinical practice, severe symptomatic Chiari type 1 malformation is usually treated by a surgical procedure called posterior fossa decompression. This procedure is depicted in figure 1.15 and aims to remove the obstruction, caused by the herniated tonsils, by the enlargement of the posterior cranial fossa to restore the normal CSF flow [74]. However, the surgical treatment is controversial because (i) the procedure increases the risk of complications including infections, CSF leakage, and damage to the blood vessels, and (ii) the long-term outcomes are variable and unpredictable: some patients (reported to be more than 15%) show no improvement or even deterioration of the health state [75]. Therefore, the interest is raised to explore alternative and less invasive treatments for the patients [76], but new therapies require a better understanding of the mechanisms leading to syringomyelia.

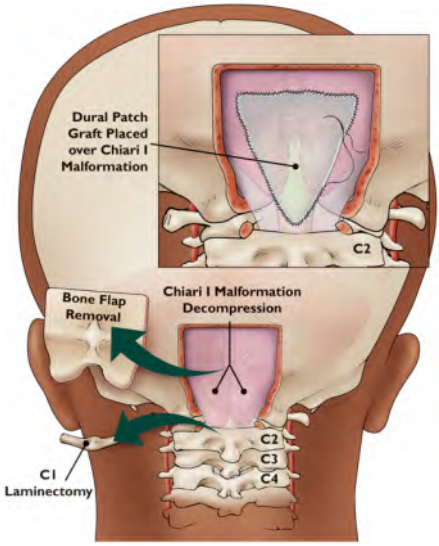


**Figure 1.15:** Schematic of the decompression surgery. This figure was obtained from Butensky et al. [74].

## 1.4 Measurement techniques for research and diagnosis

The CSF is not easily accessible for in vivo measurements and the assessment of physiological processes and their impact on the CSF

pressures and velocities is challenging. Pressure measurements with a ventricular catheter allow real-time CSF pressure monitoring but require invasive implementation of measurement devices and provide no spatial pressure data [7]. In contrast, MRI techniques provide a non-invasive tool to study CSF flow in vivo. Particularly interesting for capturing flow are Phase-Contrast (PC) MRI and 4D flow techniques that can be used to measure flow velocities in one plane as well as in the full domain. However, these are typically cardiac gated, meaning that velocities are the result of measurements over multiple cardiac cycles, and effects such as breathing are removed [77]. More recently, real-time MRI techniques have been developed allowing tracking cardiac induced flow as well as other effects including coughing and respiration [42, 56]. Capturing the slow CSF flow is not trivial and there are important differences between scanner centers [78], artifacts, and limited MRI resolution [8, 79].

The brain tissue also pulsates following the cardiac cycle, with the strongest pulsations in the central brain regions. Doppler ultrasound and MRI techniques have been used to measure this motion. Doppler ultrasound has the advantage of high temporal resolution but is typically limited to a single beam line or 2D plane and lacks anatomical information. MRI allows the researcher to directly locate the motion in the brain anatomy while higher costs, longer scan times, and lower temporal resolution are important limitations. Almudayni et al. found five different MRI techniques that have been used to measure brain tissue motion, with PC-MRI and Displacement Encoding with Stimulated Echoes (DENSE) being the most frequently reported techniques [80]. PC-MRI allows measurement of the velocities of tissue motion, while DENSE measures displacements and strains. For instance, Pahlavian et al. used PC-MRI to define the motion of the cerebellar tonsils in Chiari type 1 malformation and found a displacement between 150 and 300 $\mu$m [81]. Amplified MRI (aMRI) is a qualitative method to visualize displacement and has as major advantages short scan time and the ability to reveal subvoxel motion by magnifying the motion captured with cine MRI. The major limitation is that the method currently lacks the ability to quantify motion [80].

MRI can provide us with a range of anatomical and functional data about the anatomy and dynamics of CSF. However, the use of MRI data to investigate CSF dynamics is currently limited by (i) general limitations regarding temporal resolution, image quality, and operator dependence of results, (ii) the high cost and necessity of

infrastructure which limits the number and duration of scans that can be taken, (iii) information that is typically obtained at specific locations (i.e. coronal slices) to avoid these long scan times, (iv) CSF and brain tissue motion that is mostly cardiac-gated removing information of other physiological actions, (v) CSF production and absorption are generally too slow to be detected from MRI. Computational models can use the data that is already available through MRI and have the ability to fill the gaps that MRI leaves by offering high temporal and spatial resolution, allowing the inclusion of slow biological mechanisms such as production and absorption and accounting for non-MRI conditions including different body positions, and respiratory actions. These models are however only reliable when they capture the real CSF dynamics accurately and if they are appropriately validated. MRI measurements have become more and more essential to serve as input and validation of computational models, which will be discussed in chapter 2.

Chapter 2

# State-of-the-art in computational modeling of CSF dynamics

Computational models can advance our understanding of the complex CSF dynamics and the mechanisms driving them. With growing computational resources, models of a wide variety have been developed with different degrees of complexity and focussing on different regions of interest. CSF computational models can be categorized into three main groups: lumped parameter models, 1D and 2D axisymmetric models, and subject-specific 3D models.

## 2.1 Lumped parameter models

0D models, also referred to as lumped parameter models, simplify fluid flow in a biological system as a network of components. Each component is the hydraulic equivalent of an electric circuit component, allowing to resolve the system by solving a set of differential equations [82]. These models have low computational requirements and additional components can easily be added with new biological insights, making them a useful tool in studying CSF dynamics. 0D models have been successfully developed to model ICP dynamics and compliance [83]. In 1975, Marmarou modeled CSF pressure dynamics assuming a single CSF compartment, constant CSF formation,

venous absorption, and CSF compliance by using an electrical circuit analogy depicted in figure 2.1 [84].

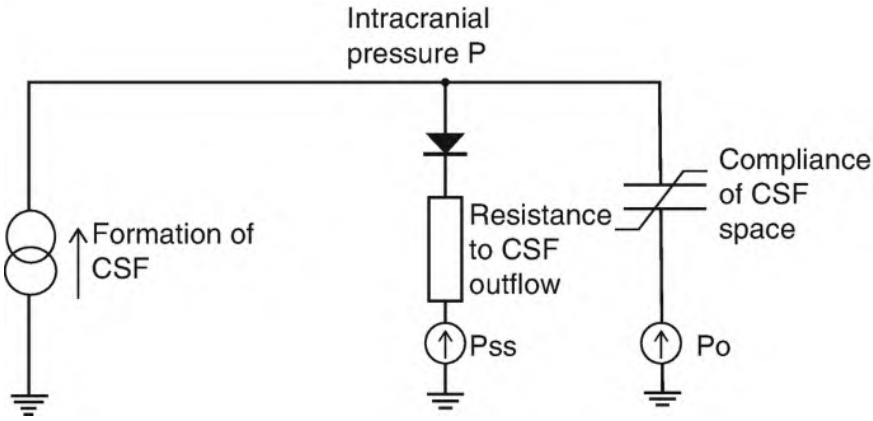


**Figure 2.1:** Schematic of the electrical circuit representing the CSF circulation, with ICP being influenced by the CSF formation rate, outflow into the venous system governed by the CSF outflow resistance and the sagittal sinus pressure ($P_{ss}$) and CSF buffering governed by CSF compliance and the reference pressure ($P_o$). This figure was obtained from Geregé et al. [85] and visualizes the model presented by Marmarou et al. [84].

In the next decades, models became gradually more complex by coupling CSF with cerebral arterial and venous blood flow [86–88], and eventually also including the role of the neurological tissues and the lymphatic system [89]. Interestingly, Tain et al. [46] implemented windkessel models in a 0D model to estimate heterogenous CSF compliance based on PC-MRI. Figure 2.2 shows the equivalent electrical circuit corresponding to this model.

Recently, Toro et al. [90] coupled a lumped parameter model of the CSF system (see figure 2.3) with a complex model of the cardiovascular system combining 1D representations of major blood vessels with 0D components. The lumped parameter model of the CSF system used was previously developed by Linninger et al. [91] and represented the different CSF compartments and the biphasic brain parenchyma as idealized cylinders, which were coupled to both the venous and arterial system. In general, lumped parameter models have contributed to a better understanding of ICP and the interaction of the CSF with the cardiovascular system, but they lack spatial information by not accounting for and not resolving the complex anatomy of the CSF spaces.

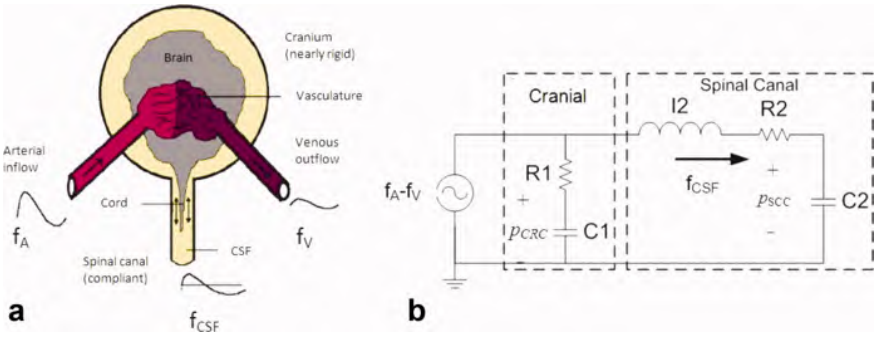


**Figure 2.2:** (A) Schematic of the intracranial and spinal compartment and (B) equivalent electrical circuit to present the flow dynamics in the CSF compartments with arterial inflow ($f_A$), the venous outflow ($f_V$), craniospinal CSF flow ($f_{CSF}$), pressure in the cranial compartment ($p_{CRC}$), pressure in the spinal canal ($p_{SCC}$), flow resistance of the cranial ($R1$) and spinal ($R2$) compartments, compliance of the cranial ($C1$) and the spinal ($C2$) compartments, and the inertia component of CSF flow ($I2$) to and from the spinal canal. This figure was obtained from Tain et al. [46].

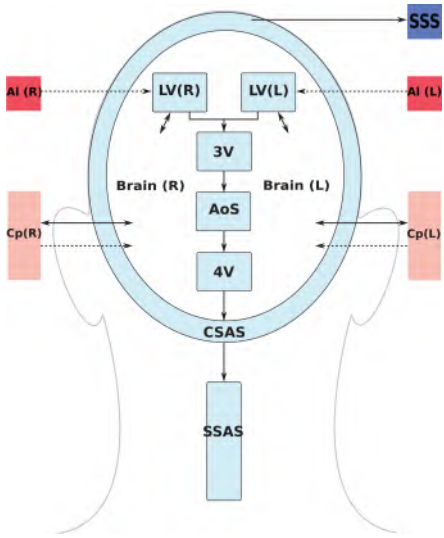


**Figure 2.3:** Schematic representing the lumped parameter model of the CSF spaces, which are interconnected and coupled to the venous and arterial system via the cerebral arterioles (Al), capillaries (Cp) and superior sagittal venous sinus (SSS). This figure was obtained from Toro et al. [90].

## 2.2 Simplified models of the spine

The spinal canal can be simplified as a system of two concentric tubes and therefore can be studied using 1D and 2D axisymmetric models. Their main advantage over 0D models is that they are spatially resolved allowing studying wave propagation, directional flow, and pressure gradients while still avoiding high computational costs. Carpenter et al. used a 1D model to develop the elastic jump theory, with the single spatial dimension allowing studying the propagation of waves through the spinal canal due to coughing [6]. As a response, Bertram et al. evaluated the impact of transients imitating arterial pulsations and coughing in a 2D axisymmetric finite element model of the spine with a blockage [92]. They concluded that the formation of a shock wave that can eventually lead to syrinx formation is unlikely, which was later confirmed by Elliott et al in a 1D model [72]. In the years after, Bertram et al. further used 2D axisymmetric models for studying the effects of a SAS stenosis on spinal cord stresses, pressure distribution, and fluid exchange with an adjacent syrinx to better understand the origin of syrinx formation and progression [71, 93, 94]. Their latest fluid-structure interaction model is depicted in figure 2.4. Interestingly, significant spatial pressure differences were only found for slow waves (timescale 0.1 - 1 s) and not for rapid excitations imitating coughing (timescale 1 ms). This was because short excitatory pressure pulses mainly produced pressure wave propagation and did not lead to significant fluid displacements. Meanwhile, slow excitations, transient and periodic, led to fluid acceleration in the spinal SAS and consequent pressure gradients. Moreover, periodic cyclic movement led to a one-way valve mechanism with elevated SAS pressure caudal to the stenosis [94].

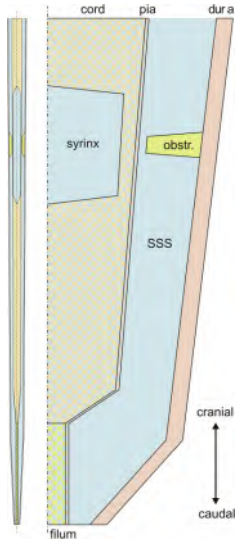


**Figure 2.4:** Axisymmetric model geometry used by Bertram et al. [71] to study the impact of an obstruction on a porelastic spinal cord with syrinx. Here, SSS depicts the spinal SAS. This figure was obtained from Bertram et al. [71].

## 2.3 Subject-specific 3D models

A third category consists of CSF models that enable resolving CSF pressures and velocities in all three spatial dimensions. Where two concentric tubes can serve as a reasonable approximation of the the spinal canal, the complex geometry of the intracranial CSF space is in an ideal scenario directly extracted from medical images allowing for subject-specific calculations of CSF dynamics. Within the 3D CSF space, CSF dynamics can be described through computational fluid dynamics (CFD) in case we consider rigid walls. To account for the interaction of the CSF with the surrounding soft tissues, a fluid-structure interaction coupling can be set up. CFD is most widely used to perform detailed simulations of CSF dynamics and is also the numerical technique used in this work.

### 2.3.1 Basics of CFD

In CFD, a numerical approach is used to solve the partial differential equations describing fluid motion. In general, the dynamics of a fluid (without heat transfer) are bound by the conservation of mass and momentum. For mass to be conserved in a specific volume, the rate of fluid accumulation should be equal to the net mass flow going into this volume. Conservation of mass can be described as the partial

differential equation 2.1 with as general form the equation 2.2, which is also known as the continuity equation.

$$\frac{\partial \rho}{\partial t} + \frac{\partial(\rho u)}{\partial x} + \frac{\partial(\rho v)}{\partial y} + \frac{\partial(\rho w)}{\partial z} = 0 \tag{2.1}$$

$$\frac{\partial \rho}{\partial t} + \nabla \cdot (\rho \overrightarrow{v}) = 0 \tag{2.2}$$

Here, $\rho$ is the fluid density, and u, v, and w are the x, y, and z components of the velocity $\overrightarrow{v}$. For incompressible fluids, the density ($\rho$) is constant, and as such equation 2.2 is simplified as depicted in equation 2.3.

$$\nabla \cdot \overrightarrow{v} = 0 \tag{2.3}$$

The forces acting on a mass should be equal to the acceleration multiplied by the mass, as stated by Newton's 2nd law (equation 2.4).

$$m \overrightarrow{a} = \sum \overrightarrow{F} \tag{2.4}$$

Here, m is the mass of the fluid element, $\overrightarrow{a}$ the acceleration, and $\overrightarrow{F}$ the forces acting on the fluid element. This equation can be rewritten as a set of partial differential equations in a fluid volume following the three main velocity directions, which are also known as the Navier-Stokes equations (see equation 2.5 assuming an incompressible fluid).

$$\rho \frac{\partial(\overrightarrow{v})}{\partial t} + \rho \overrightarrow{v} \cdot (\nabla \overrightarrow{v}) = -\nabla p + \nabla \cdot \tau + \rho \overrightarrow{g} + \overrightarrow{f} \tag{2.5}$$

The left-hand side describes the rate of change in velocity ($\overrightarrow{v}$) over time that is experienced by a volume that moves in space. The first term accounts for the variations in velocity over time at the point where the volume is situated whereas the second term describes the change in velocity as a result of the fluid moving in the domain with spatially variable condition states. Meanwhile, the right-hand side is composed of the terms describing the body and surface forces acting on the fluid volume. Body forces ($\overrightarrow{f}$) are described per unit mass and act directly on the volumetric mass of the fluid volume (e.g. gravity and centrifugal forces). Meanwhile, surface forces act on the surfaces of the fluid volume and are the result of internal shear and normal viscous stresses ($\tau$) and outside pressure ($p$) from surrounding fluid.

CSF can be considered as an incompressible fluid. For Newtonian fluids, the viscous stress tensor $\tau$, which includes normal and shear components, can be written in function of viscosity $\mu$. This results in equation 2.6, which is the form generally used to describe CSF dynamics.

$$\rho \frac{\partial \overrightarrow{v}}{\partial t} + \rho \overrightarrow{v} \cdot (\nabla \overrightarrow{v}) = -\nabla p + \mu \nabla^2 \overrightarrow{v} + \rho \overrightarrow{g} \tag{2.6}$$

### 2.3.2 Numerical techniques for solving partial differential equations

The system of non-linear partial differential equations presented in the previous section has no general closed-form solution, but we can approximate the exact solution by discretizing these equations in space and, in the case of transient simulations, also in time. The discretization of the governing equations provides us with a so-called numerical solution, which gives the values of the variables of interest (e.g. velocity and pressure) in a discrete number of points in the spatial (and time) domain. For discretization in time, a frequently used technique is the implicit time integration where a scalar value in a given cell in the next timestep (n+1) is described in function of its value at the current timestep (n) and of the values in the neighboring cells at the next timestep (n+1). Commonly used methods for discretization in space are the finite differences, finite elements, finite volumes, and the lattice Boltzmann methods. In each method, spatial discretization is realized by dividing the volume of interest into small subvolumes, which correspond to the discrete points where the solution is determined and form the computational grid.

In the method of finite differences, the partial derivatives are replaced by discrete expressions with variables corresponding with specific, discrete grid points into which the domain is divided [95]. An important disadvantage of the finite differencing method for spatial discretization is that the grid needs to be structured. A structured grid is difficult to generate in the complex CSF spaces [9], and that is one of the reasons why finite volume and finite element methods, which function well with unstructured grids, have been used in CFD modeling of the CSF.

The CFD software Fluent (Ansys, Canonsburg, USA) used in this dissertation uses finite volume discretization. In the finite volume method, each cell (subvolume) is considered as a control volume, in which the conservation laws are applied to determine the flow variables. Therefore, the partial differential equations (conservation of mass and momentum) are integrated, and consequently, the integrated convection and diffusion terms can be written as the sum of the fluxes through the faces, which are the control boundaries of the control volume. These fluxes are written as discretized expressions based on the values in neighboring cells using discretization schemes (e.g. upwind and central schemes) [96]. An alternative approach, which has become more widespread in CSF modeling, is the lattice Boltzmann method [9]. In contrast to traditional methods, where

fluid dynamics are modeled as a continuum, a discrete approach is adopted, where for each time point and position of a predefined grid (lattice) the probability of encountering a particle with a specific velocity is determined. This probability is described by a distribution function, which can be determined by solving kinetic equations [97].

### 2.3.3 State-of-the-art in CFD modeling of CSF dynamics

The application of CFD for simulating CSF is a relatively recent evolution that was aided by the availability of MRI sequences allowing non-invasive measurements and extraction of the complex anatomy of the CSF spaces [9]. The first CFD models were developed by Jacobson et al. [98, 99] in 1996 to evaluate pressure differences over a cerebral aqueduct. Where Jacobson et al. used idealized geometries, Fin and Grebe directly extracted the aqueduct geometry from magnetic resonance (MR) images [100]. Soon after, researchers started including the remaining parts of the ventricular system, first with an idealized geometry [101], and later directly based on MR images, where Kurtcuoglu et al. demonstrated the use of CFD in reconstructing the flow field in the third ventricle by using MRI scans [102]. In this model, a constant pressure was imposed at the foramen of Monro, and pulsations were induced based on MRI measurements including an up-and-down motion of the third ventricle's walls and a velocity inlet at the inferior end of the cerebral aqueduct. Following these initial studies, multiple CFD models of the CSF have been developed. Most studies focused on part of the CSF geometry (i.e. the ventricular system [103–113], or SAS [22, 79, 81, 114–121]), which allowed studying local effects but did not provide insight into the system-wide responses. Figure 2.5 shows the model geometry of the complete ventricular system used by Yoshida et al. [111].

Increasing computational resources and advances in medical imaging have now enabled researchers to include the complete CSF space. In 2015, Tangen developed a CFD model of the complete CSF space with the inclusion of arachnoid trabeculae to study the spread of drugs within the CSF. In this model, arterial pulsations were induced by periodically deforming the choroid plexus in the lateral ventricles, the cranial pia, and the thoracic and lumbar spine [122]. More recently, Khani et al. [120] developed a CFD model of the full CSF circulation thereby including constant CSF production in the lateral ventricles, CSF pulsations at the caudal end of the spinal compartment as measured at the cervical (vertebra C2-C3) level, and a zero-pressure outlet at the cranial opening. This model was intended to compare blood removal from the CSF between two filtration systems,

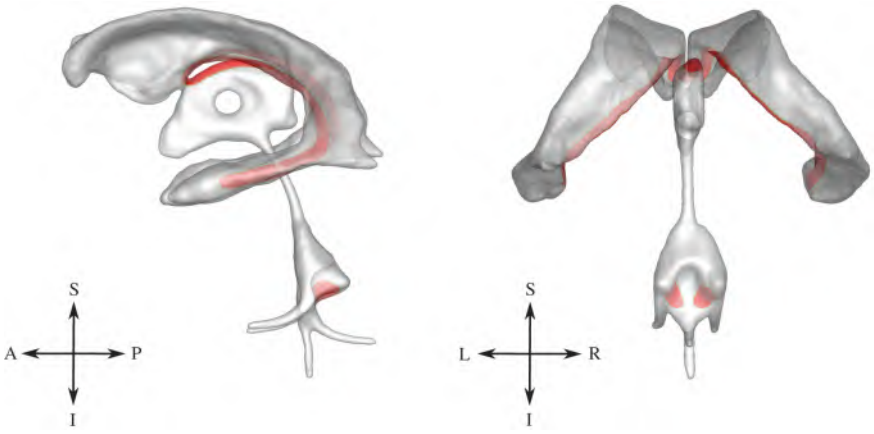


**Figure 2.5:** Model geometry used by Yosida et al. of the ventricular system with choroid plexus depicted in red. This figure was obtained from Yosida et al. [111].

i.e. lumbar drain and a dual-lumen catheter-based CSF filtration system. They used a biphasic model where blood was introduced as a tracer with the same viscosity and density as CSF. Importantly, they validated the computational model with in vitro experiments in an in vitro model with an identical geometry. In a follow-up study, this model was expanded by adding a respiration pulsation term at the caudal end [123]. Fillingham et al. presented a model of the intracranial CSF with inflow and outflow boundary conditions imposed at the choroid plexus, ventricular walls, surface of the cerebrum, foramen magnum, and arachnoid granulations calculated directly from PC-MRI measurements of the CSF and cardiac in- and outflow with obtained velocities presented in figure 2.6. They aimed to present a methodology that allows the simulation of CSF flow purely based on MRI flow measurements without unnecessary assumptions [124].

The previous paragraphs highlight the important variation in the use of boundary conditions between studies. This is in part the result of the lack of consensus on the origin of CSF pulsations (e.g. choroid plexus, third ventricle, physical arteries, brain tissue), and the complexity and incomplete understanding of the processes impacting CSF dynamics. Although there is evidence for fluid exchange with the interstitium and lymphatic absorption [35, 39], in models of the complete CSF space only venous absorption has been considered [120, 123, 125–127]. 3D CFD models can resolve fluid dynamics in complex CSF spaces, in that way providing information that can help us to understand the effects of local geometric features (e.g. interthalamic adhesion in Chen et al. [105]) and pathological changes (eg.

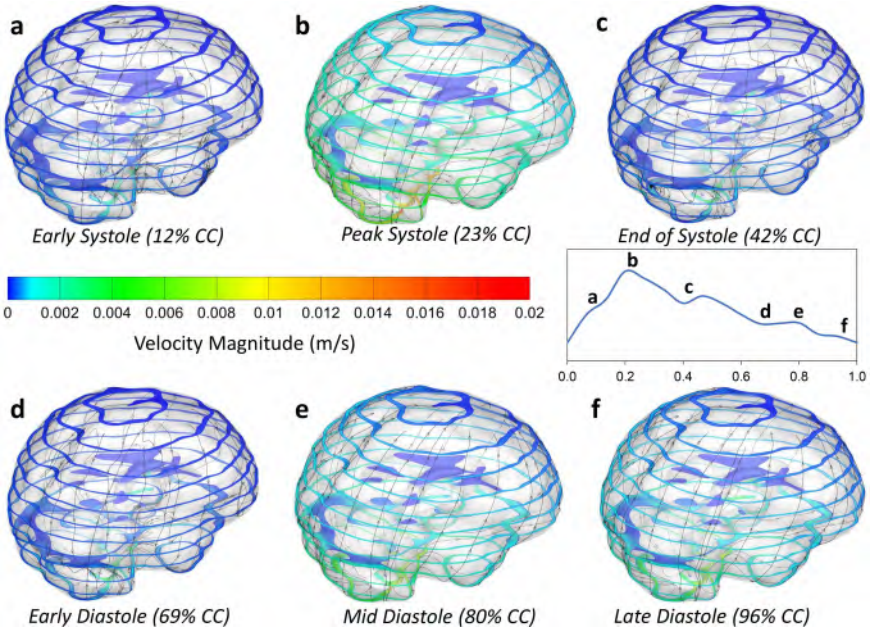


**Figure 2.6:** Simulation of velocities in the intracranial compartments as presented by Fillingham et al. in their model of the cranial CSF space. This figure was obtained from Fillingham et al. [124].

stenosis of the cerebral aqueduct and Chiari type 1 malformation) on velocities and pressure differences. However, in contrast to the previously discussed lumped parameter models (see section 2.1), CFD models of the CSF can only resolve spatial pressure differences and do not provide information on absolute pressures as recorded during ICP monitoring. Modeling absolute pressures would require the incorporation of resistance and compliance in the models. Spinal compliance has been previously implemented in fluid-structure interaction models by including a deformable dura by Sweetman et al. [128] and more recently as a pressure-volume relation by Causemann et al. [129]. To the best of our knowledge, no 3D computational studies have incorporated a heterogeneous compliance distributed over the cranial and spinal compartments.

### 2.3.4 Modeling Chiari type 1 malformation

Besides modeling general CSF dynamics, CFD models have been frequently used to study the impact of an obstruction as present in Chiari type 1 malformation. Roldan et al. compared velocities and pressures in a CFD model of the cervical-cranial junction in a healthy control and a patient with Chiari type 1 malformation at two time

points, systole, and diastole [130]. They found a 50 % steeper pressure gradient across the obstruction and higher magnitude flow jets in the patient with Chiari type 1 malformation compared to the healthy volunteer. To allow investigation of transient effects later studies used in vivo PC-MRI measurements to feed into CFD models of the CSF to assess pressure (differences). They found increased peak velocities and pressure gradients in Chiari type 1 malformation compared to healthy controls [131–135]. Stoverud et al. found elevated velocities in patients with Chiari type 1 malformation as clearly demonstrated with the velocity streamlines depicted in figure 2.7.

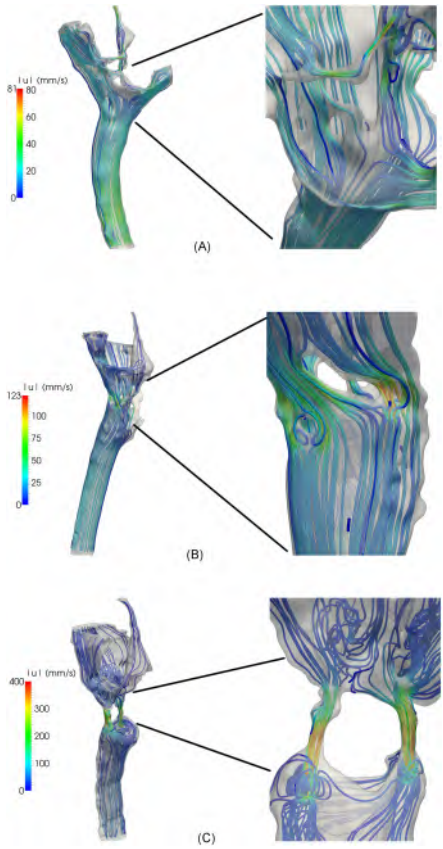


**Figure 2.7:** Figure obtained from Stoverud et al. [134] with velocity contours of a healthy control, and two patients with Chiari type 1 malformation.

Studies expanded these models to account for more physiological mechanisms, i.e., perivascular flow [42] and the periodic movement of the cerebellar tonsils [81]. Longitudinal impedance, calculated as the ratio of pressure difference and flow and derivable from CFD simulations, was introduced as a hydrodynamic parameter for assessing

disease severity by Loth and collaborators [136–139] and was found to be significantly elevated in patients with Chiari type 1 malformation compared to healthy controls.

Where the aforementioned studies provided valuable information on the effects of an obstruction on local CSF flow, the hemodynamic impact of physiological actions such as coughing and system-wide effects in patients with Chiari type 1 malformation have, to the best of our knowledge, not been explored. These studies considered only a small part of the CSF space and only accounted for arterial effects measured on an MRI scanner using cardiac-gated sequences. To the best of our knowledge, the impact of coughing in the presence of an obstruction (stenosis) has only been investigated in 1D and axisymmetric models of the spinal SAS. As discussed in section 2.2, Elliot et al. [72] and Bertram et al. [92] focused on the evaluation of shock-like mechanism previously proposed by Berkouk and Carpenter [6, 140]. Contrasting results were found when studying pressure differences with a limited impact of coughing indicated by the finite element framework by Bertram et al. [94] and an important amplification in pressure in the experimental model by Martin and Loth [141]. The four different in vitro setups of the spinal canal used by Martin and Loth are depicted in figure 2.8.

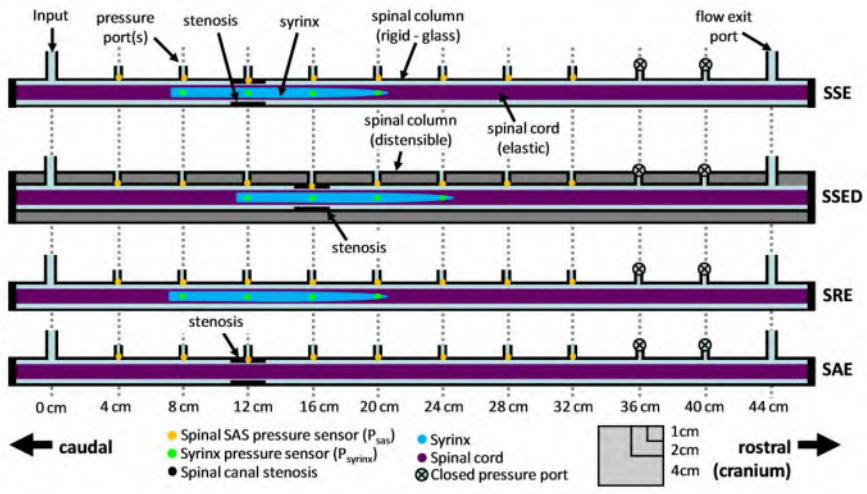


**Figure 2.8:** Schematic of four in vitro models of the spinal canal with cough pressure pulse imposed at caudal end: model with syrinx and stenosis (SSE), model with distensible spinal column (SSED), model with syrinx (SRE), and model with stenosis (SAE) used in the study by Martin and Loth. This figure was obtained from Martin and Loth [141].

## 2.4 Conclusion

In conclusion, computational models with different degrees of complexity have been developed to study CSF dynamics in healthy subjects and patients with Chiari type 1 malformation. 0D models have been successfully applied for modeling ICP and compliance but cannot capture spatial differences in pressure and flow. Meanwhile, CFD studies allowed detailed evaluation of fluid pressures and velocities within the complex CSF spaces but only provided information about spatial pressure differences and did not consider CSF compliance. Even more, we found no 3D computational studies that considered the heterogeneous compliance distribution over the intracranial and spinal compartments. Furthermore, studies focusing on Chiari type 1 malformation limited their analysis to the regions close to the foramen magnum, thereby ignoring possible system-wide effects.

Symptoms of Chiari type 1 malformation have been linked to local and system-wide changes in CSF dynamics. Therefore, computational models that can be used to not only study local but also system-wide CSF dynamics can serve as valuable tools in studying this disorder. For these models to capture absolute pressures (i.e. ICP), and spatial pressure and flow distribution, we will need to combine the approaches used in 0D and CFD models. In the next parts, the development and application of these models are presented.

# II

# Computational fluid dynamics models of the cerebrospinal fluid

Chapters

CHAPTER 3

# Implementing physiological boundary conditions

The dynamical behavior of CSF is the result of a complex interplay between CSF production, absorption, and interaction of the CSF with the cardiovascular system and the surrounding soft tissues. A computational model that incorporates these mechanisms as boundary conditions is an ideal tool for assessing CSF dynamics under different conditions. As discussed in section 2.3.3, physiological mechanisms have been incorporated to some extent in previous computational studies, but 3D models that consider realistic distributions of CSF compliance and absorption were lacking. In this chapter, we present the setup and application of a CFD model that allows the simulation of both absolute and relative pressures within the complex cranial and upper spinal CSF spaces. We here address the limitations of previous studies through implementation of distributed CSF absorption and compliance in a 3D model of the CSF.

This chapter is based on the paper with title *"Computational fluid dynamics model to predict the dynamical behavior of the cerebrospinal fluid through the implementation of physiological boundary conditions"* published in Frontiers in Bioengineering and Biotechnology [142].

## 3.1 Methods

A CFD model of the CSF circulation was constructed from medical images and literature data following four steps: (i) Segmentation of the 3D geometry, (ii) generation of computational mesh, (iii) implementation of boundary conditions, and (iv) set up of the numerical solver. These are elucidated in detail in the next paragraphs. The CFD analysis was performed using the numerical software Fluent 2021 R2 (Ansys, Canonsburg, USA).

### 3.1.1 Model geometry

First, the three-dimensional geometry was segmented from clinical T2 MRI images of a patient with Chiari type 1 malformation (Figure 3.1) using Mimics 21.0 (Materialise, Leuven). These image data were collected at Ghent university hospital using a 3 Tesla Prisma system (Siemens, München, Germany) and exist of sagittal 2D slices (in-plane resolution of 0.625 mm x 0.625 mm) of 3 mm. The use of the anonymized data for this study was approved by the ethical committee of Ghent University Hospital. The geometry of the cranial CSF space is complex, especially because of the seepage of CSF between the folds of the brain surface. These irregularities can significantly increase the necessary computational effort if they would have been included in the model. For that reason, some simplifications of the geometry were performed: (i) a constant layer of 3 and 2 pixels was added to the original segmentation volume of the cranial and spinal SAS, respectively. This was the minimal thickness to ensure that all holes were filled in the 3D geometry. (ii) The complete geometry was smoothed using Mimics 24.0 and 3-Matic 16.0 (Materialise, Leuven, Belgium). It is important to note that these modifications cleared the blockage of CSF flow characterizing Chiari type 1 malformation. With a SAS thickness of minimally 4 mm at the level of the foramen magnum in the 3D model, the resulting geometry can be considered as representative of a healthy subject despite the starting data being of a patient with Chiari type 1 malformation.

### 3.1.2 Computational mesh

A computational mesh was generated using ICEM 2021 R2 (Ansys, Canonsburg, USA). The mesh was composed of tetrahedral and prismatic elements: tetrahedra occupy the largest part of the volume and three prism layers with a total thickness of 0.7 mm were created next to the walls to accurately resolve the laminar velocity profile. The tetrahedral mesh elements had a maximal seed size of 3 mm and a

refinement factor of 10 was applied. The thickness of each prism layer was determined by an exponential growth law with height ratio 2 and the total thickness. The filet ratio, maximal prism angle, maximal height over base, and prism height limit factor were set to 1, 180, 0.8, and 1 respectively. A mesh sensitivity study was executed for a stationary flow case with a constant velocity inlet of 0.4 ml/min and a zero pressure boundary condition at the interstitial outlet and outflow boundaries for the spinal, lymphatic, and arachnoid villi outlets with 20 %, 30 %, and 30 % of outflow, respectively. Hence, the interstitium outlet accounted for the remaining 20% of the outflow. These outflow percentages were arbitrarily selected with the assumption that arachnoid villi and lymphatic absorption are the main contributors to CSF absorption. The effect of the choice of outflow percentages was expected to be minimal with the bulk flow being 2 to 3 orders of magnitude lower than the pulsatile CSF flow. Spinal SAS pressure, wall shear stress, maximal velocity, and average pressure were evaluated for 13 meshes ranging from 0.3 to 5 million cells. Based on this study, the mesh with 1.18 million cells was selected which is the coarsest mesh with a maximal deviation of 5% compared to the finest mesh.

### 3.1.3 Boundary conditions

Boundary conditions are based on our current understanding of physiological processes impacting the CSF flow. An overview of the applied in -and outlet boundary conditions is depicted in figure 3.1.

#### *3.1.3.1 Inlet boundary conditions*

**CSF production**

At the lateral ventricles (see Figure 3.1A, zones indicated in blue), a constant velocity inlet of 5.57E-04 mm/s was imposed over a surface of 11 955 $mm^2$ to account for constant CSF production of 0.4 ml/min [34, 35]. The corresponding flow rate ($Q_{production}$) is presented as production in figure 3.1 and table 3.1.

**Cardiac pulsations**

Cerebral arteries undergo volume changes along the cardiac cycle and, in that way, induce pulsatile motion of the CSF as discussed in 1.2.2. Periodic brain tissue deformations in the hindbrain region have been attributed to volume variations of small pulsating arteries within the brain tissues. We, here, assume that these brain tissue deformations drive CSF motion through the cerebral aqueduct [31]. This effect was accounted for by adding a sinusoidal velocity waveform with a

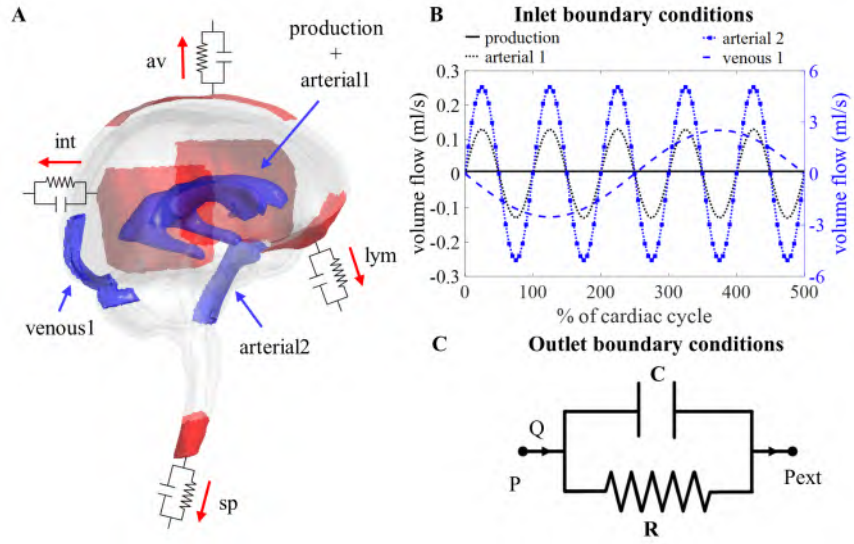


**Figure 3.1:** (A) Visualization of boundary conditions in the 3D model. Production and arterial1 designate the surface of the lateral ventricles (in blue), while arterial2 and venous1 point at the CSF volumes around the basilar artery and the cervical cerebral veins, respectively (in blue). The four outlet boundary conditions are designated in red and correspond to the interstitium (int), spinal (sp), lymphatic (lym), and arachnoid villi (av) outlets. (B) Graph containing the waveforms of the four different inlet boundary conditions depicted in (A). (C) Electrical circuit representing the 2-element windkessel model, which is imposed at the outlet boundary conditions, containing a resistance R and compliance C in parallel. A pressure difference $P - P_{ext}$ is created when a flow Q passes through the circuit.

frequency of 1 Hz and zero net flow to the constant CSF production. Following the conservation of mass, the flow amplitude of the sinusoidal signal ($Q_{arterial1}$) was derived from volumetric flow measurements at the level of the 3rd ventricle ($Q_{v3}$) reported by Sweetman et al. [128]. A value of 0.11 ml/s was selected and depicted as arterial1 in figure 3.1B and table 3.1.

$$Q_{arterial1} = Q_{v3} \tag{3.1}$$

Significant CSF displacements also appear anterior to the brainstem. We hypothesize that these displacements are caused directly by volume changes of the basilar artery along the cardiac cycle. These volume changes were implemented by adding a sinusoidal mass source term in the basilar artery region of the CSF (volume 9.53 ml). The amplitude of the corresponding volumetric flow $Q_{arterial2}$

caused by these volume changes was estimated from cervical ($Q_c$) and aqueduct ($Q_{v3}$) CSF flow measurements and the relative contribution of the spinal compartment to the total CSF compliance ($c_{sp}$) as depicted in equation 3.2.

$$Q_{arterial2} = \frac{Q_c - Q_{v3}}{c_{sp}} \tag{3.2}$$

Based on cervical measurements reporting arterial peak flows between 1.5 and 6 ml/s [122–124, 143], an average value of 3.5 ml/s was selected for $Q_c$ corresponding to a value of 5.06 ml/s for $Q_{arterial2}$ (arterial2 in figure 3.1B and table 3.1).

**Respiratory effects**

Recent studies have measured CSF displacements at the cervical level in response to respiration [47, 56]. These have been attributed to volume changes of veins that interact with the CSF. Therefore, venous volume changes were added as a pulsating 0.2 Hz source term with zero net flow in the fluid zone corresponding to the occipital cranial veins (venous1 in figure 3.1A and B, and table 3.1). The amplitude of the respiratory pulsations ($Q_{venous1}$) was considered 50% of the amplitude of the arterial pulsations based on the peak velocities reported by Yildiz et al. [56].

**Table 3.1:** Overview of average values (avg.) and amplitudes (amp.) of all the inlet boundary conditions.

| Name | Type | Avg. (ml/s) | Amp. (ml/s) |
|---|---|---|---|
| production | Constant | 6.67E-3 | - |
| arterial1 | Sine wave 1 Hz | - | 0.11 |
| arterial2 | Sine wave 1 Hz | - | 5.06 |
| venous1 | Sine wave 0.2 Hz | - | 2.53 |

#### *3.1.3.2 Outlet boundary conditions*

The model consisted of four outlets corresponding to the different CSF absorption pathways into the venous and lymphatic system: interstitial (int), spinal (sp), lymphatic (lym), and arachnoid villi (av) absorption pathway [1, 39, 144]. To account for both absorption resistance and CSF compliance, windkessel boundary conditions were imposed at each outlet. The 2-element windkessel models can be represented as an electrical analog containing resistance (R) and compliance (C) in parallel [145] as shown in figure 3.1C. Pressure ($P_i$) and flow ($Q_i$) at each outlet i were then related by

$$Q_i = \frac{P_i - P_{ext}}{R_i} + C_i \cdot \frac{d(P_i - P_{ext})}{dt} \tag{3.3}$$

where $R_i$ and $C_i$ are the resistance and compliance of outlet i, respectively and $P_{ext}$ corresponds to the external pressure which is in all cases set to zero [146].

**Formulation of windkessel models**

Resistance and compliance were accounted for by coupling a 2-element windkessel to each outlet of the CFD model. Therefore, the pressure at each outlet i was set following the differential equation coupling pressure and flow (see 3.4).

$$Q_{i,n} = \frac{P_{i,n}}{R_i} + C_i \cdot \frac{dP_{i,n}}{dt} \tag{3.4}$$

Because Fluent is a black-box solver, this differential equation cannot be solved simultaneously with the flow equations. Therefore, an explicit expression was derived by discretizing equation 3.4 over time following

$$\begin{cases} dt = \Delta t \\ dP_{i,n} = P_{i,n} - P_{i,n-1} \end{cases} \tag{3.5}$$

where $\Delta$t is the time step size, and $P_{i,n}$ and $P_{i,n-1}$ pressure in the current and previous step, respectively. This resulted in an expression of the pressure at outlet i in function of the outflow at timestep n and the pressure in the previous timestep n-1

$$P_{i,n} = \frac{Q_{i,n} \cdot R_i + P_{i,n-1} \cdot \frac{C_i \cdot R_i}{\Delta t}}{1 + \frac{C_i \cdot R_i}{\Delta t}} \tag{3.6}$$

where $C_i$ is the compliance and $R_i$ the resistance at outlet i. To couple this equation to the CFD solver for all outlets, the algorithm described in [147] and developed in the context of a fluid-structure interaction (FSI) problem, was adapted to control the interaction between the outlets with the pressure and flow governed by the windkessel formulation (equation 3.6). The coupling first determined the linearized relation between the flow rates and pressures at all outlets and then included this linearized model in the boundary conditions. This was to enable a strong implicit coupling of the pressure at the outlets and the fluid flow and overcome convergence issues that appeared with an explicit coupling scheme, ascribed to the very small spatial

pressure differences (order 0.01 mmHg) compared to large pressure differences over time (order 10 mmHg). Further details on the coupling algorithm are found in appendix A.

**Resistance values**

$R_{tot}$ was calculated as the ratio of the average ICP ($ICP_{avg}$) and the CSF production rate ($Q_{production}$). The average ICP was assumed 10 mmHg within the normal physiological range of 7-15 mmHg [7, 148, 149].

$$R_{tot} = \frac{ICP_{avg}}{Q_{production}} = 1500 \quad mmHg.s/ml \tag{3.7}$$

The four outlet resistances ($R_i$) were placed in parallel, contributing to total resistance as

$$R_{tot} = \frac{1}{\frac{1}{R_{int}} + \frac{1}{R_{sp}} + \frac{1}{R_{lym}} + \frac{1}{R_{av}}} \quad with R_i = \frac{R_{tot}}{q_i} \tag{3.8}$$

with $R_{int}$, $R_{sp}$,$R_{lym}$, and $R_{av}$ the interstitial, spinal, lymphatic, and arachnoid villi outlet resistances, and $q_i$ is the percentage of the total net outflow passing through the outlet i. The exact distribution of absorption via each of these outlets is debated. Only in recent years CSF absorption along other pathways than the arachnoid villi were identified, and studies reported lymphatic absorption ranging from 0 to 47% of the total CSF uptake [35, 144]. The outflow percentages imposed for the mesh sensitivity study were also used to calculate the absorption resistances. An overview of the resistance values is provided in table 3.2.

**Table 3.2:** Overview of average values (avg.) and amplitudes (amp.) of all the inlet boundary conditions.

| | Net outflow (%) | Resistance (mmHg.s/ml) |
|---|---|---|
| Outlet int | 20 | 7500 |
| Outlet sp | 20 | 7500 |
| Outlet lym | 30 | 5000 |
| Outlet av | 30 | 5000 |
| Total | 100 | 1500 |

**Compliance values**

The total compliance in the model is the sum of the compliances of each outlet ($C_i$), corresponding to capacitors placed in parallel.

$$C_{tot} = C_{int} + C_{sp} + C_{lym} + C_{av} \quad with \quad C_i = c_i \cdot C_{tot} \tag{3.9}$$

Here, $c_i$ is the contribution of outlet i (in %) to the total compliance. For the spinal outlet, this value was initially set to 66% based on in vivo reports with values ranging from 63 to 73% spinal compliance contribution for humans in lying position [45, 46]. The total compliance was estimated by calculating the difference between the maximal and minimal pressure over five cardiac cycles for compliance values ranging from 0 and 1.2 ml/mmHg. These compliance values were based on in vivo CSF compliance between 0.4 to 1.2 ml/mmHg as reported by [45, 46, 150, 151]. To avoid the need for a large number of 3D CFD simulations, a 0D model was used to estimate the five-second interval peak-to-peak pressure difference for multiple values of total compliance. Figure 3.2A shows a schematic of this 0D model. In this 0D model, the ICP was approximated assuming one inlet that combines all inflow boundary conditions, $Q_{in}$.

$$Q_{in} = Q_{production} + Q_{arterial1-2} \cdot sin(2\pi t) + Q_{venous1} \cdot sin(2\pi t \frac{f_{venous1}}{f_{arterial}}) \quad (3.10)$$

Here, $f_{arterial}$ is the arterial frequency of 1 $1/s$ and $f_{venous1}$ is the respiratory frequency of 0.2 $1/s$. The discretized expression in equation 3.6 was then adapted for one outlet to calculate pressure $P_n$ at time step n

$$P_n = \frac{Q_{in} \cdot R_{tot} + P_{n-1} \cdot \frac{C_{tot} \cdot R_{tot}}{\Delta t}}{1 + \frac{C_{tot} \cdot R_{tot}}{\Delta t}} \quad (3.11)$$

with $P_{n-1}$ is the pressure in the previous timestep and timestep size $\Delta$t set equal to 0.05 s. The compliance value $C_{tot}$ leading to ICP pulsations with an amplitude of 5 mmHg was then selected. This approach was applied for the calculation of compliance for cases A ($Q_{venous1}$ is zero) and B.

#### *3.1.3.3 Validation and boundary condition analysis*

Five different cases were set up to first validate the CFD simulation results for case A against reported literature data and then investigate the impact of respiration and compliance distribution on CFD simulation outcomes. Because in vivo PC-MRI measurements reported in literature were cardiac gated, only simulation results of case A validated against measurements. Meanwhile, the results of all cases were compared with reported ICP values. Table 3.3 shows an overview of inlet conditions and compliance distribution for the different cases.

- In case A, only production and cardiac pulsations were accounted for as inlet boundary conditions, thus discarding the impact of respiration. The total compliance was calculated following section 3.1.3.2 and distributed over the interstitial (int) and spinal (sp) outlet with contributions of 33 and 66%, respectively.
- In case B, respiratory effects were added to the inlet boundary conditions described in case A, while compliance distribution did not change. This addition led to a new value of total compliance, again calculated following subsection 3.1.3.2.
- In case C, we considered the same inlet boundary conditions and total compliance as case B but the compliance was distributed over all outlets with a contribution of 11, 66, 11, and 11% for the interstitial (int), spinal (sp), lymphatic (lym), and arachnoid villi (av) outlets, respectively.
- In case D, the only alteration compared to case B was the reversal of the compliance contributions of the interstitium (av) and spinal (lym) outlet by assigning 66 % of the total compliance to the interstitium and 33 % to the spinal outlet.
- In case E, inlet and outlet boundary conditions were kept the same as in case B but the total compliance was doubled.

**Table 3.3:** Overview of the inlet conditions with average (avg.) and amplitude (amp.), and distribution of and value of total compliance for cases A, B, C, D, and E.

| | **Case A** | **Case B** | **Case C** | **Case D** | **Case E** |
|---|---|---|---|---|---|
| **Inlet conditions (ml)** | | | | | |
| production avg | 6.67E-3 | 6.67E-3 | 6.67E-3 | 6.67E-3 | 6.67E-3 |
| production amp | - | - | - | - | - |
| arterial1 avg | - | - | - | - | - |
| arterial1 amp | 0.11 | 0.11 | 0.11 | 0.11 | 0.11 |
| arterial2 avg | - | - | - | - | - |
| arterial2 amp | 5.06 | 5.06 | 5.06 | 5.06 | 5.06 |
| venous1 avg | - | - | - | - | - |
| venous1 amp | - | 2.53 | 2.53 | 2.53 | 2.53 |
| **Compliance distribution (%)** | | | | | |
| int (cint) | 33 | 33 | 11 | 67 | 33 |
| sp (csp) | 67 | 67 | 67 | 33 | 67 |
| lym (clym) | - | - | 11 | - | - |
| av (cav) | - | - | 11 | - | - |
| **Compliance (ml/mmHg)** | | | | | |
| Total (Ctot) | 0.17 | 0.51 | 0.51 | 0.51 | 1.01 |

#### *3.1.3.4 Solver settings*

CSF was modeled as an incompressible Newtonian fluid with properties the same as water (density 998.2 $kg/m^3$ and dynamic viscosity of 0.001003 $kg/m/s$). The motion of the fluid was governed by the continuity and Navier-Stokes equations

$$\nabla \cdot \overrightarrow{v} = 0 \tag{3.12}$$

$$\rho \frac{\partial \overrightarrow{v}}{\partial t} + \rho \overrightarrow{v} \cdot (\nabla \overrightarrow{v}) = -\nabla p + \mu \nabla^2 \overrightarrow{v} \tag{3.13}$$

with the fluid density ($kg/m^3$), the velocity vector $\overrightarrow{v}$ ($m/s$), the fluid viscosity $\mu$ ($kg/m/s$), and the pressure field p ($Pa$). The effects of gravity were neglected and the flow was considered incompressible and laminar because of low Reynolds numbers, i.e., maximal order of 100 s (35 and 372 at the level of the cerebral aqueduct and cervical SAS respectively). The transient simulations were run using a PISO scheme and a finite volume method with 2nd order spatial discretization for momentum, standard for pressure, and 2nd order implicit temporal discretization. Under-relaxation factors were set to 0.5 for both pressure and momentum. An absolute convergence criterion of 1E-9 was imposed for all residuals (velocity in 3 spatial

directions, pressure). All simulations were run using a time step of 0.05 s. The central High Performance Computing infrastructure of Ghent University (HPC) was used for the simulations using up to 96 processor cores. Simulation of 25 cardiac cycles or a total simulation time of 25 s took about 14 hours to complete.

## 3.2 Results

### 3.2.1 Tuning total compliance using a 0D model

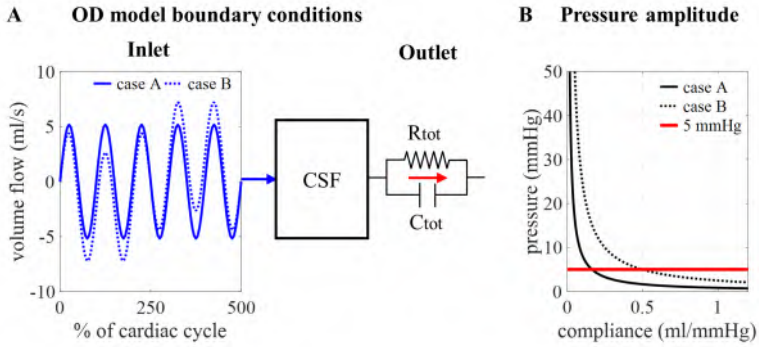


**Figure 3.2:** (A) Schematic of the 0D model assuming one inlet and one 2-element windkessel outlet. (B) Fitting compliance values for cases A and B using the 0D model. Pressure pulsation amplitudes for 1,000 compliance values ranging from 0 to 1.2 ml/mmHg (black curves) are visualized together with the targeted amplitude of 5 mmHg (red curve).

In figure 3.2B, the amplitudes of pressure pulsations are shown for 1000 compliance values ranging from 0 to 1.2 ml/mmHg as calculated using the 0D approximation. The cross-section of the two curves with the targeted amplitude of 5 mmHg corresponds with a compliance value of 0.17 and 0.51 ml/mmHg for cases A and B, respectively. With these compliance values, the ICP was calculated using the 0D model for 3000 cardiac cycles (figure 3.3 A) showing a transient phenomenon over time.

In the first five cardiac cycles (figure 3.3 B), the average pressure was 14.9 mmHg for case A compared to 7.7 mmHg for case B. In contrast, after 2000 cardiac cycles, average pressure approached the targeted average ICP for both cases (10.0 mmHg for case A and 9.9 mmHg for case B). In the next paragraphs, CFD simulation results were obtained using a total compliance of 0.17 ml/mmHg for case A, 0.51 ml/mmHg for cases B, C, and D, and 1.01 ml/mmHg for case E as presented in table 3.3.

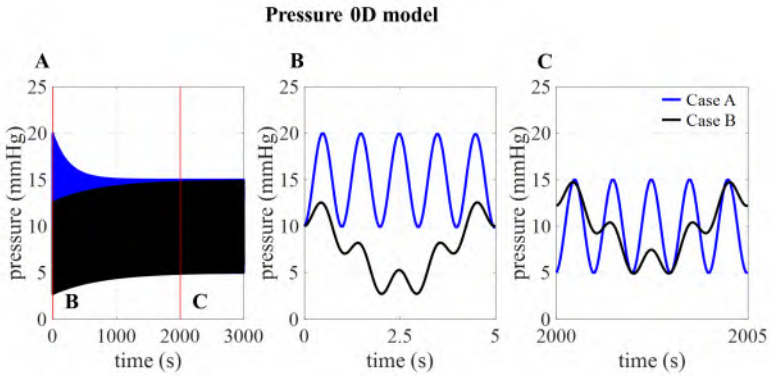


**Figure 3.3:** 0D prediction of pressure over 3,000 cardiac cycles for cases A and B and detail of pressure at (B) 0-5 s and (C) 2000-2005 s.

### 3.2.2 Validation against in vivo CSF flow measurements (Case A)

First, we consider the results corresponding with case A, thus without the inclusion of respiration. In figure 3.4, the calculated and measured CSF flow are visualized for two locations: the spinal SAS and the cerebral aqueduct. The amplitude of the pulsations in the cerebral aqueduct was both in vivo and in silico in the order of 0.1 ml/s whereas flow pulsations through the foramen magnum were in the range of 2 to 5 ml/s and thus more than 10 times larger than the flow through the cerebral aqueduct.

### 3.2.3 Impact of respiration on CSF dynamics (Case B)

#### *3.2.3.1 CSF flow*

Figure 3.5A shows the flow through a cross-section of the cerebral aqueduct and the spinal SAS simulated for 5 respiratory cycles and 25 cardiac cycles corresponding with case B. The inclusion of pulsations at the level of the ventricles and in the basilar region led to the fast pulsations of 1 Hz found in the cervical region, whereas slower fluctuations were induced by venous volume changes implemented at the location of the occipital cranial veins. The amplitude of the pulsations at the cross-section of the SAS was not only proportional to applied venous and arterial pulsations but also to the 66% spinal compliance contribution. In figures 3.5B and C the CSF velocities are visualized for 2 time points showing a clear direction switch of the velocity vectors along the respiratory cycle. Flow velocity through the cerebral aqueduct reached a maximal value of 1.2 cm/s.

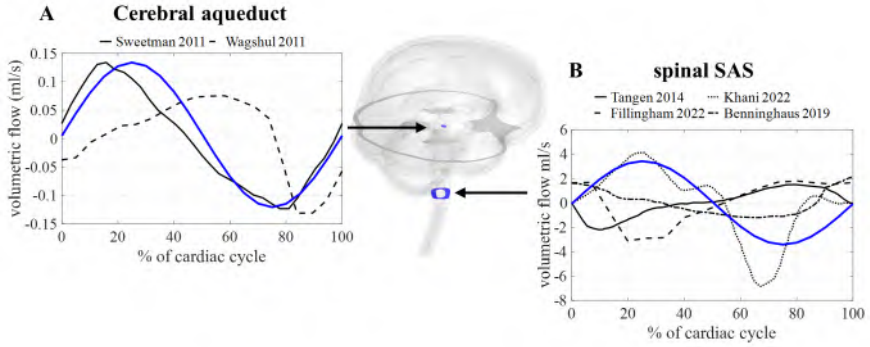


**Figure 3.4:** CFD simulation results (blue) and literature measurements (black) of CSF flow through 2 cross-sections: (A) flow through a cross-section of the cerebral aqueduct with literature values reported in and reproduced from [128, 152]. (B) Flow through spinal SAS space cross-section with literature values reported in and reproduced from [122–124, 143].

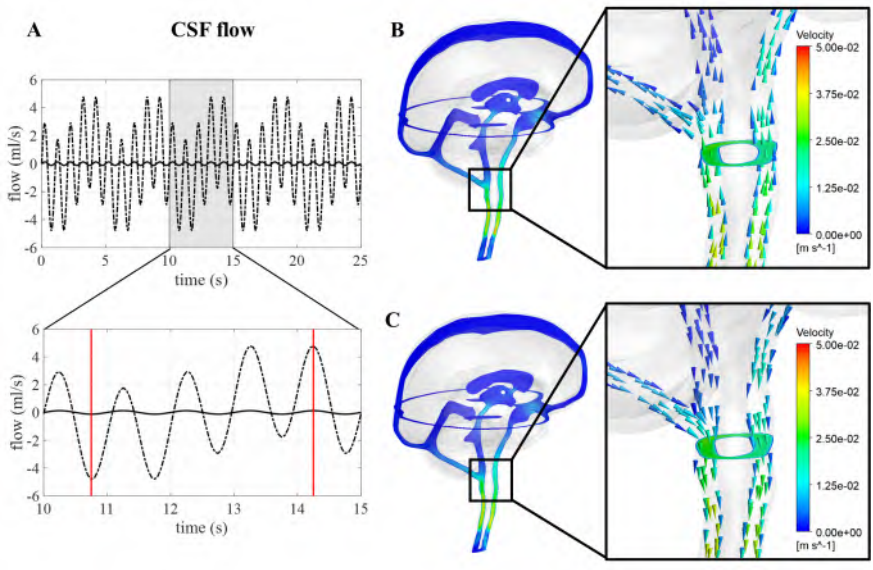


**Figure 3.5:** CSF flow and velocity simulations for case B. (A) CSF flow through a cross-section of the cerebral aqueduct and the spinal SAS for 25 s and then zoomed in for 5 s. (B) and (C) CSF velocities after 10.75 and 14.25 s, respectively.

### *3.2.3.2 CSF pressure*

ICP, corresponding with average pressure at the interstitial outlet (int), is presented over 25 s (Figure 3.6). Contours are visualized for 4 different time points in one respiratory cycle showing the spatial pressure differences with the pressure at the interstitial outlet (int) as reference. These spatial pressure differences were much smaller than the temporal pressure differences, which was expected from the low CSF flow velocities. Fluctuations of CSF flow led to spatial fluctuations of pressure in the spinal SAS following CSF pulsations.

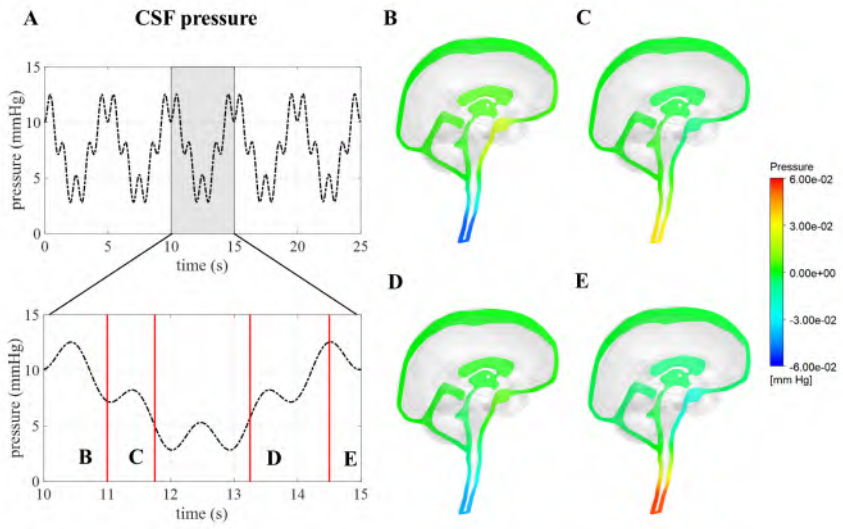


**Figure 3.6:** CFD pressure for case (B) A pressure averaged over the interstitial outlet over 25 s and then zoomed in on 5 s. (BE) pressure contours at 11, 11.75, 13.25, and 14.5 s, respectively.

Calculated pressures for cases A and B are visualized in Figure 3.7 for one cardiac cycle together with the average physiological range of 7-15 mmHg [7, 148, 149]. Also, the absolute threshold of 22 mmHg for ICP (recommended for management of traumatic brain injury [153, 154]) was added. The average pressure over 25 cardiac cycles was 14.8 mmHg for case A and 7.7 mmHg for cases B, C, and D compared to 14.9 and 7.7 predicted using the 0D model. Moreover, the amplitude of pressure pulsations was 4.96 mmHg for case A and 4.86 mmHg for case B.

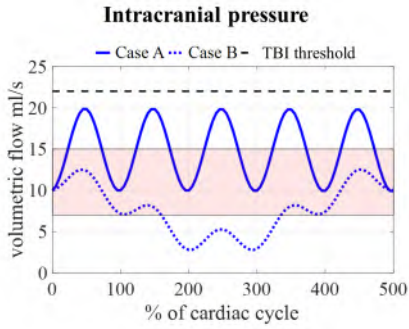


**Figure 3.7:** Model pressure for cases A and B is visualized together with the physiological range of 7-15 mmHg reported in [7, 148, 149] and the threshold for maximal pressure following the guidelines for traumatic brain injury (TBI) [153] for 5 cardiac cycles.

### 3.2.4 Impact of compliance magnitude and distribution (case B-E)

#### *3.2.4.1 CSF flow and pressure*

The flow through the cerebral aqueduct (Figure 3.8E) was identical for all simulations and did not change with compliance. Flow at the spinal SAS level (Figure 3.8D), however, was dependent on compliance distribution with a reduced contribution of spinal compliance in case D leading to reduced flow pulsations. Figure 3.8C presents the spatial difference in pressure between a point in the lateral ventricles and a point in the upper part of the spinal SAS. This pressure difference was only impacted by changes in the spinal compliance contribution. Here, an amplitude of maximal 0.032 mmHg was predicted for cases B, C, and E against 0.024 mmHg for case D. In contrast, doubling the intracranial compliance between B and E resulted in a reduction of average ICP as presented in figure 3.8B.

#### *3.2.4.2 CSF flows through outlets*

Figure 3.9B depicts the outflows for the three intracranial (int, lym, and av) and the spinal (sp) outlets. For case B, arterial and venous volume changes were accommodated by the spinal and interstitial outlet, whereas a flow following the pressure fluctuations was observed for the lymphatic and arachnoid villi outlets. Redistributing the compliance over all outlets in case C resulted in a pulsatile flow through all outlets. Further, the amplitude of the flow through the spinal and interstitial outlet was switched between cases B and D, where the spinal and interstitium compliance contributions were changed

as summarized in table 3.3. Finally, no difference in outflow was predicted between cases B and E.

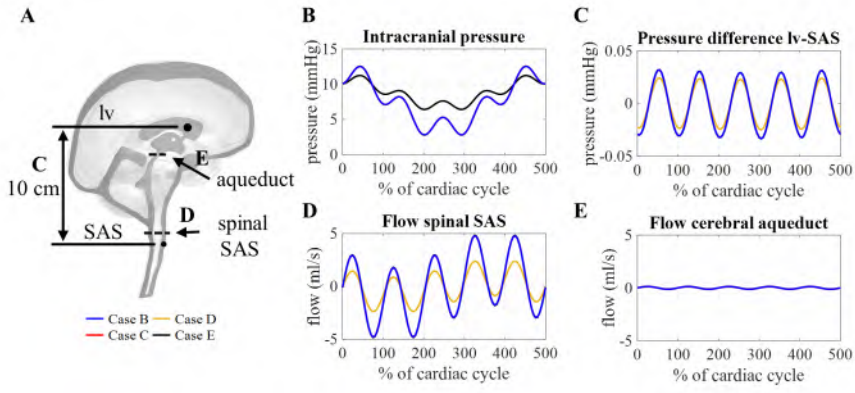


**Figure 3.8:** (A) Sagittal cross-section CSF depicting the location of aqueduct cross-section B, spinal SAS cross-section D, and 10 cm distance between a point in lateral ventricles (lv) and spinal SAS (SAS) C. Simulation results for cases B, C, D, and E : (B) ICP corresponding to interstitial outlet (int), (C) spatial pressure difference between a point in lateral ventricle and spinal SAS, (D) and (E) flow through a cross-section of the spinal SAS and cerebral aqueduct, respectively.

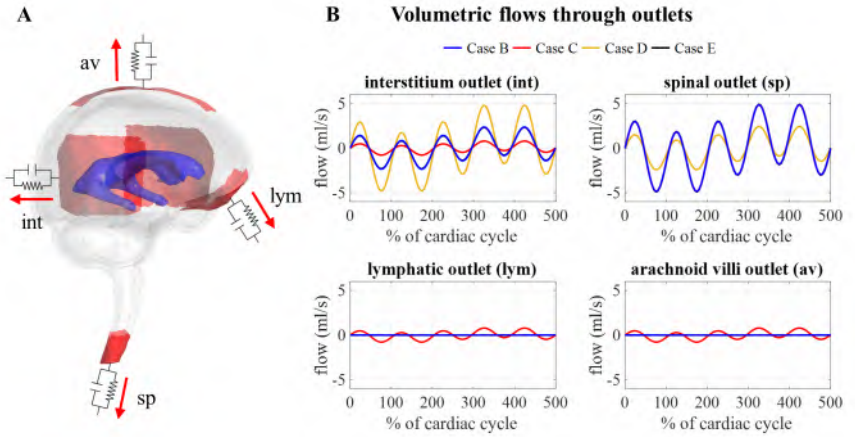


**Figure 3.9:** flow obtained at each outlet for different values of compliance corresponding. (A) visualization of outlets with windkessel boundary conditions. (B) graphs showing the flow through the interstitium, spinal, lymphatic, and arachnoid villi outlet for cases B, C, D, and E.

## 3.3 Discussion

A computational fluid dynamics model of the CSF was presented where fluid pressures and flow were reproduced through the implementation of physiological boundary conditions. First, a 0D model was used to define an adequate value of total compliance by simulating pressure for different compliance values and then selecting the value yielding physiological pressure pulsations. Different compliance values were obtained for case A without and case B with respiration effects. Interestingly, it was only when considering the effects of respiration that we obtained a compliance value within the range derived from in vivo measurements (0.4 to 1.2 ml/mmHg) [45, 46, 150, 151], suggesting that discarding respiration leads to an underestimation of the intracranial compliance. The amplitude of pressure pulsations predicted by the 3D model deviated 1% for case A and 3 % for case B from the targeted 5 mmHg amplitude, which can be attributed to the simplifications in the 0D model having only one inlet compared to the spatial distribution of the inlets and outlets in the 3D model.

Since MRI data reported in previous studies are typically obtained through cardiac-gated MRI acquisition, only simulation results without respiratory influences (case A) were compared to in vivo obtained flow values. Here, fluid flow across a cross-section of the cerebral aqueduct and the spinal SAS showed a good agreement with reported PC-MRI measurements in the third ventricle and cerebral aqueduct [128, 152] and the spinal SAS [122–124, 143], respectively (see figure 3.4). This showed the effectiveness of the presented approach in obtaining physiological peak flow rates but also indicated differences in the timing of those peak flows between the measured and simulated profiles. Adding respiration resulted in a pulsatile flow pattern across the foramen magnum with, evidently, the appearance of pulsations at the imposed frequencies (Figure 3.5) of 1 (cardiac) and 0.2 Hz (respiration). Maximal velocities at the cerebral aqueduct were 1.2 cm/s, which was in the same order of magnitude as velocity measurements reported in Matsumae et al. [31]. However, these velocities were lower than those presented in computational studies with maximal velocities of 2.4 cm/s [128] and 2 cm/s [124] in the cerebral aqueduct, and in vivo measurements of 3-4 cm/s reported for a reference cohort in Eide et al. [155].

We assumed that the average pressure is determined by the absorption resistance and production rate, and consequently setting the proper absorption resistance should return the targeted mean pressure (10 mmHg). However, in the simulations, time-average pressures

of 14.8 mmHg for case A and 7.7 mmHg for case B were obtained at the interstitial outlet (int). This was because the simulations were only run for 25 cardiac cycles to save computational time. The 0D results, presented in figure 3.3, showed that for both cases A and B average pressure evolved toward a steady state after only 2000 cardiac cycles yielding an average of 10 mmHg, the targeted mean ICP. It was, however, not feasible to do these long simulations using the 3D CFD model. Nevertheless, CFD average pressures still lay within the physiological range (figure 3.4), which is typically considered 7-15 mmHg [7, 148, 149], and below the absolute threshold of 22 mmHg recommended for management of traumatic brain injury in 2017. This absolute threshold was selected because a significant rise in mortality of traumatic brain injury patients was observed when an ICP higher than 22 mmHg was sustained for five days [153].

The possibility to obtain absolute CSF pressures and velocities simultaneously (figure 3.5 and 3.6) was an important advantage of this model over previous CFD models that did not provide absolute pressures [120, 124]. Meanwhile, the FSI model by Sweetman et al. [128] simulated CSF pressure over time with an average pressure of about 575 Pa (4.3 mmHg) and a maximal pressure difference of 175 Pa (1.3 mmHg). They predicted maximal spatial pressure differences of 0.2 mmHg between the lateral ventricles and the cervical spinal SAS, which was nearly 10 times larger than the pressure differences of 0.024 mmHg (case A) and 0.032 mmHg (case B) obtained in this study. In contrast, the CFD model by Fillingham et al. [124] reported maximal pressure differences of 7 Pa or 0.05 mmHg over the cranial CSF space. In vivo pressure measurements in patients with idiopathic normal pressure hydrocephalus indicated a maximal pressure difference between the subdural space and the lateral ventricles of 1 mmHg/m or 0.1 mmHg difference between the ventricles and foramen magnum (10 cm) [156]. Thus, both our model and the CFD model by Fillingham et al. [124] seem to underpredict, while the FSI model by Sweetman et al. [128] appears to overpredict the spatial pressure differences. The lower pressure difference in our model might be attributed to the larger diameter of the cerebral aqueduct in our model compared to the physiological diameter. Also, it should be noted that pressure differences in patients with Hydrocephalus might differ from normal physiological conditions.

Multiple windkessel outlets enabled modeling a heterogenous CSF compliance and absorption, which are thought to be impaired in different types of hydrocephalus [157, 158]. The inclusion of resistances

allowed us to steer absorption through four different outlets, thereby, no longer ignoring system-wide absorption in both the lymphatic and venous systems. To the best of our knowledge, this was the first 3D computational study to include both venous and lymphatic absorption, and a heterogeneous compliance distribution over the spinal and intracranial compartments. The total CSF compliance was found to impact the overall CSF pressures, whereby an increase in total compliance reduced the amplitude of pressure pulsations (figure 3.8 B). Moreover, simulation outcomes indicated that the location and distribution of compliance impact CSF flow. The amplitude of flow through each outlet was proportional to the contribution of that outlet to the total compliance. Consequently, the distribution of compliance could impact the flow through the spinal SAS as observed in figure 3.8D when switching the spinal and intracranial compliance from case B to case D. These results suggested that adequate distribution of compliance is important to predict physiological CSF flows.

### 3.3.1 Limitations and future perspectives

First, the simulation results were validated by comparison to literature data, which were recorded at a limited number of points or planes in the CSF space. Also, these are typically obtained through cardiac-gated acquisition only, meaning that the measurements are not real-time and respiration information is not quantified. In that way, they do not account for respiratory effects. Therefore, only simulation results without respiratory influences (case A) were compared to flow measurements. Pressure recordings presented are typically acquired in the context of traumatic brain injury [7, 153] or hydrocephalus [151] and may not reflect normal physiological pressures. Recordings in subjects with physiological ICP would allow for expanding our validation. The parameters in our model including inlet boundary conditions, resistance, and compliance, can easily be adapted once more measurement data becomes available. Our data indicated that the boundary conditions can be optimized to simultaneously obtain pressure and velocities in the physiological range.

Further, this model included some important simplifications. First, the currently used 3D geometry was simplified to overcome the limited resolution of the original scan (slice thickness of 3 mm) and reduce complexity to limit computer time. Second, the model geometry was obtained from clinical MRI images of a patient with Chiari type 1 malformation. However, above mentioned simplifications of the CSF geometry resulted in a CSF layer at the level of the foramen magnum of minimally 4 mm, hereby removing the

obstruction from the segmented geometry. As such, simulations were representative for a healthy subject, rather than for a patient with Chiari malformation. Third, the locations of the veins and arteries were limited to three locations and the morphology of the boundary surfaces was loosely based on literature. Fourth, the inlet boundary conditions were simplified to sinusoidal time signals with a constant value over the complete inlet surface. Last, CSF absorption and volume compensation mechanisms within and beyond the simulated 3D space were simplified by introducing windkessel models at the outlets. These models were distributed, yet still implemented at a discrete and limited number of sites. The distribution of compliance (for case B) was based on in vivo measurements [45, 46]. However, the absorption percentages were arbitrarily selected because of the current lack of quantitative in vivo data. Yet, the effect of the outflow percentages was minimal with bulk flow being 2 to 3 orders of magnitude lower than the pulsatile CSF flow and leading to pressure differences between the outlets in the order of 1E-5 mmHg compared to pressure differences in the order of 0.01 mmHg due to pulsatile CSF flow. It is, without any doubt, more physiologically correct to use an FSI approach to account for compliance effects arising from the deformability of the tissues surrounding the simulated 3D fluid spaces, as demonstrated by among others [110]. As such, although FSI models are computationally more complex and require adequate material models and properties for brain tissues, future research should aim to include FSI to achieve more physiological fluid displacements across the simulated 3D space.

Despite these simplifications and assumptions, this model is a proof of concept that by setting proper boundary conditions, thus inlet and windkessel boundary conditions in a 3D model of the CSF, one can obtain pressures and velocities within the physiological range. Now, the model can be stepwise optimized, including more detailed information on the neural anatomy and physiology. Toward the future, we aim to apply this framework to neurological disorders with known disruptions of CSF pressure and flow and to expand validation with subject-specific in vivo measurements of flow and brain tissue motion.

## 3.4 Conclusion

A CFD model of the 3D CSF space was developed. In this model, we implemented the physiological processes of CSF production and absorption, arterial and venous volume changes, and CSF compliance

distributed over the CSF domain. This approach yielded CSF pressures and velocities within the physiological range and enabled the evaluation of the impact of the magnitude and the distribution of the CSF compliance. We found that tuning the magnitude of compliance using a 0D model is an effective strategy to obtain CSF pressure pulsations within the targeted range, whereas the obtained volumetric flow rates depend on the tuning of the input flow rates and the spatial distribution of compliance over the CSF domain.

Chapter 4

# Implementing amplified MRI acquired motion

In chapter 3, brain tissue motion in the midbrain region was incorporated through simplified sinusoidal inflow boundary conditions in the lateral ventricles based on literature data for measured CSF flow. However, brain tissue motion can also be measured in vivo using aMRI. In this chapter, we evaluate the feasibility of deducing brain tissue motion from amplified MR images and in turn using this motion in subject-specific CFD models.

This chapter is based on the manuscript with title *"Evaluating amplified MRI as an input for computational fluid dynamics models of the cerebrospinal fluid"* in preparation for submission.

## 4.1 Introduction

Cerebrospinal fluid (CSF) dynamics are complex and can be seriously altered in neurological disorders such as Chiari type 1 malformation and hydrocephalus [58, 159]. Computational models that accurately capture CSF dynamics can serve as valuable tools to understand the pathophysiology of neurological disorders and to evaluate the effects of clinical treatments such as shunt placement and drug delivery [9, 83]. However, the selection of adequate boundary conditions for these models is challenging as it requires a detailed understanding of the processes impacting CSF dynamics, which is currently lacking.

In the last decades, several studies have used CFD to study CSF dynamics in the ventricular system. Kurtcuoglu et al. initially modeled wall motion of the third ventricle as the sole driver of CSF motion [101]. Here, they assumed that the third ventricle acts as a CSF pump, which contracts with the expansion of the thalami during systole as previously suggested by Boulay and OConnell [160, 161]. However, in a later study, the authors did not find a significant contribution of head-feet motion of the third ventricle to the net CSF flow [102]. Meanwhile, Linninger et al. [125] and Howden et al. [103] assumed that the choroid plexus was the primary source of CSF flow in the ventricular system and therefore implemented pulsatile boundary conditions at the choroid plexus sites. This assumption was questioned because in vivo MRI studies did not show any significant acceleration around the choroid plexus sites of the lateral ventricles [31]. More recently, studies investigated the impact of ependymal cilia and indicated a significant contribution of these structures in local CSF motion [106, 111]. Hence, the selection of boundary conditions between studies has been diverse. This diversity in boundary conditions exists because the exact mechanisms driving the pulsatile motion of CSF are not completely understood [9]. In general, rhythmic displacements of CSF are induced by volume changes of blood vessels in the cranium following respiration and cardiac pulsations [56]. Less clear is how and where these volume changes are transferred to CSF motion. These volume changes could be transferred directly to the CSF or indirectly through small arteries causing volume changes of the parenchyma [162].

In vivo measurements of CSF flow and brain tissue motion can help us to better understand CSF motion and optimize boundary conditions of computational models. PC-MRI is the most frequently used method for direct measurement of CSF flow and allows the detection of CSF velocities perpendicular to the measurement planes (e.g., cerebral aqueduct, foramen magnum) [78]. These measurements can serve as a basis for input boundary conditions in CFD models as presented in chapter 3 and other works [113, 120, 124]. Measurement of the periodic displacement of the CSF-brain boundary is more challenging because of the small and complex deformations of brain tissues. Frequently used techniques for measuring this displacement are DENSE [163] and PC-MRI [81].

An alternative MRI technique for measuring deformations is aMRI, which uses a phase-based post-processing technique to amplify

sub-voxel motion in cine MRI images and in that way enables visualization of amplified brain tissue motion [164, 165]. Important advantages of this technique are the short scan times, the high spatial resolution, high signal-to-noise ratio, and the visualization of smaller motion [80, 166]. Moreover, due to the amplification, brain motion can be observed visually, and thus complex deformations of the CSF domain can be readily extracted. Nevertheless, to the best of our knowledge, this technique has only been used qualitatively to identify differences in brain motion between healthy subjects and patients [166, 167].

In this study, we evaluate the use of brain tissue motion deduced from aMRI for the prediction of CSF dynamics in the ventricular system. Therefore, we directly impose the tissue motion in a CFD model of the ventricular system and compare the resulting CSF flows with those obtained by imposing inflow boundary conditions based on PC-MRI measurements to make a first assessment of the physiological deformations of the ventricles.

## 4.2 Methods

### 4.2.1 Image acquisition and processing

MR brain images of a healthy subject were acquired using a 3T MRI scanner (SIGNA Premier; General Electric Healthcare) with AIR 48-channel head coil at the medical research institute M$\bar{a}$tai in Gisborne, New Zealand. Ethical approval for this study was obtained through the New Zealand Health and Disability Ethics Committee (20/CEN/107), with informed consent of all subjects. Data collection included a sequence of PC-MRI slices at the level of the cerebral aqueduct and a 3D volumetric (FIESTA) MRI sequence of 20 whole-brain cine images retrospectively reconstructed to one heartbeat. Peripheral pulse measurement was used to trigger data collection at the beginning of each cardiac cycle and retrospectively bin the data to 20 and 30 cardiac phases for the cine MRI and PC-MRI datasets, respectively. An encoding velocity of 16 cm/s and 0.7 mm isotropic in-plane resolution were selected for the PC-MRI dataset. In vivo CSF flow was extracted using Circle CVI42 (Circle Cardiovascular Imaging, Calgary, Canada). Meanwhile, the cine images were obtained with slice increment 1 mm, in-plane pixel size 0.875, field of view 224 x 224 mm, matrix size 256, repetition time 3.084 ms, echo time 1.156 ms, and flip angle 25°.

The cine MR images were post-processed using the 3D aMRI algorithm pipeline outlined in Terem et al. [165] and Abderezaei et al.

[167]. In brief, the algorithm first decomposes the original cine images using a 3D steerable pyramid, which results in amplitudes and phases at different scales and orientations. The phases of the decomposition are subsequently separated from the amplitude component, and independently temporally band pass filtered to select a desired range of motion frequencies (here the cardiac frequency), followed by noise filtering and amplification. The resulting phases are added back to the original phases and finally combined with the amplitude data to create the 3D aMRI images. In this study, an amplification factor of 30 was used.

### 4.2.2 Segmentation

The deforming CSF domain was extracted from the resulting aMRI sequence using the open-source segmentation software 3D slicer 5.4.0. The geometry of the ventricular system was first extracted from the image volume corresponding with the first reconstructed timestep in one cardiac cycle (timestep 0). The segmentation process for this timestep consisted of three main steps as depicted in 4.1.

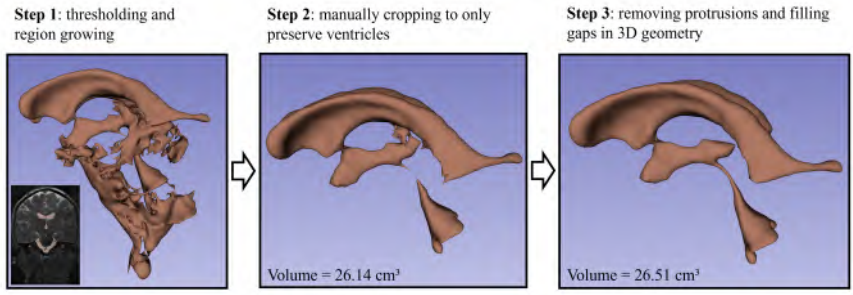


**Figure 4.1:** Segmentation of geometry in three steps.

Step 1 involved the extraction of the initial volume by first selecting voxels through thresholding (grey value: 5800) and then separating the ventricles from other fluid regions by using the islands option in 3D slicer, which divides the volume into interconnected components. It can be observed that the interthalamic adhesion could not be extracted from the MRI data. This does not mean this feature of the third ventricle is not present, rather the contrast and/or resolution of the MRI scan in that region was insufficient to distinguish between CSF and brain tissue. In step 2, the regions that did not belong to the ventricular system were removed to only preserve the ventricular system. Finally, in step 3, the geometry was smoothed by manually removing protrusions, restoring the aqueduct, and automatically

filling gaps using a kernel size of 1 mm. A volume change of 1.4 % was induced by adjustments in step 3 compared to step 2. The volumes of the ventricles for the next 19 timesteps were then obtained using the slicer extension Sequence Registration, which is available as a module in 3D Slicer, and allowed tracking the deformation of the ventricular volumes over time. The resulting 20 segmented volumes were exported as STL files. Figure 4.2 depicts the volumes of the ventricles for three different time points to visualize the deformations.

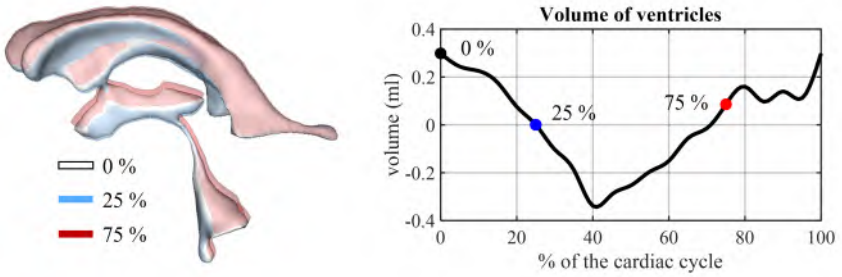


**Figure 4.2:** Visualization of STL files using Mimics (Materialize, Leuven, Belgium) at 0, 25 and 75 % of the cardiac cycle corresponding with volumes of 26.09, 25.80 and 25.88 ml, respectively. This demonstrates that arterial pulsations undergo both translations (rigid body motion) and volume changes between timesteps.

### 4.2.3 Generating computational volume mesh

The computational mesh was generated in ICEM CFD 2023 R2 (Ansys, Canonsburg, USA) using the STL file corresponding with timestep 0. To avoid the need for interpolation in space when the tracking deformation, the original distribution of points, as stored in the STL, was used to generate the surface mesh. The triangular surface mesh based on the STL data has a minimal quality above 0.2, which was deemed sufficient. To preserve the surface mesh, the volume mesh was constructed using the Delaunay method, without smoothing, and consists of 349 074 tetrahedral cells. Less than 0.023 % of the cells have a quality below 0.2. In general, the quality is based on the cells aspect ratio as discussed in the user manual of ICEM CFD 2023 R2 (Ansys, Canonsburg, USA) for triangular and tetrahedral cells.

### 4.2.4 Implementation in CFD solver

The model was implemented by importing the computational volume mesh in the finite volume solver Fluent 2023 R1 (Ansys, Canonsburg,

USA). CSF was considered as a fluid with properties of water (density 998.2 $kg/m^3$, dynamic viscosity 0.001003 $kg/m/s$) and the flow was considered laminar because of previously reported CSF Reynolds numbers in the order of 100ths (see chapter 3). The transient simulations were run using a PISO scheme and a finite volume method with 2nd order spatial discretization for momentum, standard for pressure and 2nd order implicit temporal discretization. Under-relaxation factors were set to 0.3 for pressure and 0.7 for momentum for all simulations.

#### *4.2.4.1 Mesh motion*

The deformations obtained from aMRI were implemented as mesh motion using a dedicated Python algorithm and a user-defined function (UDF). An overview of the workflow is shown in figure 4.3.

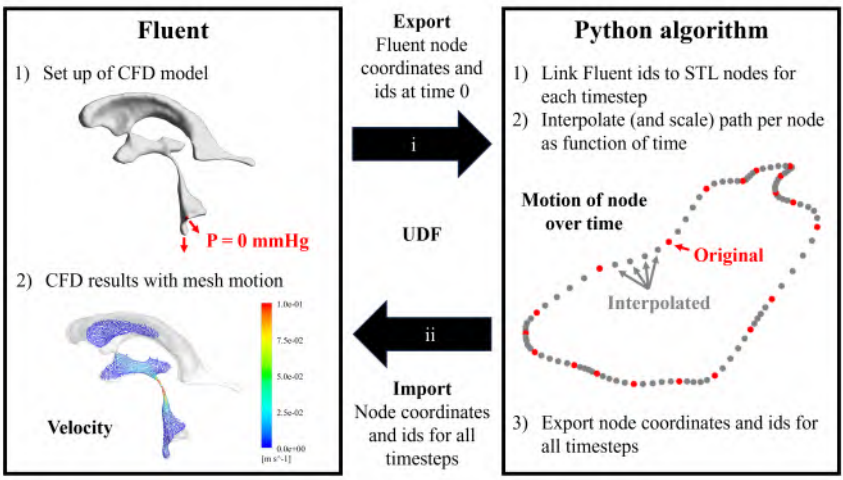


**Figure 4.3:** Workflow for CFD model and implementation of mesh motion.

The UDF was an adjusted version of the file used in the fluid-structure interaction code CoCoNuT (github.com/pyfsi/coconut) [168, 169]. The UDF enables (i) exporting unique node ids and coordinates of the computational mesh and then (ii) prescribing mesh motion by reading node coordinates and imposing them to the mesh at every time step. Unique nodes allow identifying each surface node of a computational mesh, which was essential when prescribing the motion of each unique node. The Python algorithm was used to couple the node coordinates in the STL files with the corresponding node ids of the computational mesh. In this algorithm, the nearest neighbor approach (specifically KTDtree of the sklearn.neigbors

Python package) was used to find for each node of the computational mesh the location of that node in the original STL file (timestep = 0). We used this location information to add unique node ids to the nodes in the STL files for all timesteps. The original data consisted of only 20 timesteps and we assumed the total time per cardiac cycle to be 1 s. To reduce the timestep size, the transitioning point data was interpolated in time (by adding points to the trajectory of each node) using a piecewise-defined cubic polynomial to finally obtain 100 timesteps. The resulting information about the position of the nodes was then imported in Fluent at each timestep to impose mesh motion.

Because deformations were obtained from aMRI sequences, the deformations and thus also the volume changes were expected to be larger than the CSF displacements occurring in vivo. Therefore, three different scaling factors (1/2, 1/4, and 1/8) were considered to reduce the displacement of each mesh point.

#### *4.2.4.2 Boundary conditions*

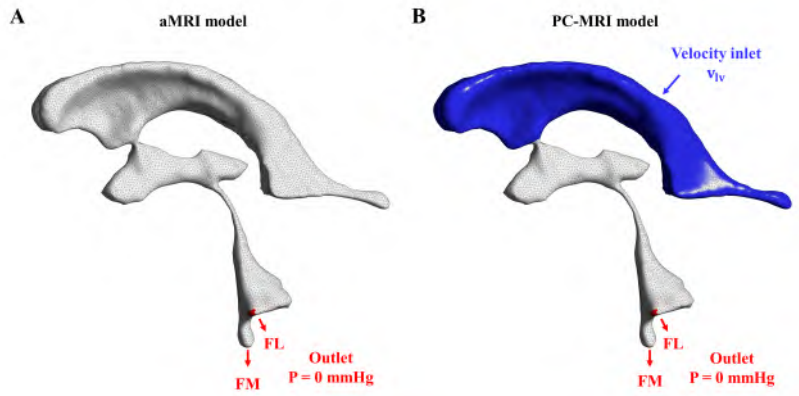


**Figure 4.4:** Boundary conditions of (A) aMRI model with imposed mesh motion and zero pressure outlet boundary conditions at the foramina of Luschka (FL) and Magendie (FM), and (B) PC-MRI model with a velocity inlet based on PC-MRI measurements in the cerebral aqueduct and zero pressure outlet boundary conditions. Inlet and outlet boundary conditions are indicated with blue and red arrows, respectively.

Zero pressure was imposed at three outlets corresponding to the connections of the ventricular system with the SAS: the foramen of

Magendie (ML) and the two lateral connections making up the foramina of Luschka (FL). To allow comparison between the flow velocity fields based on PC-MRI and aMRI, a second model was set up with the same three outlets but with the domain deformation replaced by a velocity inlet in the lateral ventricles. Here, the inlet velocity ($v_{lv}$) in lateral ventricles was calculated by dividing the measured flow rate from PC-MRI in the cerebral aqueduct ($Q_{aq}$) by the surface area of the lateral ventricles ($A_{lv}$). Figure 4.4A and B visualize the inlet and outlet boundary conditions imposed in the model with the aMRI motion (aMRI model) and the PC-MRI-based inlet velocity (PC-MRI model), respectively.

#### *4.2.4.3 Solver settings*

The simulations were run for one cardiac cycle of 1 s and the aMRI and PC-MRI model took respectively 6.5 and 10 minutes to complete. Solver settings included standard and second order upwind spatial discretization of pressure and momentum, respectively. Furthermore, the pressure-volume coupling was realized using a PISO scheme and a second order implicit formulation was used for time discretization. Absolute convergence criteria of 0.001 and 1E-6 were imposed for continuity and velocity (x, y, and z), respectively. To absorb the motion of the surface mesh, the smoothing method linearly elastic solid was used.

## 4.3 Results

### 4.3.1 Volumetric changes induced by deformation of the ventricles

Motion of the ventricular walls induced pulsatile changes in the volumes of the ventricles as depicted for the lateral (LV), third (V3), and fourth ventricle (V4) in Figure 4.5B and C. Here, volume changes are presented relative to the mean volume. We observe that the different ventricles reach a maximal volume at different time points, with a maximal volume at time 0.75, 0.76 and 0.11 s for the 4th, 3rd, and lateral ventricles, respectively. This corresponds to a time delay compared to the time of the maximal volume of the 4th ventricle of 1 % for the 3rd and 35 % for the lateral ventricles expressed in % of the total cardiac cycle.

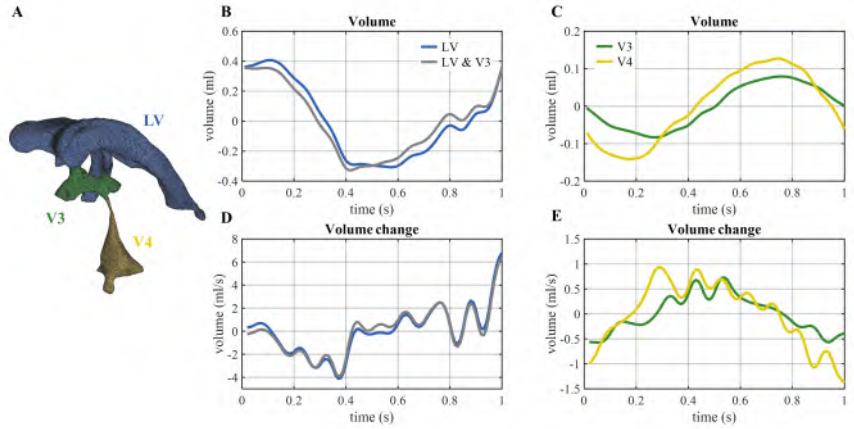


**Figure 4.5:** (A) Visualization of the volumes of the ventricles with their time-dependent volumes relative to their mean volumes depicted in (B) and (C) and the corresponding discretized volume differentials calculated following equation 1 in (D) and (E).

The ventricular volumes over time can also be used to calculate the corresponding differentials which represent the flow in and out the different ventricles. The calculation of these volume changes over time is depicted in equation 4.1.

$$\frac{dV}{dt} = \frac{V_n - V_{n-1}}{\Delta t} \tag{4.1}$$

Here, $\Delta t$ is the timestep size, and $V_n$ and $V_{n-1}$ are the volumes at the current and previous timestep, respectively. These instantaneous

volume changes were plotted over time in Figure 4.5D and E with negative values indicating CSF being forced out of the ventricles. Accordingly, a maximal flow rate of 3.92 ml/s was expected to be forced through the cerebral aqueduct during systole when imposing mesh motion based on aMRI for the third and lateral ventricles.

### 4.3.2 CSF dynamics in response to scaled aMRI deformations

First, to ensure that outflow rates were not affected by motion of the outlet and thus rigid bulk motion of the whole ventricular system, the volume changes as calculated in section 4.3.1 were first compared with simulated outflow rates obtained without scaling. We found a good match between both profiles as depicted in figure 4.6.

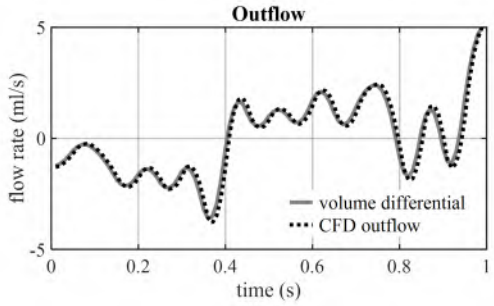


**Figure 4.6:** Flow through the outlet obtained by calculating the discretized volume differentials and extracted from the model output of the CFD model imposing the non-scaled aMRI motion.

Figure 4.7A depicts the flow rates through the cerebral aqueduct obtained by imposing deformation based on aMRI. The aMRI deformations were scaled with factors 1/2, 1/4 and 1/8, which corresponded with pulsatile amplitudes of 2.61, 1.30 and 0.65 ml/s, respectively. Scaling with a factor 1/8 led to an aqueduct flow rate closest to 0.51 ml/s, which is the flow rate measured in the cerebral aqueduct with PC-MRI. Therefore, CFD results are presented for deformations scaled with a factor 1/8. Figure 4.7B shows CSF flow in the caudal direction in the first half of the cardiac cycle and dominantly in the cranial direction in the second half. The same pattern and closely matching flow rates were observed for the flow through the foramina of Monro and the outlet as depicted in Figure 4.7D.

To compare aMRI and PC-MRI-based simulations, velocity vectors corresponding to aMRI deformation and PC-MRI inflow were

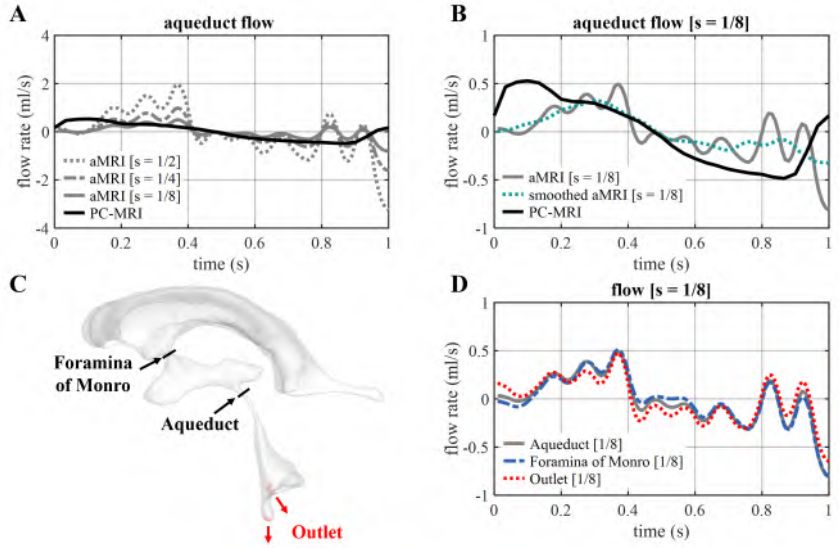


**Figure 4.7:** (A) Flow rate through the cerebral aqueduct obtained after imposing the aMRI deformation which was scaled with factor 1/2, 1/4, and 1/8 and compared with in vivo flow measurements. (B) Flow rate through the cerebral aqueduct after scaling aMRI deformations with factor 1/8 visualized together with moving mean smoothing with 25 timesteps and in vivo flow measurement (PC-MRI). (C) Visualization of locations of planes of interest. (D) For scaling factor 1/8, flow through cerebral aqueduct, foramina of Monro and the outlet.

plotted at three different time points in Figure 4.8A and B, respectively. For both models, maximal velocities of the order 0.1 m/s appeared in the cerebral aqueduct. Whereas the general flow patterns at the selected time points were similar, differences in local flow patterns and recirculation appear in the third and fourth ventricles. Finally, the corresponding pressure distributions are depicted in Figure 4.9 indicating pressure differences at these time points in the order of 0.5 and 1 mmHg for the PC-MRI and the aMRI model, respectively.

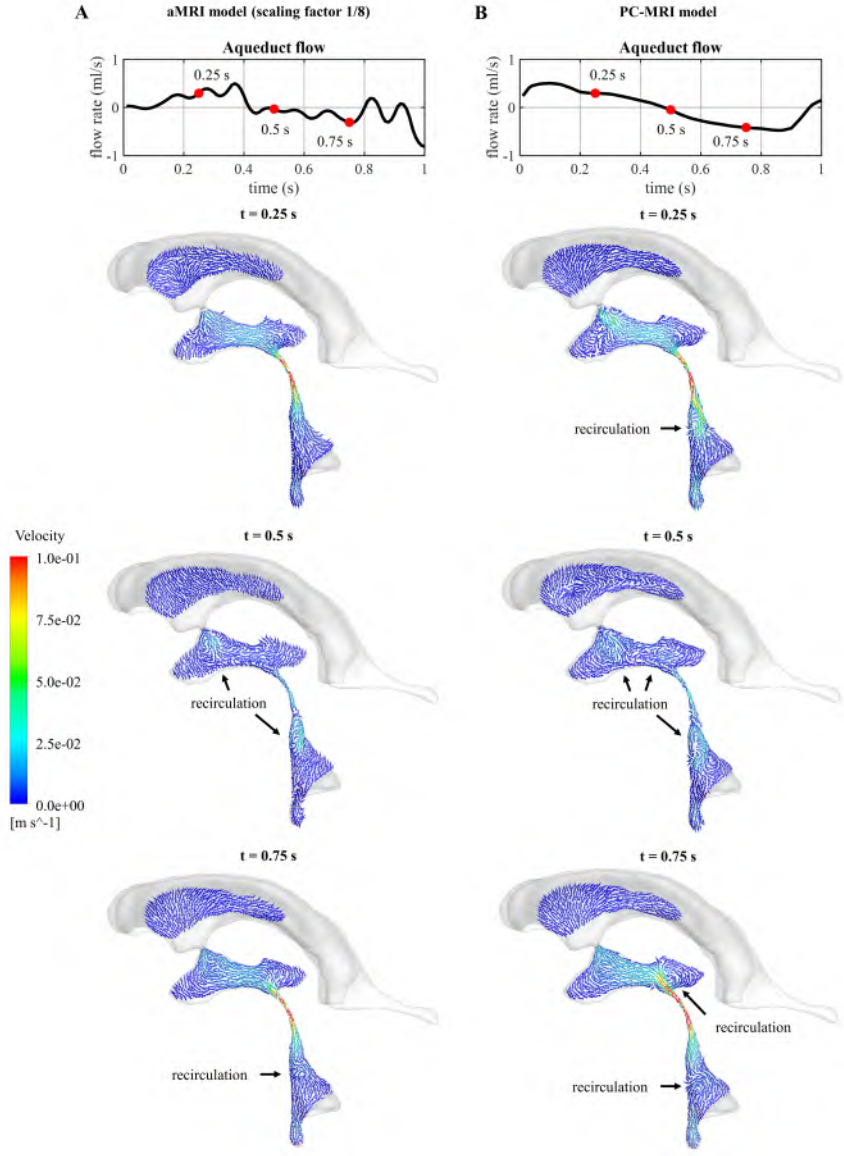


**Figure 4.8:** Visualization of aqueduct flow and velocity vectors at three different time points (A) for aMRI-based deformation scaled with factor 1/8 and (B) corresponding with the PC-MRI measurements imposed at the wall of the lateral ventricles.

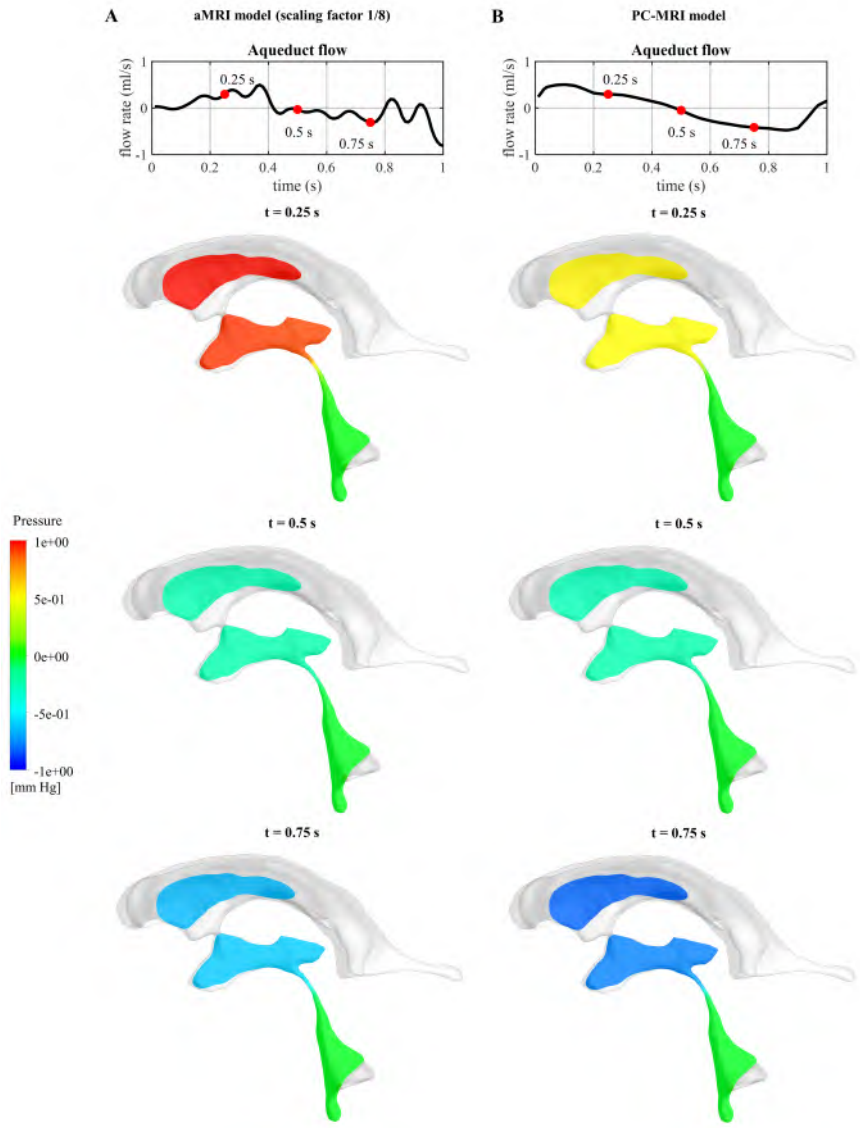


**Figure 4.9:** Visualization of aqueduct flow and pressure contours at three different time points (A) for aMRI-based deformation scaled with factor 1/8 and (B) corresponding with the PC-MRI measurements imposed at the wall of the lateral ventricles.

## 4.4 Discussion

In this study, we evaluated the feasibility of inferring brain tissue motion from aMR images and then using this motion to predict CSF behavior in the cerebral ventricles. Therefore, we developed a workflow to first extract brain tissue motion from aMRI data and then prescribe this motion to a CFD model. The resulting CSF dynamics were compared with the results obtained by imposing PC-MRI-based boundary conditions to make an estimate of the necessary scaling factor and evaluate the performance of the approach. To the best of our knowledge, this is the first study using aMRI as an input for CFD simulations of CSF and in that way imposing non-uniform boundary motion to the entire ventricular surface.

We found that each of the ventricles reduced and expanded in a pulsatile way leading to consecutively caudal and cranial flows through the cerebral aqueduct. Interestingly, we observed in figure 4.5 that the third and fourth ventricles reached their peak almost simultaneously while the peak volume of the lateral ventricles followed only 0.35 s later (35 % of the cardiac cycle). This indicates that brain tissue deforms in a heterogeneous manner, with delayed motion in deeper brain regions (e.g., region around lateral ventricles). Soellinger et al. already indicated increased damping in brain regions further away from the main pulsating arteries [163]. This suggests that imposing non-uniform ventricular boundary motion is necessary to account for realistic phase differences in pulsatile CSF flow. The delay in peak volume between the ventricles also led to a delay in instantaneous volume changes and thus a delayed displacement of CSF. A delay was also observed between the peak flows through the cerebral aqueduct and the spinal SAS measured with PC-MRI in the same subject. This delay was, however, smaller (10 % of the cardiac cycle).

The brain tissue motion was amplified, and therefore flow velocities were expected to be overestimated. An important limitation of the current study is that the spatial amplification cannot be known in advance and therefore the CFD simulations were executed after applying three different scaling factors (1/2, 1/4, and 1/8) to the originally deduced motion. We found that peak flows for scaling factor 1/8 most closely matched those of the PC-MRI measurements (see figure 4.7). Therefore, we assumed that while the PC-MRI and aMRI data were obtained at different time points (minutes apart), the conditions were sufficiently alike. Conditions during the MRI investigation were controlled (no postural changes, tracking of cardiac pulse and

breathing), but changes in heart rate and breathing pattern might have led to time-dependent differences.

Comparison of the aMRI aqueduct flow with in vivo PC-MRI measurements indicated a similar overall pattern with caudal flow in the first half of the cardiac cycle and dominantly cranial flow in the second half. Meanwhile, the flow obtained through aMRI showed important variations and a more irregular curve compared to the PC-MRI curve. These irregularities can be attributed to the fact that the flow through the aqueduct is the result of the complex motion of multiple points, which induces volume changes. The accuracy of these volume changes depends on the quality of the original aMRI sequence, the segmentation of the initial volume, and the performance of the registration algorithm. While the original volume curve was relatively smooth, the curve was not 100% noiseless and taking derivatives (e.g. relative volume changes) typically amplifies noise.

In the PC-MRI model, we assumed that aqueduct flow is driven by volume changes of the lateral ventricles by only imposing inflow in the lateral ventricles. The limited differences observed among the flow rates through the foramina of Monro, the cerebral aqueduct, and the outlet support this assumption. However, this finding needs to be confirmed in other subjects to be able to draw conclusions. For the scaling factor of 1/8, we found peak velocities in the cerebral aqueduct in the order of 0.1 m/s, which is in the same order of magnitude as the velocity found when imposing a velocity inlet based on PC-MRI measurements (PC-MRI model). While the overall velocity direction at the selected time points (see Figure 4.8) was similar, we observed local differences in recirculation in the third and fourth ventricle. These differences in recirculation might be attributed to the difference in flow curves, but also to the contribution of the third and fourth ventricles to ventricular CSF flow in the aMRI model. These results suggest that implementing physiological motion rather than inflow boundary conditions can add information regarding the detailed flow and mixing [170].

In this study, we assumed that volume changes of the brain tissues drive ventricular CSF flow, whereas other volume changes within the CSF domain might also influence the motion. However, the influence of internal volume changes is expected to be limited [31]. Finally, previous studies have reported alterations in CSF flow [171] and brain tissue motion [166] in patients with Chiari type 1 malformation compared to healthy subjects. Application of the presented workflow to multiple subjects (healthy and patients) will not only be essential to

further validate this approach and confirm the current findings but can also provide a better understanding of how physiological changes (e.g., changes in brain tissue stiffness and intracranial compliance) alter CSF dynamics.

## 4.5 Conclusion

This chapter presented the first application of non-uniform surface motion extracted from aMRI for the prediction of CSF dynamics in the cerebral ventricles. Comparison of the obtained CSF velocities with PC-MRI measurements showed a good agreement between the flow directions obtained using both techniques with dominantly caudal flow in the first half and cranial flow in the second half of the cardiac cycle. However, the aMRI peak flow rates were more subject to noise and only approached the PC-MRI flow rates in amplitude when reducing the deformations with a scaling factor. Given the current findings of phase differences and the variable contributions of boundaries to CSF flow, this study motivates the application of the presented workflow to multiple subjects to first validate the current findings and contribute to a better understanding of CSF dynamics in general.

# III

# Application of computational fluid dynamics models to study Chiari type 1 malformation

Chapters

Chapter 5

# Modeling Chiari type 1 malformation as a porous zone obstruction

Chiari type 1 malformation is characterized by an obstruction of the CSF flow at the level of the foramen magnum as previously discussed in section 1.3. This obstruction can be considered as a resistance between the intracranial and spinal compartment. An effective way to locally establish a local resistance in a fluid domain is by introducing a porous zone. Introducing a porous zone has the advantage that it requires no remeshing and the severity of the obstruction can be easily adapted by changing the resistance of the porous zone. In this chapter, we evaluate (i) whether porous zones can approximate the effects of a physical obstruction created by the herniation of the tonsils and (ii) to what level of area obstruction porous zones are expected to correspond.

This chapter is based on the supplementary material of the paper with title *"A computational fluid dynamics study to assess the impact of coughing on cerebrospinal fluid dynamics in Chiari type 1 malformation"* published in Scientific Reports [172].

## 5.1 Methods

This study is performed in cropped models of the CSF containing the skull base and the upper part of the spinal SAS (see figure 5.1).

This limited the necessary computational cost compared to a model of the full CSF circulation as presented in chapter 3. The geometry and boundary conditions were based on a newly generated and comprehensive MRI dataset and are discussed in the next sections.

### 5.1.1 Image acquisition

MR brain images of a healthy subject were acquired using a 3T MRI scanner (SIGNA Premier; General Electric Healthcare) at the medical research institute Mātai based in Gisborne, New Zealand. Ethical approval for this study was obtained through the New Zealand Health and Disability Ethics Committee (20/CEN/107). Informed consent was obtained from all subjects involved in this study. Data collection included whole-brain anatomical T1, T2, and T2 FLAIR weighted images with an isotropic resolution of 0.5 $mm^3$ and axial PC-MRI slices at the level of the second cervical vertebra (C2) and the cerebral aqueduct. An encoding velocity of 9 and 16 $cm/s$, respectively, and 0.7 $mm^2$ in-plane resolution was used for these measurements.

### 5.1.2 Geometry

The 3D geometry of the cranial and the upper spinal CSF space was extracted from the anatomical MR images using Mimics 24.0 (Materialise, Leuven, Belgium). First, thresholding and region-growing techniques were used to extract the CSF spaces, and the geometry was adjusted manually to only preserve CSF regions. Further, to allow CSF circulation around the brain, a minimal thickness of four pixels or about 2 mm was imposed for the cranial subarachnoid space (SAS). The resulting CSF space consisted of a large number of fine structures where the CSF seeps inside larger and finer sulci of the cerebellum and cerebrum. In this model, these sulci were partially removed or heavily smoothed to facilitate meshing afterward and limit computational cost. More details about the extraction of the CSF domain can be found in appendix B.

A cropped model was created from the 3D model geometry where only the CSF space around the craniocervical junction was maintained (= control). Then, cone-shaped volumes were added using Mimics 24.0 (Materialize, Leuven, Belgium) to enlarge the cerebellum and in that way occupy a larger part of the CSF space. This finally resulted in a model without obstruction (control) and four models with area stenosis of 29% (herniation 1), 70% (herniation 2), 92% (herniation 3), and 99% (herniation 4) as depicted in figure 5.1.

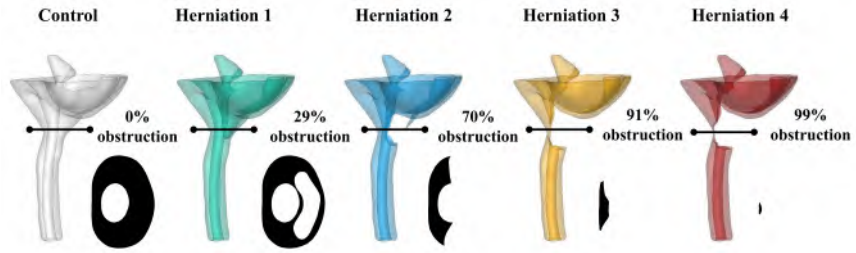


**Figure 5.1:** Control model and four different degrees of obstruction (herniation 1, 2, 3, and 4) with visualization of a cross-section (location z = -0.055 m) with corresponding % obstruction.

### 5.1.3 Meshing

The five geometries depicted in figure 5.1 were exported as STLs using 3Matic 16.0 (Materialize, Leuven, Belgium) and volume meshes were then generated in ICEM 2021 R2 (Ansys, Canonsburg, USA) with in table 5.1 the number of elements for each mesh. The meshes consisted of tetrahedral elements, which were refined up to 0.25 mm to guarantee sufficient mesh quality in the narrow CSF regions shaped by the expanding tonsillar volumes.

**Table 5.1:** Number of volumes in the meshes of the different degrees of herniation

| | Control | Herniation 1 | Herniation 2 | Herniation 3 | Herniation 4 |
|---|---|---|---|---|---|
| # cells | 920 828 | 962 061 | 917 856 | 737 880 | 919 523 |

### 5.1.4 Model setup and boundary conditions

CFD simulations were set up in finite volume solver Fluent 2021 R2 (Ansys, Canonsburg, USA) with fluid properties (density 998.2 $kg/m^3$ and dynamic viscosity 0.001003 $kg/m/s$) and assuming laminar flow. The transient simulations were run using a PISO scheme and a finite volume method with 2nd order spatial discretization for momentum, standard for pressure and 2nd order implicit temporal discretization. Under-relaxation factors were set to 0.5 for both pressure and momentum. Figure 5.2 depicts the locations of the boundary conditions with zero pressure imposed at the caudal end of the SAS and inlet velocities (in m/s) at the top of the fourth ventricle $v_{v4}$ with surface area $A_{v4}$ and at the top cranial SAS $v_{csas}$ with surface area $A_{csas}$.

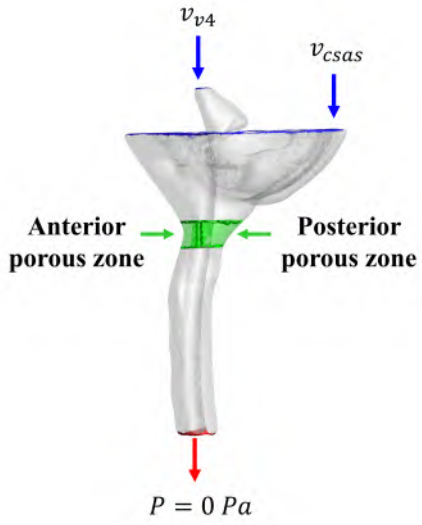


**Figure 5.2:** Overview of inlet (blue) and outlet (red) boundary conditions for the base model with the anterior and posterior porous zone (green) created in the control model.

The transient inlet velocity profile was calculated from the smoothed in vivo flow measurements obtained at the level of the cerebral aqueduct $Q_{aq}$ and in the spinal SAS $Q_{sas}$.

$$v_{csas} = \frac{Q_{sas} - Q_{aq}}{A_{csas}} \tag{5.1}$$

$$v_{v4} = \frac{Q_{aq}}{A_{v4}} \tag{5.2}$$

### 5.1.5 Introducing the porous zone approach

The anterior and posterior porous zones were created in ICEM 2021 R2 (Ansys, Canonsburg, USA) after meshing and extended along the spinal canal over a length of 1 cm (between z = -0.050 to -0.060 m). At an axial plane with z-coordinate -0.055 m, the posterior zone filled 75 % of the spinal canal, whereas the anterior zone entailed the remaining 25 %. Neglecting inertial effects, the relation between pressure difference (dP) and volumetric flow (Q) over a porous zone with cross-sectional area (A) and length (d) is given by

$$dP = R_{viscous} \cdot \mu \cdot d \cdot \frac{Q}{A} \tag{5.3}$$

where $R_{viscous}$ $(1/m^2)$ is the viscous resistance and $\mu$ $(kg/m/s)$ the dynamic viscosity. Three different degrees of obstruction (OBS-1, OBS-2, and OBS-3) were realized by adapting the viscous resistance of the anterior porous zone. The viscous resistance of the posterior zone was based on the permeability values used by Bertram et al. [71], who modeled the spinal cord as a poroelastic medium and suggested that the permeability $a$ of 1E-14 $m^2$ was most realistic. The viscous resistance can be described as $1/a$, indicating that a value of 1E14 $1/m^2$ would be adequate for neurological tissue and thus the obstruction. To make the final selection for the viscous resistance values of the anterior porous zone (OBS-2 and OBS-3), we evaluated the pressure in the fourth ventricle for viscous resistances varying from 1E6 until 1E10 $1/m^2$. The results corresponding to the selected porous zone obstructions (OBS-1, OBS-2, and OBS-3) and the physical obstructions were evaluated to verify whether porous zones adequately capture the impact of herniated tonsils on CSF flow.

## 5.2 Results

### 5.2.1 Selecting the viscous resistance of the anterior zone

We found that a viscous resistance of 1E8 $1/m^2$ displayed the first significant increase in pressure compared to OBS-1 as depicted in figure 5.3, and was therefore selected as OBS-2. Finally, a viscous resistance of 1E10 $1/m^2$ induced as the lowest value a peak pressure in the fourth ventricle larger than the mean ICP of 10 mmHg considered in this work, and therefore was judged suitable as the most severe case (OBS-3).

### 5.2.2 Impact of obstruction on pressure difference

Figure 5.4A-C shows the pressure difference between a cross-section of the fourth ventricle and the spinal SAS (below the herniation) for both physiologically inspired herniations and the porous obstructions. Without obstruction (control), a maximal value of 0.08 mmHg is reached at time 0.91 s. Introducing a physiological herniation amplifies this pressure difference up to 0.11, 0.18, 0.44, and 22.25 mmHg for herniation 1, 2, 3, and 4, respectively, with a delay in the peak for herniation 4 with 0.06 s. OBS-1 resulted in a maximal pressure difference of 0.16 mmHg and similar to the herniation 1, 2, 3 no delay in peak pressure difference occurred. This contrasts with OBS-2 and OBS-3 where a peak of 0.40 mmHg and 33.51 mmHg appears at time points 0.94 and 0.97 s, respectively. These peak pressure differences

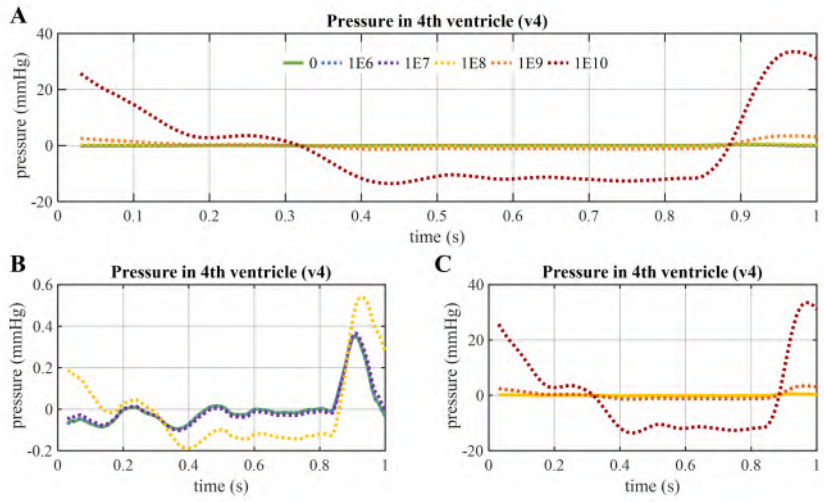


**Figure 5.3:** Pressure in the fourth ventricle with a viscous resistance of the posterior zone of 1E14 $1/m^2$ and a viscous resistance of the anterior zone ranging from (A) 0 to 1E10 $1/m^2$, (B) 0 to 1E8 $1/m^2$ and (C) 1E8 to 1E10 $1/m^2$.

**Table 5.2:** Overview of the peak pressure differences and corresponding % increases for the control, the physical obstructions (herniation 1, 2, 3 and 4) and the porous zone obstructions (OBS-1, OBS-2 and OBS-3).

| | | Herniation | | | | OBS | | |
|---|---|---|---|---|---|---|---|---|
| | control | 1 | 2 | 3 | 4 | 1 | 2 | 3 |
| dP (mmHg) | 0.08 | 0.11 | 0.18 | 0.44 | 22.25 | 0.16 | 0.40 | 33.51 |
| Increase (%) | - | 27 | 114 | 419 | 26381 | 90 | 381 | 39783 |

(dP) and the corresponding increases (in %) in peak pressure difference compared to the control are summarized in table 5.2.

Visualization of pressure as a function of volumetric outflow in figure 5.4D shows a close match between OBS-1 and herniation 2. Despite the difference of only 9 % between the peak values for OBS-2 and herniation 3, the pressure-flow curves are very different with a more linear relation for OBS-2 compared to herniation 3 (figure 5.4E). Finally, in figure 5.4F, we observe an almost linear relationship between pressure difference and flow for OBS-3, whereas a nonlinear relationship is found for herniation 4. It should be noted that around peak flow the pressure residual (convergence criterion) did not drop below 1E-3 for herniation 4 (fluctuated around 1E-2). This can be the result of the important reduction and expansion of the cross-section leading to a significant local disturbance of the CSF flow.

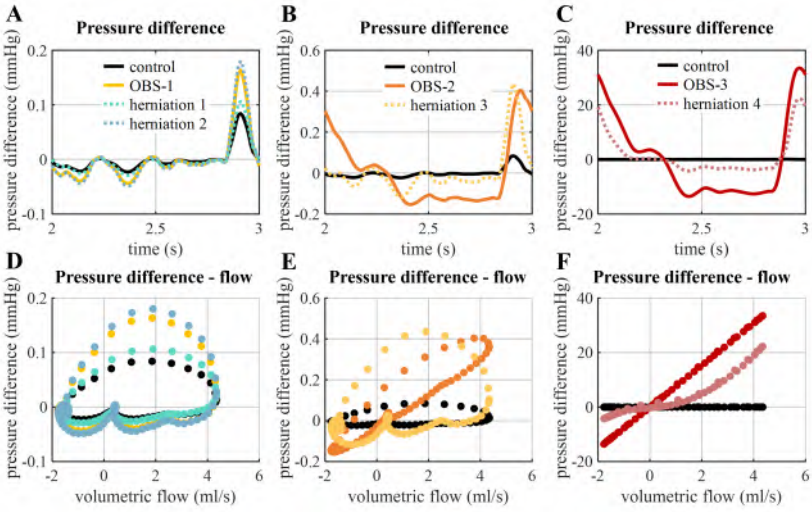


**Figure 5.4:** Pressure difference between fourth ventricle (v4) and spinal SAS in function of time and volumetric flow for (A, D) healthy control, OBS-1, herniation 1, and herniation 2, (B, E) for healthy control, OBS-2 and herniation 3, and for (C, F) healthy control, OBS-3, and herniation 4.

### 5.2.3 Impact of obstruction on flow

The cropped model can also be used to assess the impact of an obstruction on local flow. In figure 5.5 velocity streamlines are visualized for the case without obstruction (control), herniation 2, and OBS-1 using a porous zone approach for four different time points, with peak flows at 0.44 s and 0.97 s. It can be observed that some recirculation happened at time 0.25 s below the obstruction which was more distinct in the OBS-1 compared to herniation 2.

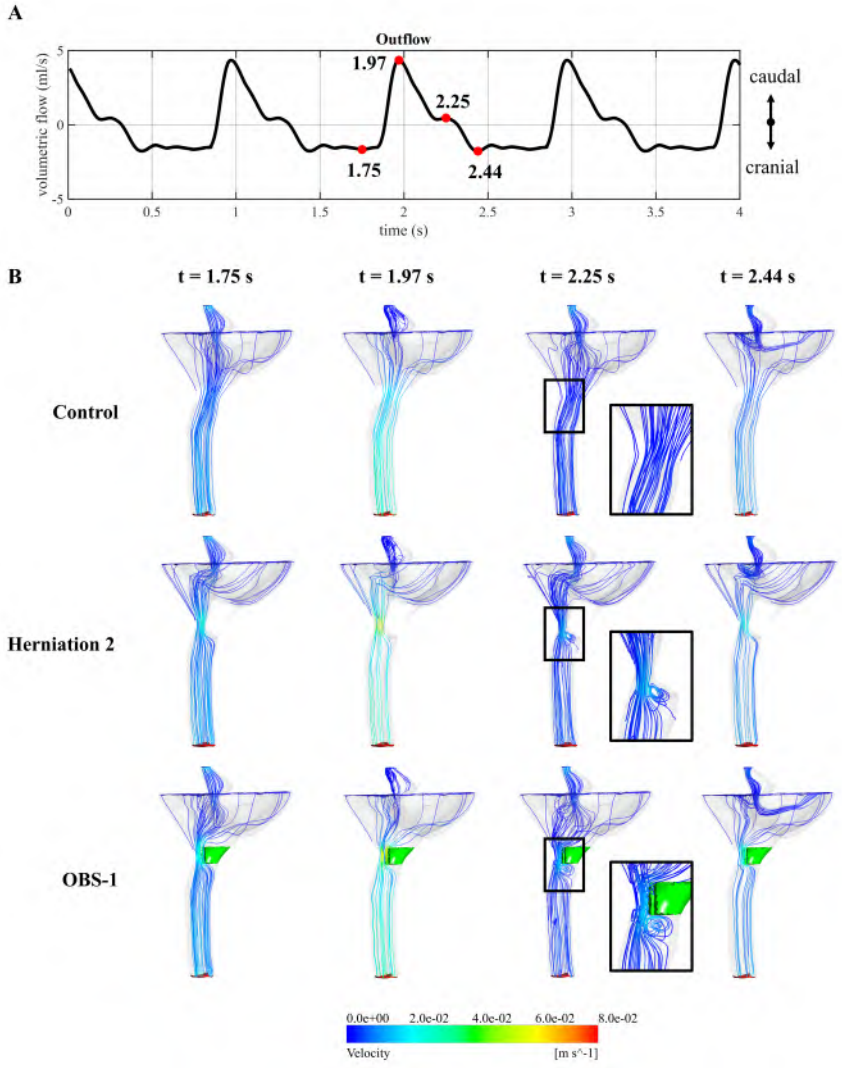


**Figure 5.5:** (A) Volumetric flow rate through the outlet and (B) velocity streamlines at four different time points along the cardiac cycle for the healthy control, herniation 2, and OBS-1.

## 5.3 Discussion

This study was performed in a cropped model, to compare the effects of a porous zone against those of four physical obstructions (herniation 1, 2, 3 and 4) with a shape based on the herniated tonsils as present in Chiari type 1 malformation. The pressure difference between the fourth ventricle and the spinal SAS deviated maximally 10 % between a 70 % area obstruction (herniation 2) and OBS-1 and corresponding pressure-flow curves matched well. For OBS-2 and OBS-3, the peak pressure differences were in the same order as those obtained for an area obstruction of 91 % (herniation 3) and 99 % (herniation 4), respectively, but the pressure-flow distributions were significantly different, with a clear linear relation for the porous obstructions (OBS-2 and OBS-3), which was not observed in any of the physical obstructions. These findings imply that OBS-1 is a valid choice for investigating pressure differences resulting from a physical obstruction occupying 70 % of the spinal canal. Meanwhile, OBS-2 and OBS-3 peak pressure differences are closest to an area obstruction of 91 and 99%, respectively; the latter suggests that OBS-3 corresponds to an almost complete blockage of the spinal canal. These results also show that the pressure difference and thus the impact of the obstruction increases with the degree of area obstruction, implying that area obstruction relates to disease severity. Previous CFD studies have reported an increase in pressure difference between healthy controls and patients with Chiari type 1 malformation with increases varying between 26 and 324 % (see table 5.3) which is in the range of the values obtained for herniation 1 and 2, and OBS-1. Only percentage increases are compared as the exact distances over which those pressure differences were calculated differ among studies.

Interestingly, recirculation caudally of the obstruction is more profound in OBS-1 compared to the physical 70% area obstruction (herniation 2) despite their close match for the pressure differences (see figure 5.5). This indicates that the shape of the obstruction has an important effect on local flow dynamics. Increased and bidirectional flows have been previously reported in a 4D PC-MRI study comparing healthy subjects and patients with Chiari malformation [57, 58]. A maximal velocity of 0.08 m/s was observed for OBS-1 at the level of obstruction, which is in range of simulation results of previous studies reporting peak values between 0.023 and 0.44 m/s [131, 132, 134, 173, 174] as depicted in table 5.3.

**Table 5.3:** Overview of peak velocities in Chiari type 1 malformation (CMI) and the increases in peak pressure differences across the partial obstruction between Chiari type 1 malformation (CMI) and healthy controls (dP) derived from CFD studies

| | Peak velocities CMI (m/s) | Increase in dP (%) (CMI vs control) |
|---|---|---|
| OBS-1 | 0.07 | 95 |
| Yiallourou et al., 2012 [132] | 0.023 - 0.035 (caudal) | - |
| Rutkowska et al., 2012 [131] | 0.075 - 0.12 | - |
| Clarke et al., 2013 [133] | - | 117 |
| Martin et al., 2013 [136] | 0.068 and 0.086 | 151 and 289 |
| Stoverud et al., 2016 [134] | 0.123 and 0.439 | 32 and 150 |
| Jain et al., 2017 [173] | 0.15 and 0.38 | -12 and 324 |
| Gholampour et al., 2020 [174] | 0.042 - 0.063 (caudal) | 26 |

CHAPTER 6

# Analysis of the effects of coughing on cerebrospinal fluid dynamics in Chiari type 1 malformation

The objective of this study is to investigate the impact of an obstruction in the spinal canal, as present in patients with Chiari type 1 malformation, on CSF flow and pressure both under normal arterial pulsations and under the action of coughing. Chiari type 1 malformation has also been found to induce a reduction of compliance in the spinal compartment [70]. We, therefore, (i) optimized and tuned our CFD modeling framework presented in chapter 3, to a newly generated and comprehensive MRI dataset, (ii) implemented sudden volume changes in the spinal compartment to emulate coughing, and assessed the impact of (iii) various degrees of obstruction in the spinal canal and (iv) different values of spinal compliance during normal pulsatile CSF dynamics and under the action of coughing.

This chapter is based on the paper with title *"A computational fluid dynamics study to assess the impact of coughing on cerebrospinal fluid dynamics in Chiari type 1 malformation"* published in Scientific Reports [172] with the inclusion of an additional study on the impact of compliance reduction.

## 6.1 Methods

In this section, the setup of the 3D model and the implementation of boundary conditions are presented.

### 6.1.1 Image acquisition

MR brain images of a healthy subject were acquired using a 3T MRI scanner (SIGNA Premier; General Electric Healthcare) at the medical research institute M$\bar{a}$tai based in Gisborne, New Zealand. Ethical approval for this study was obtained through the New Zealand Health and Disability Ethics Committee (20/CEN/107). Informed consent was obtained from all subjects involved in this study. All methods were performed in accordance with the relevant guidelines and regulations. Data collection included whole-brain anatomical T1, T2, and T2 FLAIR weighted images with an isotropic resolution of 0.5 $mm^3$ and axial PC-MRI slices at the level of the second cervical vertebra (C2) and the cerebral aqueduct. An encoding velocity of 9 and 16 cm/s, respectively, and 0.7 $mm^2$ in-plane resolution was used for these measurements.

### 6.1.2 Segmenting and meshing the 3D geometry

#### *6.1.2.1 Model Segmentation*

The 3D geometry of the cranial and the upper spinal CSF space was extracted from the anatomical MR images using Mimics 24.0 (Materialise, Leuven, Belgium). First, thresholding and region-growing techniques were used to extract the CSF spaces, and the geometry was adjusted manually to only preserve CSF regions. Further, to allow CSF circulation around the brain, a minimal thickness of four pixels or about 2 mm was imposed to the cranial subarachnoid space (SAS). The resulting CSF space consisted of a large number of fine structures where the CSF seeps inside larger and finer sulci of the cerebellum and cerebrum. In this model, these sulci were partially removed or heavily smoothed to facilitate meshing afterward and limit computational cost. More details about the extraction of the CSF domain can be found in appendix B. All the resulting geometries were checked in 3-Matic 16.0 (Materialise, Leuven, Belgium) for possible meshing errors, and boundary surfaces were selected. The geometry used in this study was the same as the geometry, which was cropped, in chapter 5.

#### *6.1.2.2 Meshing the model*

An unstructured mesh was generated using ICEM 2021 R2 (Ansys, Canonsburg, USA). The mesh was composed of tetrahedral elements

with three prism layers at the boundaries and was refined in the aqueduct region to ensure that the parabolic laminar profile was accurately captured in this thin region (1-2 mm in diameter). A mesh sensitivity study was conducted with four different meshes (with a number of volumes ranging from 0.41 to 4.29 million), whereby we evaluated two variables that are critical in this study: the pressure difference between the lateral ventricles (lv) and spinal SAS, and the maximal velocity in the aqueduct. The mesh with 1.14 million elements, corresponding to a difference of less than 3 % for these two variables compared to the finest mesh, was finally selected. More details on the mesh parameters and mesh sensitivity study can be found in appendix C.

### 6.1.3 Boundary conditions

The model was set up using the numerical finite volume software Fluent 2021 R2 (Ansys, Canonsburg, USA) with boundary conditions based on physiological processes as previously presented in chapter 3. Figure 6.1A depicts the locations of the inlet and outlet boundary conditions in blue and red, respectively.

#### *6.1.3.1 Production of CSF*

A constant velocity was imposed on a surface of the lateral ventricles to simulate CSF production, which has been estimated to occur at a rate of 0.4 ml/min (576 ml/day) in the choroid plexuses in the lateral and third ventricles (see 3), leading to an imposed velocity $v_{production}$ in m/s.

$$v_{production} = 1.14E - 5m/s \tag{6.1}$$

#### *6.1.3.2 Arterial pulsations*

The volume changes of arteries along the cardiac cycle were implemented as a source term (in $kg/m^3s$) in the CSF region anterior to the brainstem and as a velocity inlet (m/s) in the lateral ventricles. This was to emulate the pulsatile CSF motion assuming two pathways: CSF flow originating from volume changes of large arteries (e.g. basilar artery) and ventricular flow driven by brain tissue motion, which has been observed mainly in the mid-brain region [165]. In contrast to our previous study presented in chapter 3, in which simplified sinusoidal signals were used, the inputs in this study were based on in vivo measurements of the CSF flow through the cerebral aqueduct and the spinal SAS (figure 6.1B), which were extracted

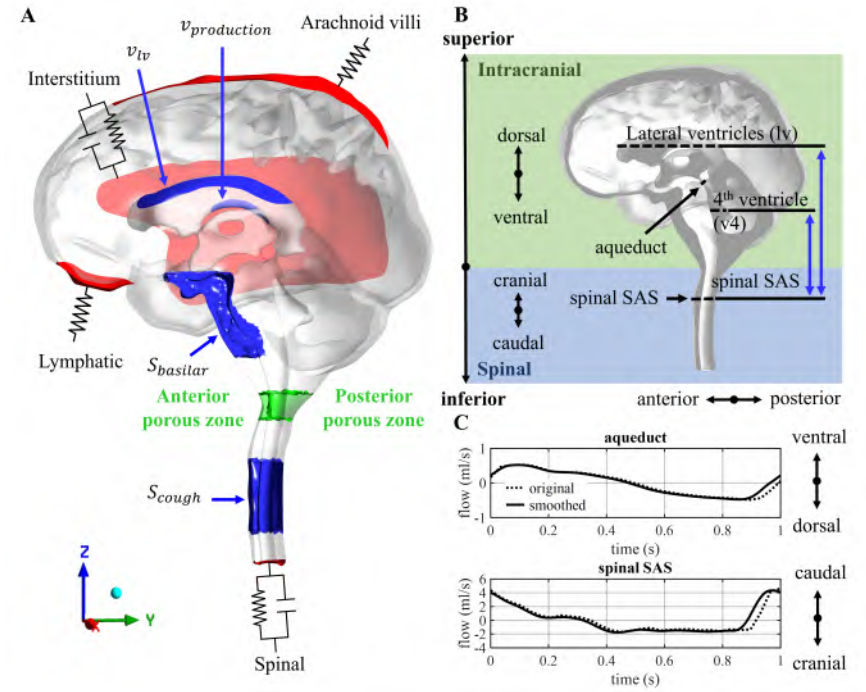


**Figure 6.1:** (A) Model geometry with the inlet (blue) and outlet (red) boundary conditions and the anterior and posterior porous zones (green). (B) Section of the 3D model showing the intracranial (green) and upper spinal (blue) compartment, anatomical directions, and cross-sectional planes where flows in (c) and spatial pressure differences are calculated. (C) Original and smoothed (as used in this model) PC-MRI measurements of volumetric flow through the cross-sections of the cerebral aqueduct and spinal SAS with caudal/ventral flow being positive.

.

from PC-MRI measurements using Circle CVI42 (Circle Cardiovascular Imaging, Calgary, Canada). The original flow data consisted of 30 time points and was first scaled to one second per cardiac beat and then interpolated to obtain 100 time points using a MATLAB R2023a (MathWorks, Natick, USA) interpolation function (Piecewise Cubic Hermite Interpolating Polynomial (PCHIP)). Finally, the data was smoothed using a moving average filter with a width of 7. Here, we assumed that the flow is equal at times 0 s and 1 s and that the CSF production is too small to be measured by PC-MRI, and thus the net flow per cardiac cycle should be zero. Therefore, for both measurements, the mean flow was subtracted from the value of every time point resulting in the flow through the cerebral aqueduct $Q_{aq}(t)$ and the spinal SAS at level C2 $Q_{sas}(t)$. In figure 6.1C both

the original and smoothed profiles are presented with positive being flow in the caudal/ventral direction and negative being flow in the cranial/dorsal direction.

The inlet boundary conditions were then defined. Following the conservation of mass, the instantaneous inflow at the lateral ventricles $Q_{lv}(t)$ should be equal to the flow through the cerebral aqueduct $Q_{aq}(t)$. Consequently, the velocity $v_{lv}(t)$ (m/s) imposed at the upper wall of the lateral ventricles (see figure 6.1A) is described as:

$$v_{lv}(t) = \frac{Q_{aq}(t)}{A_{lv}} \tag{6.2}$$

where $A_{lv}$ $(m^2)$ is the surface area of the upper part of the lateral ventricles (see figure 6.1A). Further, the flow measured in the spinal SAS $Q_{sas}(t)$ can be described in function of the CSF volume changes in the region of the basilar artery, at the anterior side of the brain stem $Q_{basilar}(t)$ and the flow through the aqueduct $Q_{aq}(t)$, with 2/3 of the flow going to the spinal compartment (result of the chosen distribution of compliance, with 1/3 and 2/3 in the intracranial and spinal compartments, respectively).

$$Q_{sas}(t) = \frac{2}{3}(Q_{basilar}(t) + Q_{aq}(t)) \tag{6.3}$$

Consequently, the source term $S_{basilar}(t)$ $(kg/m^3 s)$ imposed in the region anterior to the brainstem can be described in the following way:

$$S_{basilar}(t) = \frac{\frac{3}{2}Q_{sas}(t) - Q_{aq}(t)}{V_{basilar}} \cdot \rho \tag{6.4}$$

where $V_{basilar}$ $(m^3)$ is the volume of the CSF region posterior to the brainstem, and $\rho$ the density of CSF (998.2 $kg/m^3$).

#### *6.1.3.3 Outlet boundary conditions*

The model has four different outlets accounting for absorption via the arachnoid villi, spinal pathways, interstitium and lymphatic system and buffering in the intracranial and spinal compartments as depicted schematically in figure 6.2.

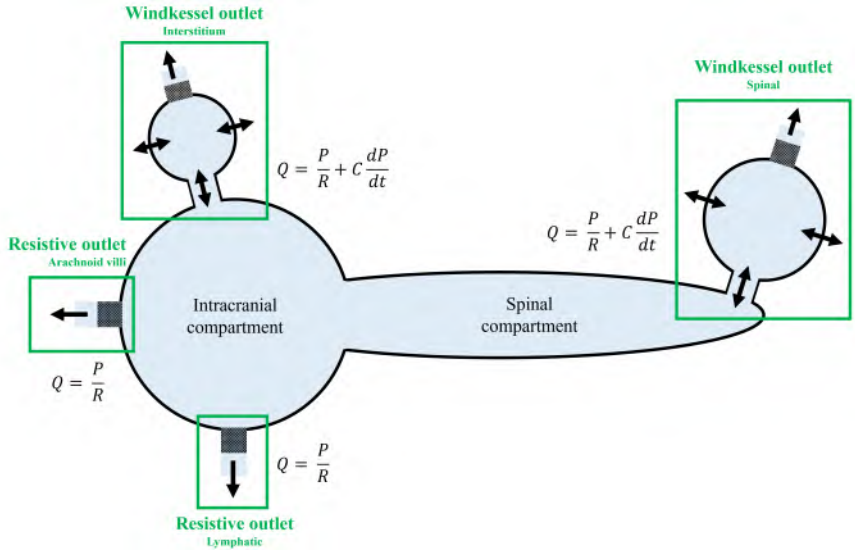


**Figure 6.2:** Schematic of the intracranial and spinal compartments with the four different outlets represented as physical components. The windkessel outlets include an absorption path and buffering compartment whereas the resistive outlets have only an absorption path.

At the arachnoid villi and lymphatic outlet, pure resistive boundary conditions were considered to model CSF absorption following equation 6.5.

$$Q_i = \frac{P_i - P_{ext}}{R_i} = \frac{P_i}{R_i} \quad P_{ext} = 0 \quad mmHg \tag{6.5}$$

For each outlet $i$, $Q_i$ is the outflow, $P_i$ the pressure and $R_i$ the corresponding resistance. $P_{ext}$ is the external pressure and was considered zero. Meanwhile, 2-element windkessel models were imposed at the interstitium and spinal outlet to model CSF absorption and buffering following equation 6.6 with $C_i$ the compliance and t the time.

$$Q_i = \frac{P_i - P_{ext}}{R_i} + C_i\frac{d(P_i - P_{ext})}{dt} = \frac{P_i}{R_i} + C_i\frac{dP_i}{dt} \quad P_{ext} = 0\, mmHg \tag{6.6}$$

The differential equation 6.6 was discretized in time by considering timestep $\Delta t = t_n - t_{n-1}$. This allowed us to express the pressure at time n ( $P_{i,n}$ ) in function of the outflow ($Q_{i,n}$) and the pressure at the previous timestep ($P_{i,n-1}$) as depicted in equation 6.7.

$$P_{i,n} = \frac{Q_{i,n} \cdot R_i + P_{i,n-1} \cdot \frac{C_i \cdot R_i}{\Delta t}}{1 + \frac{C_i \cdot R_i}{\Delta t}} \tag{6.7}$$

We first calculated the compliance and resistance parameters using a 0D windkessel model presented in chapter 3. For this study, we implemented this 0D windkessel model in MATLAB R2023a (MathWorks, Natick, USA) and considered the same mean CSF pressure $P_{mean}$ of 10 mmHg, but a lower peak-to-peak pressure difference $dP_{min-max}$ of 4 mmHg. The mean CSF pressure was selected within the reported physiological range of 7 to 15 mmHg [148] and the peak-to-peak pressure difference was based on historical measurements from Ghent University Hospital. The peak-to-peak pressure difference was allowed to maximally deviate 0.01 mmHg compared to the targeted value for calculation of compliance. Resistance values for the interstitium, spinal, lymphatic, and arachnoid villi outlets were 7500, 7500, 5000, and 5000 mmHg.s/ml, respectively. Compliance values for the interstitium and spinal outlet were 0.0988 and 0.1977 ml/mmHg, respectively.

The resistor and windkessel boundary conditions were implemented using a coupling algorithm, which was monitored by a combination of UDFs and journal files, and was previously discussed in chapter 3. In this algorithm, a strong coupling between different outlets was reached by dividing each timestep into coupling iterations and using a Jacobian, calculated by introducing a pressure perturbation at each outlet in the first four coupling iterations. In contrast to chapter 3 where only one value for the pressure perturbation was used for each simulation, in this study, the pressure perturbation was varied between 1 to 1E-2 Pa to ensure a decreasing value of the flow residual over the coupling iterations.

#### *6.1.3.4 Emulating coughing*

Coughing leads to intrathoracic pressure changes and compression and expansion of the veins in the spinal compartment [42], and was implemented into the CFD model as a source term $S_{cough}(t)$ $(kg/m^3s)$, which was described by a Gaussian function leading to a subsequent steep positive (subscript p) and negative inflow (subscript n).

$$S_{cough}(t) = \frac{SA}{\sigma \cdot \sqrt{2\pi}} \cdot \Big[ \exp\Big( -\frac{1}{2}\frac{(t-\mu_p)^2}{\sigma^2} \Big) - \exp\Big( -\frac{1}{2}\frac{{\mu_p}^2}{\sigma^2} \Big) - \exp\Big( -\frac{1}{2}\frac{(t-\mu_n)^2}{\sigma^2} \Big) + \exp\Big( -\frac{1}{2}\frac{{\mu_n}^2}{\sigma^2} \Big) \Big] \quad (6.8)$$

Here, the standard deviation of the peak $\sigma$ was selected to be 0.1 s and the mean values of respectively the positive $\mu_p$ and negative peak $\mu_n$ were set to 1.88 s and 2.13 s. The source term was implemented in the spinal compartment (see figure 6.1A) to mimic the volume changes of the dense network of veins lining the spinal canal (venous plexus) during coughing. To determine the scaling factor SA, we based ourselves on Williams et al. who reported that coughing causes a sharp peak in ICP of about 35 mmHg above the mean value [49]. Therefore, factor SA ($kg/m^3s$) was estimated using the 0D windkessel model by imposing the sum of $S_{cough}(t)$ and the constant production rate $Q_{production}$ as transient input in the 0D model. The factor leading to an increase in CSF pressure of minimally 35 mmHg was selected, which was 2356.30 $kg/m^3$ s and corresponded to a peak volumetric inflow into the model of 50.46 ml/s.

### 6.1.4 Emulating different degrees of obstruction

The final objective of this work is to evaluate the impact of a flow obstruction at the level of the foramen magnum as present in Chiari type 1 malformation on CSF dynamics. We chose to model the obstruction as a porous disc composed of an anterior zone and a posterior zone depicted in green in figure 6.1A, inspired by Cheng et al. [175] modeling a spinal canal arachnoiditis. This approach had as a major benefit that all computations could be done on identical geometries and meshes thereby avoiding that differences in the boundary zones or numerical meshes introduced differences between simulations which may interfere with the effects of the obstruction. The validity of the approach for the computation of cranio-spinal pressure differences was verified by comparison of the porous zone approach with the conventional stenosed geometry methodology in a cropped model. Results of this comparison study are provided in chapter 5. The anterior and posterior porous zones were created in ICEM 2021 R2 (Ansys, Canonsburg, USA) after meshing in the same way as discussed in chapter 5.

Three different degrees of obstruction were evaluated, starting with a model without obstruction (control), then including a posterior obstruction (OBS-1), and finally adding a mild and severe anterior obstruction (OBS-2 and OBS-3). The values of viscous resistance for the posterior and anterior zones are selected based on the permeability of the spinal cord [71] and the effect of viscous resistance on pressure, respectively. More details on the selection procedure are provided in chapter 5. An overview of these different cases is provided in Table 6.1.

**Table 6.1:** Overview of viscous resistances $1/m^2$

| | Viscous resistance anterior zone $(1/m^2)$ | Viscous resistance posterior zone $(1/m^2)$ |
|---|---|---|
| Control | 0 | 0 |
| Posterior (OBS-1) | 0 | 1E14 |
| Posterior-Anterior mild (OBS-2) | 1E8 | 1E14 |
| Posterior-Anterior severe (OBS-3) | 1E10 | 1E14 |

### 6.1.5 Reducing spinal compliance

We evaluated the impact of a compliance reduction by adapting the compliance value of the spinal outlet. Heiss et al. [70] reported a mean cervical compliance value of 6 ml CSF/mmHg for healthy subjects, and 3.2 and 4.1 ml CSF/mmHg for patients with Chiari type 1 malformation pre and post-treatment, respectively. Hence, the spinal compliance increased after treatment of the patients with Chiari type 1 malformation. These values correspond to a decrease in compliance of 47 and 32 % compared to healthy subjects. We apply these relative changes to the calculated spinal compliance of 0.1977 ml/mmHg. An overview of adapted compliance values is listed in table 6.2.

**Table 6.2:** Overview of the applied values for spinal compliance with the original value (baseline), and the reduced values for patients with Chiari type 1 malformation before treatment (CMI pre-treatment), and after treatment (CMI post-treatment) calculated based on Heiss et al. [70].

| | Spinal compliance (ml/mmHg) |
|---|---|
| Baseline | 0.1977 |
| CMI pre-treatment | 0.1054 |
| CMI post-treatment | 0.1351 |

### 6.1.6 Numerical settings

CSF was modeled as an incompressible Newtonian fluid with properties the same as water (density 998.2 $kg/m^3$ and dynamic viscosity of 0.001003 $kg/m/s$). The effects of gravity were not taken into account. The Navier-Stokes equations were solved using the numerical finite volume solver Fluent 2021 R2 (Ansys, Canonsburg, USA).

As mentioned previously, a semi-implicit approach was used to update windkessel boundary conditions, where each timestep was divided into coupling iterations; the underlying algorithm is described in more detail in chapter 3. Furthermore, the transient simulations were run using a PISO scheme, a second-order temporal discretization and standard for pressure and second-order for momentum spatial discretization. The relaxation factors for momentum and pressure varied between 0.5 and 0.15 to stabilize the convergence. An initial timestep size of 0.01 s was imposed. This time-step was reduced during the cough to 0.001 s to improve the convergence of the simulation results. All simulations were run for four cardiac cycles. The convergence criterion for residuals in the solver iterations was set to 1E-5 for continuity and 1E-9 for the three velocity directions. For the residuals of the coupling iterations with the windkessel models, a dynamic flow criterium with a value of three orders of magnitude lower (1E-3) than the lymphatic volumetric outflow was set (on average 1E-9 $m^3/s$). Less than 0.5 % of coupling iterations did not meet the set convergence criterion for all simulations. The central computing infrastructure of Ghent University (HPC) was used for the simulations using up to 128 processor cores. The simulation of 4 seconds (1300 timesteps) took between 31 to 37 hours to run for the different cases.

## 6.2 Results

The results are organized into three sections: (i) comparison of simulation results for a healthy control with in vivo measurements and targeted pressures, and evaluation of the impact of three different degrees of obstruction (ii) during pulsatile CSF dynamics, and (iii) during coughing.

### 6.2.1 Evaluating pulsatile CSF dynamics in a healthy control

The simulation results for the control are compared with the input flow data in figure 6.3A. A maximal deviation of 1 % was found

between simulated and targeted flow in the cerebral aqueduct, while a difference of 9.9 % appears during peak flow through the spinal SAS (time point depicted as d in figure 6.3A). Figure 6.3B-G show that along the cardiac cycle maximal velocities occur at the cerebral aqueduct. In the control, the velocity averaged at one cross-section of the cerebral aqueduct, with location depicted in figure 6.1B, reaches a maximal value of 0.13 m/s. Given that this cross-section has a diameter of 2 mm, a maximal Reynolds number of 259 is reached, indicating a laminar flow.

Windkessel parameters were tuned using a 0D model targeting a mean pressure of 10 mmHg and a peak-to-peak pressure difference of 4 mmHg. A mean pressure of 10.62 mmHg was obtained in the 0D model which gradually reduced over time toward the targeted pressure of 10 mmHg. The 3D model realizes a mean pressure of 10.42 mmHg and a pulsatile pressure difference of 3.93 mmHg as depicted in figure 6.3H, which correspond to differences of respectively 4.2 and 1.8 % compared to the target pressure values. The large reduction in diameter between the third and fourth ventricles is also reflected in the spatial pressure differences (see figure 6.3I) where a maximal pressure difference of 0.10 mmHg is reached between the fourth ventricle and a cross-sectional plane of the spinal SAS compared to a pressure difference of 0.31 mmHg between the lateral ventricles and the same plane in the spinal SAS.

### 6.2.2 Impact of an obstruction on pulsatile CSF dynamics

To evaluate the impact of an obstruction, the simulation results of the healthy control are compared with those corresponding to three degrees of obstruction introduced in the control as porous zones (see overview in 6.1 1).

#### *6.2.2.1 CSF flow*

Figure 6.4A shows how the pulsatile flow through the spinal SAS (location in figure 6.1B) undergoes minor changes for OBS-1 and OBS-2, with a 10 % increase of the peak flow in OBS-1 and a delay of the peak flow with 0.01 s in OBS-2. For these milder obstructions and the control, the flow rates through the arachnoid villi and lymphatic outlets reflect the pressure profile, whereas the flow rates at the spinal and interstitium outlet follow the inflow profiles, with the amplitudes depending on the contribution of these outlets to the total compliance (see figure 6.4B-E). This contrasts with the visible reduction of the flow through the spinal SAS in OBS-3 (figure 6.4A), which is compensated for by the intracranial outlets with an increase in the peak

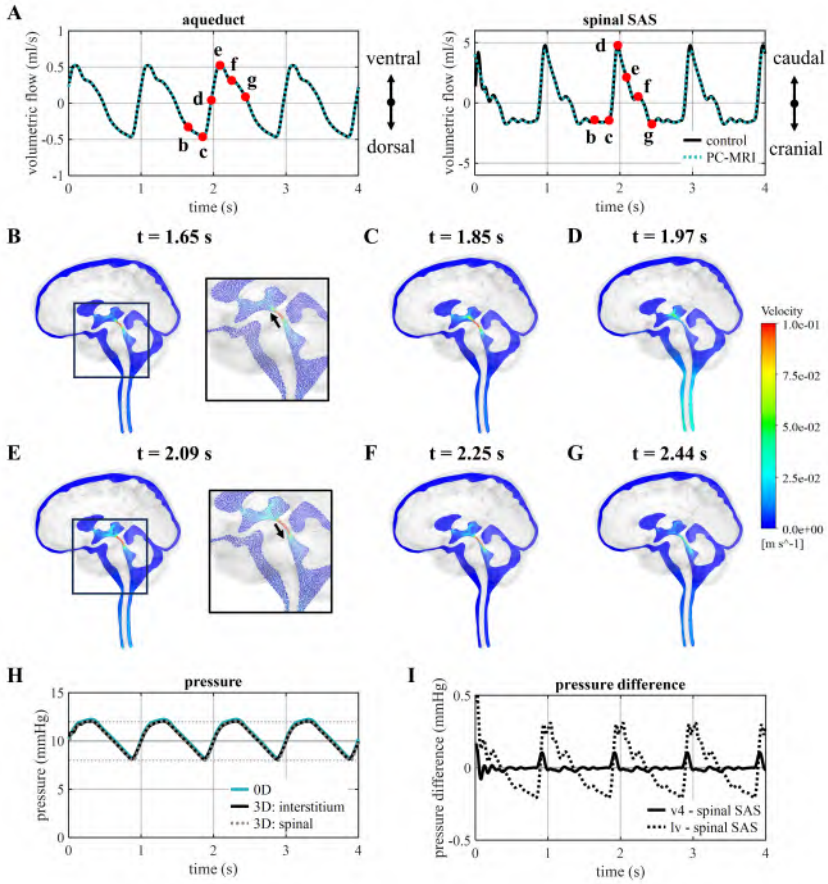


**Figure 6.3:** Simulation results for control case. (A) Smoothed PC-MRI flow measurements compared to simulated flow through the cross-sections of the cerebral aqueduct and the spinal SAS. (B-G) Selection of velocity contours at six different time points to visualize velocity distribution and with details of the velocity vectors in (B) and (E). (H) Pressure at the spinal and interstitium outlet presented together with the pressure in the 0D model (0D) with horizontal lines depicting the targeted mean pressure (10 mmHg) and amplitude (2 mmHg). (I) Plot of pressure differences between the fourth ventricle (v4) and the lateral ventricle (lv), and the spinal SAS.

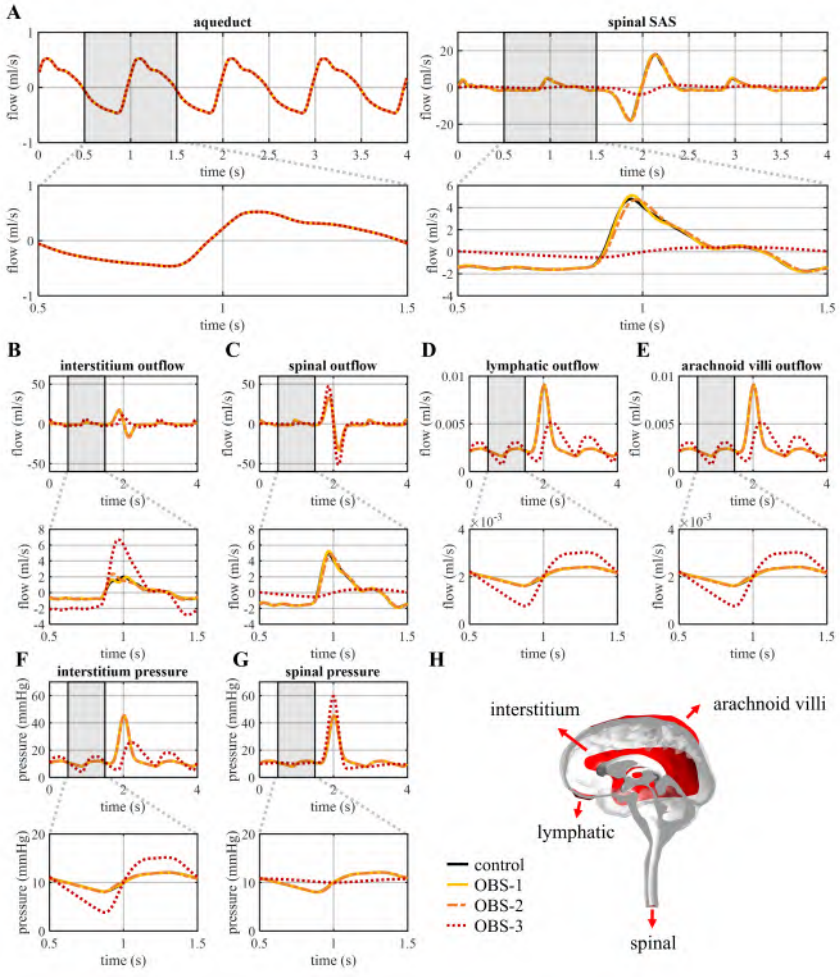


**Figure 6.4:** Volumetric flow rate through (A) a cross-sectional plane of the cerebral aqueduct and spinal SAS, and at the (B) interstitium, (C) spinal, (D) lymphatic, and (E) arachnoid villi outlet for four cardiac cycles and zoomed in for one cardiac cycle between 0.5 and 1.5 s. Pressure at the (F) interstitium and (G) spinal outlet for four cardiac cycles and zoomed in for one cardiac cycle between 0.5 and 1.5 s. (H) Locations of the four different outlets.

flow through the interstitium outlet (+240%) and the flow amplitude (peak-to-peak flow difference divided by 2) through the arachnoid villi and lymphatic outlet (+189%) (figure 6.4C-E).

#### *6.2.2.2 CSF pressure and pressure differences*

The amplitude of the pressure pulsations is equal to 1.96 mmHg at the interstitium and 2.04 mmHg at the spinal outlet in the control model and remains close to this value (max 3.2% difference) for OBS-1 and OBS-2 (figure 6.4F and G). It is only in OBS-3 that a significant effect is observed with an increase in the amplitude of pressure pulsations to 5.67 mmHg at the interstitium outlet and a reduction to 0.38 mmHg at the spinal outlet. These changes also reflect in the pressure differences between the spinal SAS, and the fourth and lateral ventricles, presented in figure 6.5, where these spatial pressure differences rise between 0.5 and 1.5 s to a peak of 4.70 and 4.81 mmHg, respectively. A smaller, although clearly visible, increase in pressure differences is found when introducing OBS-1 and OBS-2 (figure 6.5C and F), with pressure differences between the lateral ventricles and the spinal SAS reaching a maximal value of 0.31 in the control compared to 0.44 in OBS-1 and 0.88 mmHg in OBS-2. An overview of these peak values can be found in Table 6.3. Adding an anterior obstruction also delays the peak with 0.04s for OBS-2 and 0.34s for OBS-3. Finally, to allow comparison with previous studies, the longitudinal impedance is calculated from the volumetric flow and pressure differences between the fourth ventricle and spinal SAS based on Shaffer et al. [137] over four cardiac cycles (without coughing) and led to values of longitudinal impedance of 0.19 (control), 0.43 (OBS-1), 1.02 (OBS-2), 90.29 mmHg/ml (OBS-3).

### 6.2.3 Impact of an obstruction during coughing

Finally, the effects on flow and pressure are evaluated during coughing, starting by inducing coughing in the control case without obstruction, and then gradually increasing the obstruction from OBS-1 to OBS-2 and OBS-3.

#### *6.2.3.1 CSF flow during coughing*

During coughing, a large fluid volume is forced through the foramen magnum into the intracranial compartment, leading to a subsequent negative (cranial direction) and positive (caudal direction) flow through the spinal SAS (figure 6.6A), with peak values of -18.05 and 18.02 ml/s, respectively. Meanwhile, flow through the cerebral aqueduct is unaffected. While velocities in the spinal SAS are generally low during normal arterial pulsations, they undergo an important

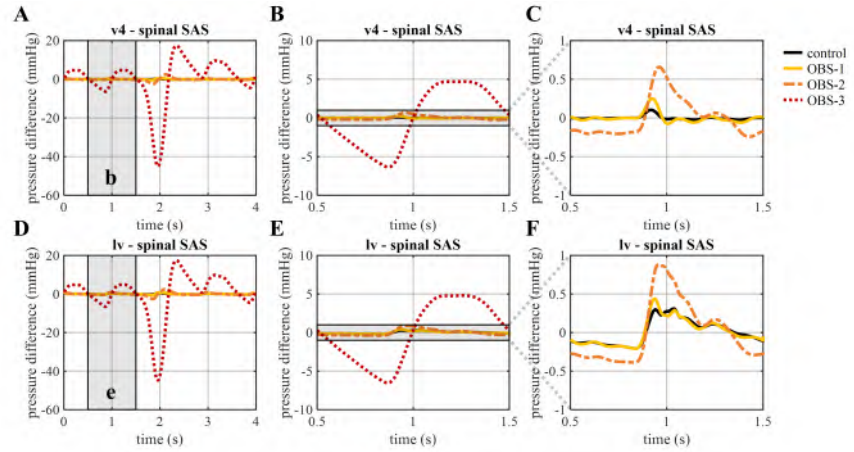


**Figure 6.5:** Pressure difference between the fourth ventricle and spinal SAS, and the lateral ventricles and spinal SAS (A, D) for four cardiac cycles, and zoomed in on one cardiac cycle between 0.5 and 1.5 s (B, E) for all cases and (C, F) without OBS-3.

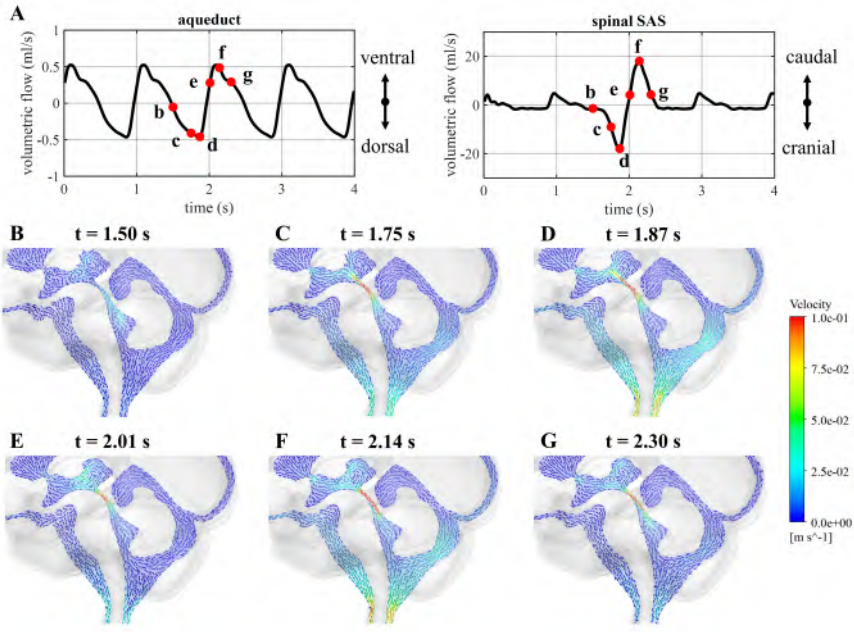


**Figure 6.6:** (A) Simulated flow through the cerebral aqueduct and the spinal SAS and visualization of the selected time points(red) during a cough. Velocity vectors in a sagittal cross-section at six different time points: (B) at the start of the cough, (C) in between, (D) at peak spinal SAS flow in cranial direction, (E) after the change in flow direction in the spinal SAS, (F) at peak spinal SAS flow in caudal direction, and (G) at the end of the cough.

increase during coughing which can be observed in the vector plots at different time points depicted in figure 6.6B-G. Velocities averaged at the cross-section of the spinal SAS (see location in figure 6.1B) reach a peak of 0.08 m/s.

When introducing different degrees of obstruction, a close overlap is observed for the volumetric flow rates through the spinal SAS (figure 6.4A) and the four outlets (figure 6.4B-E) for the control, OBS-1 and OBS-2. Only the OBS-3 leads to a significant change in the volumetric flow during coughing, with an increase in peak flow through the spinal outlet and a reduction of flow through the spinal SAS and into the interstitium outlet.

#### *6.2.3.2 CSF pressure and pressure differences during coughing*

Figure 6.4F and G show how coughing causes a single peak in intracranial CSF pressure of respectively 45.08 and 45.27 mmHg at the interstitium and spinal outlet for the healthy control. Introducing a posterior (OBS-1) and a mild posterior-anterior obstruction (OBS-2) marginally increase peak pressure at the interstitium outlet (to 45.13 and 45.56, respectively) and reduce peak pressure in the spinal compartment (to 45.26 and 45.06 mmHg, respectively). The opposite is observed in the case of OBS-3, where pressure increases at the spinal outlet to 59.59 mmHg, while it almost disappears at the interstitium outlet (figure 6.4F and G). These changes in pressure also result in an increase in peak pressure differences between the intracranial and spinal compartments (figure 6.7, Table 6.3). The % increase of these peak pressure differences can be calculated as the relative difference in peak pressure difference between the obstructed case ($dP_{OBS}$) and the control ($dP_{control}$) as shown in equation 6.9.

$$\%increase = (dP_{OBS} - dP_{control})/dP_{control} \tag{6.9}$$

**Table 6.3:** Overview of peak pressure differences both during arterial pulsations (only maximum) and during cough (both minimum and maximum).

| | Arterial peak pressure difference (mmHg) | | Coughing peak pressure difference (mmHg) | |
|---|---|---|---|---|
| | v4-spinal SAS | lv-spinal SAS | v4-spinal SAS | lv-spinal SAS |
| Control | 0.10 | 0.31 | -0.11/0.23 | -0.29/0.54 |
| OBS-1 | 0.25 | 0.44 | -0.39/0.54 | -0.59/0.85 |
| OBS-2 | 0.66 | 0.88 | -2.39/2.44 | -2.58/2.62 |
| OBS-3 | 4.70 | 4.81 | -44.99/17.42 | -44.78/17.45 |

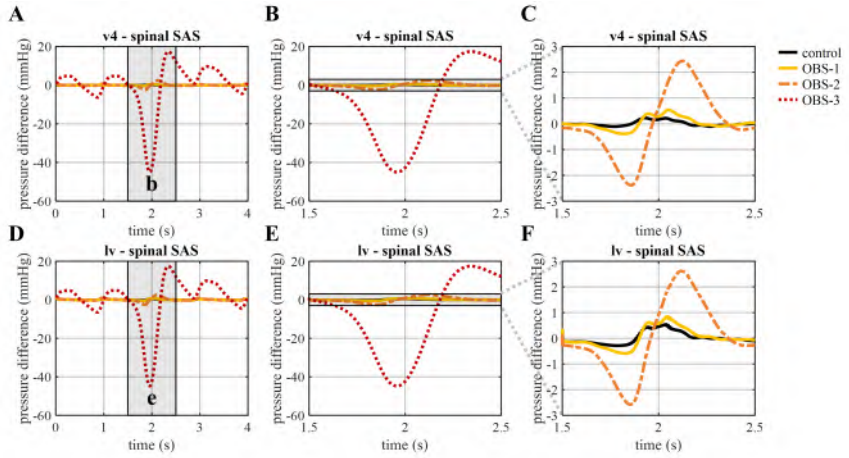


**Figure 6.7:** Pressure difference between the fourth ventricle and spinal SAS, and the lateral ventricles and spinal SAS (A, D) for four cardiac cycles, and during cough between 1.5 and 2.5 s (B, E) for all cases and (C, F) without OBS-3.

### 6.2.4 Impact of a reduction in spinal compliance

Figures 6.8, 6.9 and 6.10 visualize the pressure differences between the intracranial and spinal compartments for OBS-1, OBS-2, and OBS-3, respectively. The pre-treatment value of spinal compliance is the lowest value, but also the post-treatment value is significantly below the baseline. Here, peak pressure differences reduce with decreasing compliance during arterial pulsations for OBS-1 and OBS-2, whereas they undergo little change for OBS-3. The opposite can be observed during coughing, where pressure differences increase significantly with decreasing spinal compliance.

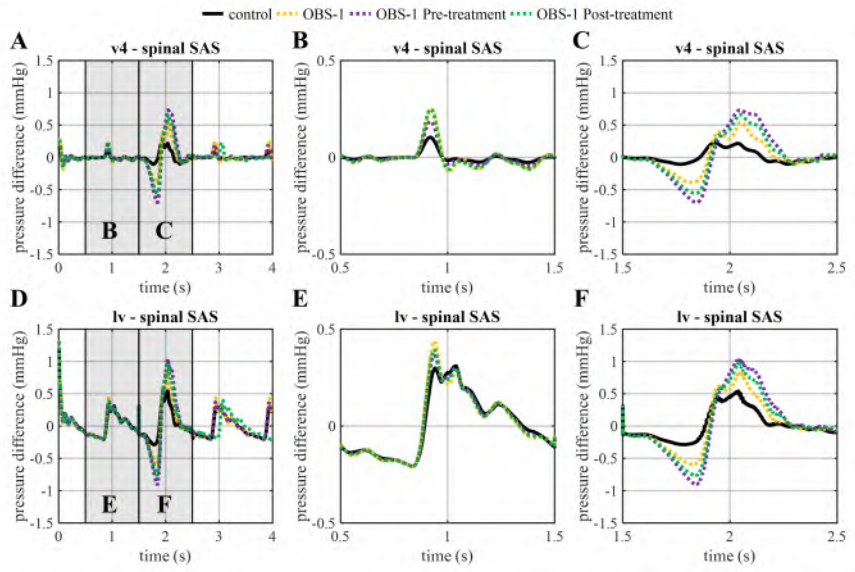


**Figure 6.8:** Pressure differences between the fourth ventricle (v4) and spinal SAS, and the lateral ventricle (lv) and spinal SAS (A, D) for four cardiac cycles, and (B, E) zoomed in on one cardiac cycle between 0.5 and 1.5 s and (C, F) during cough between 1.5 and 2.5 s for control, and OBS-1 with three values of spinal compliance: baseline (OBS-1), CMI pre-treatment (OBS-1 pre-treatment), and CMI post-treatment (OBS-1 post-treatment).

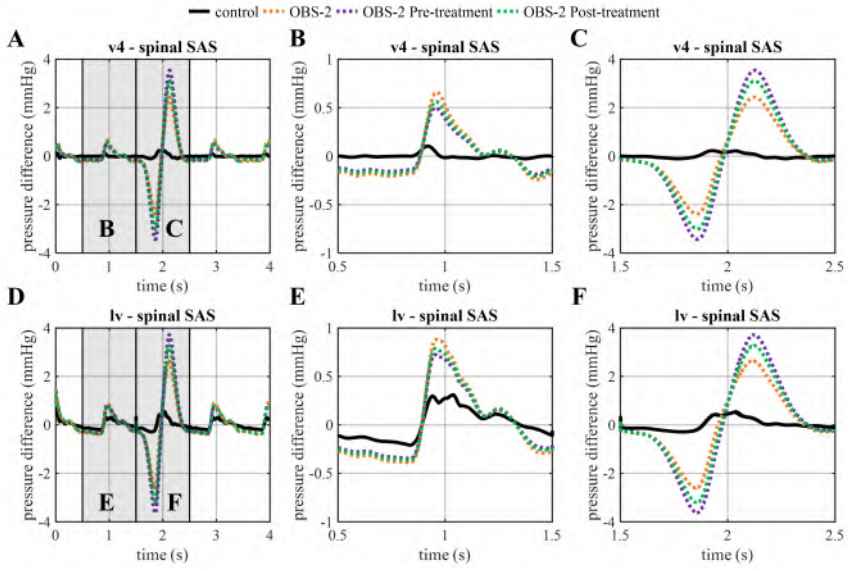


**Figure 6.9:** Pressure differences between the fourth ventricle and spinal SAS, and the lateral ventricle and spinal SAS (A, D) for four cardiac cycles, and (B, E) zoomed in on one cardiac cycle between 0.5 and 1.5 s and (C, F) during cough between 1.5 and 2.5 s for control, and OBS-2 with three values of spinal compliance: baseline (OBS-2), CMI pre-treatment (OBS-2 pre-treatment), and CMI post-treatment (OBS-2 post-treatment).

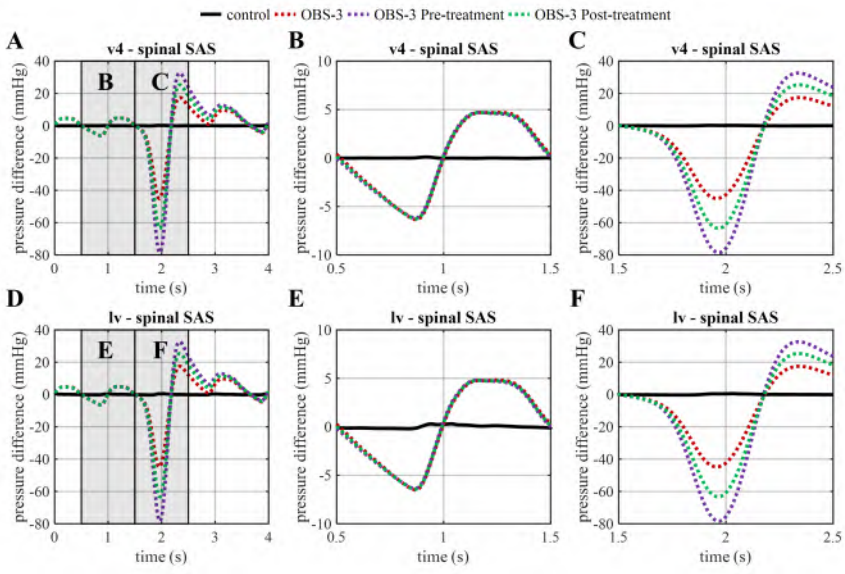


**Figure 6.10:** Pressure differences between the fourth ventricle and spinal SAS, and the lateral ventricle and spinal SAS (A, D) for four cardiac cycles, and (B, E) zoomed in on one cardiac cycle between 0.5 and 1.5 s and (C, F) during cough between 1.5 and 2.5 s for control, and OBS-3 with three values of spinal compliance: baseline (OBS-3), CMI pre-treatment (OBS-3 pre-treatment), and CMI post-treatment (OBS-3 post-treatment).

## 6.3 Discussion

In this study, the impact of different degrees of obstruction on flow distribution, pressure and local pressure differences is investigated by introducing three gradations of obstruction (OBS-1, OBS-2, and OBS-3) in a subject-specific 3D model of the cranial and upper spinal CSF circulation. This 3D model (control) was first compared with in vivo flow measurements. Next, the impact of the different obstructions was evaluated both during normal arterial pulsations and during coughing. The model allowed us to not only look at local effects, as typically done in previous studies, but also at overall effects showing an important amplification of pressure differences during coughing in presence of an obstruction and an overall redirection of the CSF flow for OBS-3.

### 6.3.1 Validating model against in vivo data

Overall, the simulated flow profiles in the cerebral aqueduct and the spinal SAS correspond to the in vivo PC-MRI measurements (figure 6.3A). The largest deviation was found for peak flow through the spinal SAS and could be the result of system-wide effects such as flow resistance throughout the 3D domain, which were not accounted for during the calculation of the inlet boundary conditions. Moreover, the target pressures have been achieved (figure 6.3H) through model calibration, with a minor deviation of 1.8 % compared to the target amplitude of pressure pulsations of 2 mmHg, which can be attributed to flow resistance in the 3D domain. Importantly, we observe a difference of 4.2 % compared to the target mean pressure of 10 mmHg, which also appears in the 0D model and is the result of transient effects of incorporating windkessel compliance (see chapter 3). Indeed, simulation with the 0D model over multiple cardiac cycles shows that the pressure eventually evolves into an equilibrium situation with a stable pressure after minutes to hours. All in all, these results demonstrate that the presented simulation approach leads to realistic pressures and flows in the subject-specific 3D model of the CSF space.

The compliance obtained in this study is 0.2965 ml/mmHg, which is in the same order but lower than compliances between 0.4 and 1.2 ml/mmHg measured in vivo [45, 150, 151]. Hence, the compliance appears to be underestimated in our model, although it should be noted that the targeted pressure is not derived from subject-specific pressure measurements and is based on multiple recordings typically performed in patients. In vivo values would lead to ICP pulsations

with amplitude between 0.5 and 1.5 mmHg in our model. Moreover, not accounting for physiological effects such as breathing or internal resistance effects (e.g. due to the presence of trabeculae in the SAS) might cause this underestimation of compliance.

### 6.3.2 Impact of an obstruction on pulsatile CSF dynamics

The tuned model is subsequently used to evaluate the impact of an obstruction as present in Chiari type 1 malformation by introducing a porous zone at the level of the foramen magnum in the CSF model. OBS-1 and OBS-2 lead to limited changes in overall intracranial and spinal pressure, and, like in the healthy control, arterial pulsations are compensated for by the compliances of both the spinal and interstitium outlet (figure 6.4). This contrasts with the obstruction in OBS-3, which seriously hampers fluid exchange between the spinal and intracranial compartments and consequently forces the interstitium outlet to take up the largest part of the CSF pulsations originating from the intracranial arteries. This can be observed as a reduction in the amplitude of flow and pressure pulsations at the spinal outlet and their increase at the intracranial outlets. An increase in amplitude of pressure pulsations in the intracranial compartment was previously reported by Magnæs et al. [45], who performed in vivo ICP recordings and found an increase in their amplitude between 94 and 126 % when establishing a cervical SAS blockage, which is lower than the increase of 189 % found between OBS-3 and the control case in this study. These larger pulsations of intracranial CSF pressure actually appear to display the effects of reduced CSF compliance, despite the total CSF compliance being unchanged.

A reduction in CSF compliance in patients with Chiari type 1 malformation was proposed based on imaging and computational studies [52] and was hypothesized from a decrease in the delay between intracranial and spinal flow peaks [58, 134, 135]. It is an interesting pathway to investigate whether overall compliance decreases in Chiari type 1 malformation, which has been suggested by previous studies, or whether the phenomenon occurs due to a disconnection of the spinal and intracranial compliance, with underutilization of either. The latter would be caused by the obstruction hindering fluid exchange between the spinal and intracranial compartments, as suggested by our results.

However, the high degree of area obstruction (>99 %) which was found to best correspond to OBS-3, might not occur in Chiari type 1 malformation. Indeed, pressure differences in previous studies have

been found to better align with those corresponding with OBS-1 and OBS-2 which induced a rise of 150 (OBS-1) and 560 % (OBS-2) in the peak pressure difference between the fourth ventricle and the spinal SAS with respect to the healthy control (figure 6.5). Simplified models reported an increase between 15 and 400 % [176, 177], and person-specific models found a difference between 32 and 149 % [130, 133, 134] indicating that specifically OBS-1 corresponds well with previous modeling studies. Moreover, the longitudinal impedance in both the control (0.19mmHg/ml) and OBS-1 (0.43 mmHg/ml) is consistent with the previously reported range of 0.17 ± 0.1 for the healthy control and 0.41 ± 0.05 mmHg/ml for Chiari type 1 malformation [137].

Figure 6.5 also shows that OBS-2 causes a delay in peak pressure difference (40ms). A delay in pressure difference between cases with and without obstruction has been reported by previous studies [175, 177] with an increasing delay when expanding the percentage obstruction. At the same time, others found that the peak in pressure difference appeared earlier [133, 135]. This earlier peak was the result of a phase shift in the input flow curve which Clarke et al. previously found to be characteristic of patients with Chiari type 1 malformation [171]. This phase shift might either be related to patient-specific differences or to physiological changes in the intracranial compartment related to the obstruction, which were not considered in this model.

### 6.3.3 Impact of an obstruction during coughing

Previous studies have suggested a role for coughing in the origin of syrinx formation in patients with Chiari type 1 malformation. Therefore, the effect of coughing, which can be described as a sharp rise and fall in ICP, was emulated by imposing a transient flow profile in the spinal compartment. To the best of our knowledge, this study is the first to infer the impact of coughing in a subject-specific in silico CFD model of the CSF space. The amplitude of the imposed flow peak was estimated based on the 0D windkessel model, which was previously presented in chapter 5. The achieved peak values of 45.3 mmHg for the spinal and 45.1 mmHg for the interstitium outlet correspond well to the pressure originally targeted (increase 35 mmHg above 10 mmHg). The physiological plausibility of the result is further supported by data reported by Lloyd et al. [42] who measured CSF flow during coughing using a real-time PC-MRI technique. A maximal cranial flow of about 10-20 ml/s was found, which is in very good agreement with the peak estimated using our approach (18 ml/s). At the same time, Lloyd et al. did not detect a caudal

peak flow, suggesting that it may take some time for the veins and consequently the CSF domain to return to the original size, which contrasts with our assumption of an immediate restoration of venous volume.

When adding an obstruction to the model, the maximal pressure difference between the lateral ventricles and the spinal SAS increases 41 (OBS-1), 184 (OBS-2), and 1,448 % (OBS-3) under the action of arterial pulsations, and the positive peak rises 56 (OBS-1), 384 (OBS-2), and 3,119 % (OBS-3) during coughing. Hence, we observed an amplification of the maximal pressure differences due to coughing compared to normal arterial pulsations (see Table 6.3). It should be noted that only an increase, but no % amplification was observed with OBS-1 for the pressure difference (positive peak) between the fourth ventricle and the spinal SAS. These results can, to some extent, be compared with available in-vivo [49, 65] and experimental [141] data, although direct comparison using absolute values is not trivial because our model does not incorporate the complete spinal SAS and interaction with dura and spinal cord, and discards possible hydrostatic pressure differences. Therefore, we choose to compare the relative changes in the variables of interest. Williams et al. [5] indicated that patients with a hindbrain hernia, and thus blockage of CSF flow, can experience a pressure difference between the ventricles and lumbar spinal SAS of over 100 mmHg compared to a pressure dissociation of about 30-35 mmHg for subjects without obstruction, which represents an increase of 208 % (between OBS-1 and OBS-2). Martin and Loth [141] investigated the impact of coughing in an in vitro model of the spinal SAS for different cases including a case with a stenosis obstructing $> 90$ % of the spinal SAS and a case with syringomyelia without stenosis. They also found a pressure difference between OBS-1 and OBS-2, with a maximal pressure difference for a case with stenosis and without stenosis (with syringomyelia) of 83 and 28.5 mmHg, respectively (an increase of 191 %) over a distance of 28 cm.

With the reduction of spinal compliance, pressure differences between the intracranial and spinal compartments during a normal arterial pulsation stayed largely the same for OBS-3 and even decreased for OBS-1 and OBS-2. The opposite was observed for coughing with a significant increase in pressure differences for all cases. This discrepancy between the effects of arterial pulsations and coughing can be related to the location of the arterial and coughing input in the intracranial and spinal compartments, respectively.

With the reduction of the spinal compliance, the buffering capacity of the spinal compartment is reduced and consequently more fluid is displaced through the foramen magnum toward the intracranial compartment. This leads to an increase of the pressure differences over the foramen magnum. The results are consistent with the study of Martin and Loth. [141] who reported a decrease in the pressure difference (between cervical and lumbar SAS) across a stenosis during coughing, following the addition of compliance in their experimental model of the spine. These findings imply that a reduction in spinal compliance as measured by Heiss et al. [70] might be an important factor contributing to critical pressure differences during coughing.

Thus, our results indicate that coughing increases and even % amplifies pressure differences between the intracranial and spinal compartments. These pressure differences further increase during coughing with reduction of spinal compliance; an elevation that was not observed during arterial pulsations. This, thereby, supports the hypothesis that coughing might cause additional strain on the hindbrain and spinal cord leading to direct pain (including headache) and might eventually contribute to long-term development and progression of syringomyelia (e.g. dilation of spinal cord due to negative spinal cord pressures) as previously suggested by Williams et al. [49] and Martin and Loth [141]. Alternatively, these pressure gradients might cause suction of CSF into the central canal [5] or support seepage of CSF through the perivascular spaces into the spinal cord [94]. Further investigation of the impact of these pressure gradients on the spinal cord parenchyma can provide us with more information on the exact mechanism of syrinx formation, but at the same time will add an extra layer of complexity to our models.

### 6.3.4 Limitations

While the 3D geometry was extracted from anatomical MRI scans, scan resolution, and post-processing (i.e. manual adjustments, imposing minimal thickness of the cranial SAS and smoothing) could influence the simulation results. Indeed, the in-domain CSF resistance might be underestimated in the current study due to the imposed minimal thickness for the cranial SAS and by not accounting for trabeculae and small blood vessels in the cranial and spinal SAS. Inlet boundary conditions are based on in vivo flow measurements which are obtained at two cross-sections of the CSF domain. To incorporate these in the model, assumptions were made regarding the origin of the given pulsations. More information on the actual motion

of the neurological tissues, and arteries joining in the circle of Willis can enable us to better match and validate the overall flow velocities in the full CSF domain. The original in vivo flow measurements are cardiac-gated, and consequently model results do not account for normal breathing, in contrast to chapter 5, but allow us to compare with results of previous studies also based on cardiac-gated measurements.

Volume compensation mechanisms and CSF absorption are the result of a complex interaction between the CSF, the intracranial and spinal veins and the lymphatic system acting over the full CSF domain. By reducing these interactions to resistors and 2-element windkessel models and coupling these to venous and lymphatic pressures, which are prescribed at a discrete number of locations, we significantly simplify the real complexity. Extending the 2-element windkessel models may improve the models ability to capture the ICP profile and possible flow delays more accurately. Additionally, adding brain parenchyma as a deformable structure and introducing a fluid-structure interface would better represent compliance effects originating from neurological tissue deformation. These compliance effects might explain among others the reported respiratory influences in the cerebral aqueduct [48, 178], which were not found in this study because of the absence of compliance in the ventricular system. However, adding extra windkessel model components or selecting material models and properties in a fluid-structure interaction model introduce additional uncertainty in the models and coupling the fluid domain with a structural domain will undoubtedly lead to an increase in computational cost. Because of low Reynolds numbers in the CSF domain ($<2000$), laminar flow was considered for all simulations. Although, Jain et al. [173] has suggested that Chiari type 1 malformation could lead to local transitional flow rather than pure laminar flow, but in-depth evaluation of possible transitional phenomena is beyond the scope of this study.

The choice for the porous zones to emulate the obstruction allows direct comparison between different degrees of obstruction and resulted in peak pressures in the same order as those for physical obstructions. However, physical obstructions might be more suited for evaluation of the local flow patterns (e.g., recirculation and bidirectional flow) and pressure differences over the whole cardiac cycle in severe obstructions (i.e., OBS-3). Also, all obstructions were considered static, thereby not accounting for possible one-way valve mechanisms [62]. Finally, we assumed that the only impact of Chiari type 1 malformation is the blockage created by the cerebellar tonsils by introducing two porous zones. However, the disorder has also been proposed

to be caused by or coexist with other changes in physiology (e.g., increased tissue stiffness and reduced spinal compliance [70]) and anatomy (e.g., smaller posterior fossa), which were not considered in this model.

## 6.4 Conclusion

In conclusion, we used our computational framework to evaluate the impact of three degrees of obstruction on CSF dynamics during pulsatile CSF flow and coughing. The simulation results indicated that coughing amplified the pressure differences between the lateral ventricles and the spinal SAS for all degrees of obstruction and that OBS-3 led to a decoupling of the spinal and intracranial compartment with effects linked to a decrease in intracranial compliance. Although further improvements and validation of the model are warranted, system-wide models of Chiari type 1 malformation as first presented in this study can provide crucial insights regarding both local and overall CSF dynamics to better understand Chiari type 1 malformation.

# IV

# Conclusion

Chapters

Chapter 7

# Conclusion and outlook

This research focused on computational modeling of the CSF flow to quantitatively assess the impact of the structural obstruction in Chiari type 1 malformation on CSF pressures and flow velocities. To realize this objective, a CFD framework was developed which allowed us to simulate CSF dynamics through the implementation of physiological processes. Important was the implementation of distributed compliance and CSF absorption as resistive and windkessel boundary conditions. In this framework, we introduced an obstruction of the foramen magnum and reduced spinal compliance allowing us to reveal both the local and system-wide impact of Chiari type 1 malformation during cardiac pulsations and coughing.

## 7.1 Development of a CFD framework for modeling CSF dynamics

The framework was first tested by imposing simplified sinusoidal boundary conditions to simulate arterial pulsations and breathing as presented in chapter 3. We found that our approach yielded pressure and flow rates within the physiological range after tuning the input parameters. We assumed that the aqueduct CSF flow is mainly driven by volume changes of the lateral ventricles, which were also found to be the main source of fluid motion when implementing mesh motion based on aMRI in chapter 4. The model introduced in chapter 3 was updated to include subject-specific CSF flow data in chapter 6.

The presented framework surpasses the state-of-the-art in CFD modeling of the CSF by not only considering relative but also absolute pressures through the implementation of resistive and windkessel boundary conditions. Intracranial (CSF) pressure is a critical parameter in central nervous system biomechanics, as an elevation of the ICP can lead to brain injury [7]. Therefore, monitoring ICP is an essential component of neurocritical care [7, 179]. In the CFD models, we could introduce physiological (e.g. CSF production and absorption, compliance, input flow) and physical (e.g. domain resistance) changes and evaluate their impact on ICP. This makes these models suitable for studying Chiari type 1 malformation (see chapter 6) and other CSF-related disorders.

The implementation of resistor and windkessel boundary conditions did not only enable modeling 3D CSF dynamics and absolute pressures simultaneously but also allowed accounting for the underlying processes of CSF absorption and compliance. With resistor and windkessel outlets, absorption into the venous and lymphatic system was taken into account. This contrasts with previous studies where lymphatic drainage was to the best of our knowledge always ignored despite its estimated contribution being up to 47 % of the total CSF absorption [38]. However, for now, the contribution of each of the outlets was arbitrarily selected because of the lack of conclusive data on the in vivo outflow percentages.

Moreover, the windkessel boundary conditions enable accounting for CSF compliance, which is a clinically relevant parameter as its value might alter in neurological conditions [180, 181]. The compliance values predicted in this study were in the same order of magnitude but consistently lower than the range of values reported in literature when only considering arterial effects. This indicated that internal resistance mechanisms and respiratory effects should be considered in models for an adequate estimation of compliance. Internal resistance might have been underestimated in the presented models because of the post-processing of the CSF geometry and by not accounting for the trabeculae and small blood vessels occupying the subarachnoid spaces.

In the model presented in chapter 3, a pulsatile inflow was imposed in the lateral ventricles to simulate the brain tissue deformation driving flow through the cerebral aqueduct, thereby ignoring a possible contribution of the third ventricle. The third ventricle has been suggested to act as a pump driving CSF motion in the brain ventricles [31]. However, when imposing deformations obtained from

aMRI (see chapter 4), we found that the volume changes of the third ventricle were much smaller than those of the lateral ventricles. Thus, our results indicate that the lateral ventricles are the main driver of CSF motion in the ventricular system, which supports our initial assumption. This finding motivates the application of the presented aMRI approach in multiple subjects, not only to confirm this finding and validate the approach presented in chapter 4 but also to advance our understanding of CSF dynamics in the ventricular system.

## 7.2 Impact of Chiari type 1 malformation on CSF dynamics

The defining feature of Chiari type 1 malformation is the descent of the cerebellar tonsils through the foramen magnum into the spinal canal thereby (partially) obstructing CSF flow between the spinal and intracranial compartments. We found that a porous zone occupying the posterior part of the spinal canal (OBS-1) induced pressure differences that acceptably matched those obtained with a physical 70 % obstruction (see chapter 5). When adding an anterior porous zone (OBS-2 and OBS-3) occupying the remaining cross-section of the foramen magnum, peak pressure differences were in the same range as physical 91 % and 99 % obstructions. However, the pressure-flow curves showed some significant differences in behavior for OBS-2 and OBS-3 in comparison with the physical obstructions. The study presented in chapter 5 indicated to what level of obstruction the selected porous zones correspond (OBS-1 to 70 %, OBS-2 to 91 %, and OBS-3 to 99 %), and signaled possible limitations of the porous zone approach compared to physical obstructions.

In chapter 6, the selected porous zones were introduced in the subject-specific model of the intracranial and upper spinal CSF space. We found that milder obstructions (OBS-1 and OBS-2) induced limited system-wide and mostly local changes in pressure and flow. These mild obstructions resulted in an increase in pressure differences in line with those reported in previous studies presenting CFD simulations in healthy subjects and patients with Chiari type 1 malformation. Significant global changes were only found with a severe obstruction (OBS-3) (corresponding to 99% physical obstruction), with an increase of the pulsatile amplitude in the intracranial compartment. This increase in amplitude can be seen as a marker for increased intracranial compliance but here was the result of a (partial) decoupling between the intracranial and spinal compartments impeding flow exchange between those two

compartments. The increased pressure amplitude was previously observed by Magnaes et al. when they completely blocked CSF exchange between the spinal and intracranial compartment [45], which is in line with our findings.

Coughing has been proposed as a possible triggering factor for syrinx formation in patients with Chiari type 1 malformation and therefore the effects of coughing were evaluated in the presented CFD model of the CSF. We found that coughing significantly elevated peak pressure differences for all three degrees of obstruction and that simultaneous reduction of spinal compliance further increased the pressure differences. Such elevation was not found during the arterial pulse, which was attributed to the original location of the pulse in the intracranial and spinal compartments, for the arterial pulsations and coughing respectively. The results of this research are indicative of a possible critical effect of coughing and, given the significant impact of compliance reduction, support investigation of other changes in the physiology besides the obstruction to understand the impact of Chiari type 1 malformation.

## 7.3 Limitations and future perspectives

In this research, we validated the CFD models by evaluating the correspondence of the simulated flow rates through two planes (i.e. cerebral aqueduct and C2 spinal SAS) with PC-MRI measurements. While the presented approach yielded a good correspondence between the simulated and targeted flows, additional flow measurements across the whole CSF domain (multi-slice PC MRI or 4D flow MRI) will be crucial to ensure accurate simulation of CSF flow in the complete domain. Moreover, expanding the validation dataset with ICP recordings, which are not trivial to collect because of the invasive nature of these recordings, would be a challenging but essential step in verifying the validity of the models.

The performance of a computational model is to a large extent determined by the geometry, the imposed physics, and the boundary conditions. The inlet and outlet boundary conditions accounted for the physiological processes impacting CSF dynamics (i.e. production, absorption, buffering, arterial pulsations, and respiratory actions). While the spatial distribution of these processes was taken into account in the presented models, the boundary conditions are still imposed at a discrete number of locations, which might differ from the more gradual and heterogenous distribution of these processes in vivo. To some extent, we addressed this issue by replacing

the uniform inflow profile in the lateral ventricles with surface motion derived from aMRI. While aMRI motion yielded a pulsatile pattern similar to the PC-MRI measurements in the cerebral aqueduct, the presented approach needs to be evaluated in multiple subjects and requires a robust method for selecting the correct scaling factor and for noise reduction. Alternatively, the impact of brain tissue motion can also be accounted for by coupling the mechanical behavior of the tissues to the fluid domain. While such approach could be considered, the benefits of adding such complexity should be weighed against the additional computational cost and uncertainty regarding the input parameters (e.g. material parameters and models).

Importantly, we only considered the specific conditions corresponding with a person lying down in an MRI scanner with a regular heartbeat and performing simple breathing maneuvers (normal respiration and coughing). This had the advantage that we could compare our results with in vivo flow measurements, but at the same time, a wide range of conditions was not explored. With humans spending most of their day either standing or sitting, a crucial next step toward understanding CSF disorders is the investigation of CSF flow in an upright position. This would require changing compliance distribution, accounting for the gravitational field, and the inclusion of the different compensatory mechanisms which avoid a serious drop in ICP when standing up (see chapter 1). Importantly, the model was found to be sufficiently robust to cope with sharp peaks during coughing and therefore should be suited for investigation of other actions large CSF displacements like Valsalva maneuvers and changes in posture.

In that regard, in the current analysis, resistor and two-element windkessel models were used to couple CSF to the neural tissues (interstitium), the lymphatic, and the venous system. Hence, simple lumped parameter models governed by constant values of compliance and resistance describe the complex downstream mechanisms. While this approach works well in standard conditions (a person lying down in MRI scanner), it might be necessary to expand these models to predict CSF dynamics in more diverse conditions (e.g. upright position). To this end, including the mechanisms controlling pressure in the venous sinuses (see chapter 1) and the lymphatic system, and accounting for condition dependent changes in CSF compliance could further advance the applicability of the current models.

In general, the model outcomes were the result of a number of assumptions and simplifications regarding the geometry, computational

mesh, location and nature of boundary conditions, and the solver settings. Some of these input parameters are uncertain, meaning that their physiological value is not known (e.g. minimal thickness of the cranial SAS, the contributions of each outlet to the total CSF absorption, and CSF domain resistance induced by the presence of trabeculae and small blood vessels). Uncertainty quantification can provide information about the sensitivity of the output parameters to the variability of the inputs and the general uncertainty regarding the obtained output. Where a mesh sensitivity was performed for each of these studies (except the aMRI study), sensitivity to the other parameters was not explored in detail and should be investigated in future work. To utilize CSF models for medical applications, validation, and assessment of the model's sensitivity to inputs will be an essential step.

For the models specifically focusing on Chiari type 1 malformation, we found that the porous zone approach induced peak pressures that were in the same range as those with a physical obstruction. Meanwhile, we also observed differences in local flow patterns and in pressure-flow behavior for high-level obstructions. These findings indicated that while a porous zone might function well as a replacement to predict peak pressure differences, a detailed evaluation of the flow and the local pressure distribution would require a realistic shape of the (partial) obstruction. Therefore, applying the presented modeling framework to multiple 3D models of healthy subjects and patients with Chiari type 1 malformation should be an interesting next step in the investigation of Chiari type 1 malformation. However, this would require a large number of scans of both healthy subjects and patients with Chiari type 1 malformation to rule out the person-person variability.

Finally, we hypothesized that large pressure differences across the obstruction in patients with Chiari type 1 malformation are associated with fluid accumulation in the spinal cord and thus syrinx development. We found that in the presence of a partial obstruction pressure differences were increased more during coughing than in resting state (arterial pulsations) and that this effect was strengthened with reduction of the spinal compliance. Imposing these pressure differences to a structural model of the spinal cord would provide an understanding of not only the impact of the obstruction on CSF dynamics but also on the spinal cord behavior and help reveal how these changes in CSF dynamics might eventually lead to syringomyelia. Important here will be the adequate modeling of the spinal cord tissue

and thus considering among others its time-dependent response and the biphasic nature.

# V

# Appendices

Chapters

APPENDIX A

# Coupling algorithm

In this chapter, more details on the implementation of the coupling algorithm for implementation of windkessel boundary conditions are provided. This approach is based on the coupling algorithm described in [147, 182]. The overview of the coupling scheme used in chapter 3 is depicted in figure A.1.

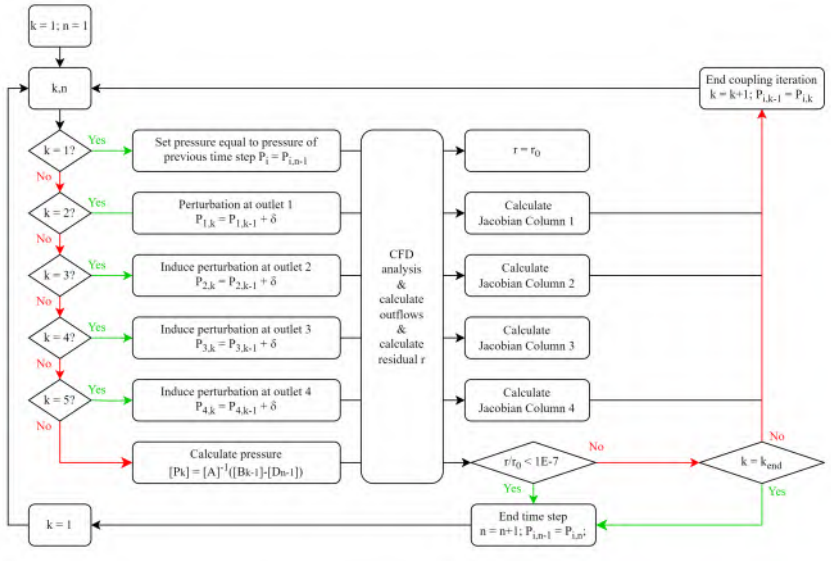


**Figure A.1:** Schematic of coupling algorithm

First, an explicit expression is derived for pressure ($P_{i,n}$) at outlet i in function of the outflow at timestep n ($Q_n$) and the pressure in the previous timestep n-1.

$$P_{i,n} = \frac{Q_{i,n}R_i + P_{i,n-1}\frac{C_iR_i}{\Delta t}}{1 + \frac{C_iR_i}{\Delta t}} \tag{A.1}$$

Each timestep is subdivided into coupling iterations and the windkessel formulation between pressure and flow is linearized for coupling iteration k and time step n.

$$\begin{cases} Q_{1,k} = Q_{1,k-1} + \sum_{i=1}^{4} \frac{\partial Q_1}{\partial P_i}\Big|_k (P_{i,k} - P_{i,k-1}) \\ Q_{2,k} = Q_{2,k-1} + \sum_{i=1}^{4} \frac{\partial Q_2}{\partial P_i}\Big|_k (P_{i,k} - P_{i,k-1}) \\ Q_{3,k} = Q_{3,k-1} + \sum_{i=1}^{4} \frac{\partial Q_3}{\partial P_i}\Big|_k (P_{i,k} - P_{i,k-1}) \\ Q_{4,k} = Q_{4,k-1} + \sum_{i=1}^{4} \frac{\partial Q_4}{\partial P_i}\Big|_k (P_{i,k} - P_{i,k-1}) \end{cases} \tag{A.2}$$

Subsequently, the linearized equations in A.2 are substituted in the windkessel equation A.1 resulting in the following set of equations.

$$\begin{cases} P_{1,k}(\frac{1}{R_1} + \frac{C_1}{\Delta t}) - \sum_{i=1}^{4} \frac{\partial Q_1}{\partial P_i}\Big|_k P_{i,k} = Q_{1,k-1} - P_{1,n-1}\frac{C_1}{\Delta t} - \sum_{i=1}^{4} \frac{\partial Q_1}{\partial P_i}\Big|_k P_{i,k-1} \\ P_{2,k}(\frac{1}{R_2} + \frac{C_2}{\Delta t}) - \sum_{i=1}^{4} \frac{\partial Q_2}{\partial P_i}\Big|_k P_{i,k} = Q_{2,k-1} - P_{2,n-1}\frac{C_2}{\Delta t} - \sum_{i=1}^{4} \frac{\partial Q_2}{\partial P_i}\Big|_k P_{i,k-1} \\ P_{3,k}(\frac{1}{R_3} + \frac{C_3}{\Delta t}) - \sum_{i=1}^{4} \frac{\partial Q_3}{\partial P_i}\Big|_k P_{i,k} = Q_{3,k-1} - P_{3,n-1}\frac{C_3}{\Delta t} - \sum_{i=1}^{4} \frac{\partial Q_3}{\partial P_i}\Big|_k P_{i,k-1} \\ P_{4,k}(\frac{1}{R_4} + \frac{C_4}{\Delta t}) - \sum_{i=1}^{4} \frac{\partial Q_4}{\partial P_i}\Big|_k P_{i,k} = Q_{4,k-1} - P_{4,n-1}\frac{C_4}{\Delta t} - \sum_{i=1}^{4} \frac{\partial Q_4}{\partial P_i}\Big|_k P_{i,k-1} \end{cases} \tag{A.3}$$

These equations are rewritten in matrix form in equation A.4.

$$\Big([R] + \frac{1}{\Delta t}[C] - [J]\Big)[P_k] = [Q_{k-1}] - \frac{1}{\Delta t}[C][P_{n-1}] - [J][P_{k-1}] \tag{A.4}$$

With Jacobian [J] in equation A.5, resistance [R] in equation A.6, and compliance matrix [C] in equation A.7

$$[J] = \begin{bmatrix} \frac{\partial Q_1}{\partial P_1}\Big|_k & \frac{\partial Q_1}{\partial P_2}\Big|_k & \frac{\partial Q_1}{\partial P_3}\Big|_k & \frac{\partial Q_1}{\partial P_4}\Big|_k \\ \frac{\partial Q_2}{\partial P_1}\Big|_k & \frac{\partial Q_2}{\partial P_2}\Big|_k & \frac{\partial Q_2}{\partial P_3}\Big|_k & \frac{\partial Q_2}{\partial P_4}\Big|_k \\ \frac{\partial Q_3}{\partial P_1}\Big|_k & \frac{\partial Q_3}{\partial P_2}\Big|_k & \frac{\partial Q_3}{\partial P_3}\Big|_k & \frac{\partial Q_3}{\partial P_4}\Big|_k \\ \frac{\partial Q_4}{\partial P_1}\Big|_k & \frac{\partial Q_4}{\partial P_2}\Big|_k & \frac{\partial Q_4}{\partial P_3}\Big|_k & \frac{\partial Q_4}{\partial P_4}\Big|_k \end{bmatrix} \tag{A.5}$$

$$[R] = \begin{bmatrix} 1/R_1 & & & \\ & 1/R_2 & & \\ & & 1/R_3 & \\ & & & 1/R_4 \end{bmatrix} \tag{A.6}$$

$$[C] = \begin{bmatrix} C_1 & & & \\ & C_2 & & \\ & & C_3 & \\ & & & C_4 \end{bmatrix} \tag{A.7}$$

Finally, the pressures at the outlets contained in the matrix $[P_k]$ can be written in function of the outlet pressures in previous timestep $[P_{n-1}]$, and the pressure $[P_{k-1}]$ and flow $[Qk-1]$ in the previous coupling iteration.

$$[P_k] = \Big([R] + \frac{1}{\Delta t}[C] - [J]\Big)^{-1}\Big([Q_{k-1}] - \frac{1}{\Delta t}[C][P_{n-1}] - [J][P_{k-1}]\Big) \tag{A.8}$$

This can be written in short as equation A.9.

$$[P_k] = [A]^{-1}([B_{k-1}] - [D_{n-1}]) \tag{A.9}$$

The Jacobian [J] contains the derivatives of flow with respect to pressure. These derivatives are approximated by finite differences. Following figure A.1, the first five coupling iterations are used to calculate the Jacobian, whereby a perturbation $\delta$ is subsequently added to each outlet (equation A.10).

$$
\begin{aligned}
k=1 \Rightarrow & \begin{cases} P_{1,1}=P_{1,n-1} \\ P_{2,1}=P_{2,n-1} \\ P_{3,1}=P_{3,n-1} \\ P_{4,1}=P_{4,n-1} \end{cases} \Rightarrow \begin{cases} Q_{1,1} \\ Q_{2,1} \\ Q_{3,1} \\ Q_{4,1} \end{cases} \\
k=2 \Rightarrow & \begin{cases} P_{1,2}=P_{1,1}+\delta \\ P_{2,2}=P_{2,1} \\ P_{3,2}=P_{3,1} \\ P_{4,2}=P_{4,1} \end{cases} \Rightarrow \begin{cases} Q_{1,2} \\ Q_{2,2} \\ Q_{3,2} \\ Q_{4,2} \end{cases} \\
k=3 \Rightarrow & \begin{cases} P_{1,3}=P_{1,2} \\ P_{2,3}=P_{2,2}+\delta \\ P_{3,3}=P_{3,2} \\ P_{4,3}=P_{4,2} \end{cases} \Rightarrow \begin{cases} Q_{1,3} \\ Q_{2,3} \\ Q_{3,3} \\ Q_{4,3} \end{cases} \\
k=4 \Rightarrow & \begin{cases} P_{1,4}=P_{1,3} \\ P_{2,4}=P_{2,3} \\ P_{3,4}=P_{3,3}+\delta \\ P_{4,4}=P_{4,3} \end{cases} \Rightarrow \begin{cases} Q_{1,4} \\ Q_{2,4} \\ Q_{3,4} \\ Q_{4,4} \end{cases} \\
k=5 \Rightarrow & \begin{cases} P_{1,5}=P_{1,4} \\ P_{2,5}=P_{2,4} \\ P_{3,5}=P_{3,4} \\ P_{4,5}=P_{4,4}+\delta \end{cases} \Rightarrow \begin{cases} Q_{1,5} \\ Q_{2,5} \\ Q_{3,5} \\ Q_{4,5} \end{cases}
\end{aligned}
\tag{A.10}
$$

This perturbation impacts the flow $Q_{i,k+1}$ through the different outlets i = 1-4. For each coupling iteration k, four elements of the Jacobian are calculated by dividing the flow differences for outlets $i = 1-4$ by the perturbation of outlet j as depicted in equation A.11.

$$
\left.\frac{\partial Q_i}{\partial P_j}\right|_k = \frac{Q_{i,k}-Q_{i,k-1}}{P_{j,k}-P_{j,k-1}} = \frac{Q_{i,k}-Q_{i,k-1}}{\delta} \tag{A.11}
$$

The Jacobian is then applied to derive the pressure following equation A.9. Where a Fluent built-in absolute convergence criterion is applied for the solver iterations, a relative convergence criterion is used to check the convergence of each coupling iteration k>1.

$$
r = \sqrt{\sum_{i=1}^{4}\left(Q_{i,k}-P_{i,k}(\frac{1}{R_i}+\frac{C_i}{\Delta t})+P_{i,n-1}\frac{C_i}{\Delta t}\right)^2} < 1E-7\cdot r_0 \tag{A.12}
$$

In this equation, $Q_{i,k}$ and $P_{i,k}$ are the flow and pressure corresponding to coupling iteration k, $P_{i,n-1}$ is the pressure in the previous timestep (n-1), and $r_0$ is the residual corresponding to coupling iteration k = 1. When this condition is fulfilled, the solution advances to the next timestep (n+1) and k is set to 1. When the criterion is not met, a next couplings iteration is started unless the final coupling iteration $k_{end}$ was reached.

Where the equations and commands are contained in the UDF file, journal files manage the subsequent actions of applying pressure, solving the Navier-Stokes equation, checking the convergence, and finally printing the results. In the model, presented in chapter 6, the coupling algorithm is adapted by changing the convergence criterion for the coupling iterations (see equation A.13)and varying the magnitude of the perturbation $\delta$ when the residual of the coupling iteration increased compared to the previous coupling iteration ($r_k$). An overview of the adapted algorithm is visualized in figure A.2.

$$r = \sqrt{\sum_{i=1}^{4} \left( Q_{i,k} - P_{i,k}(\frac{1}{R_i} + \frac{C_i}{\Delta t}) + P_{i,n-1}\frac{C_i}{\Delta t} \right)^2} < 1E-3 \cdot Q_{3,k} \tag{A.13}$$

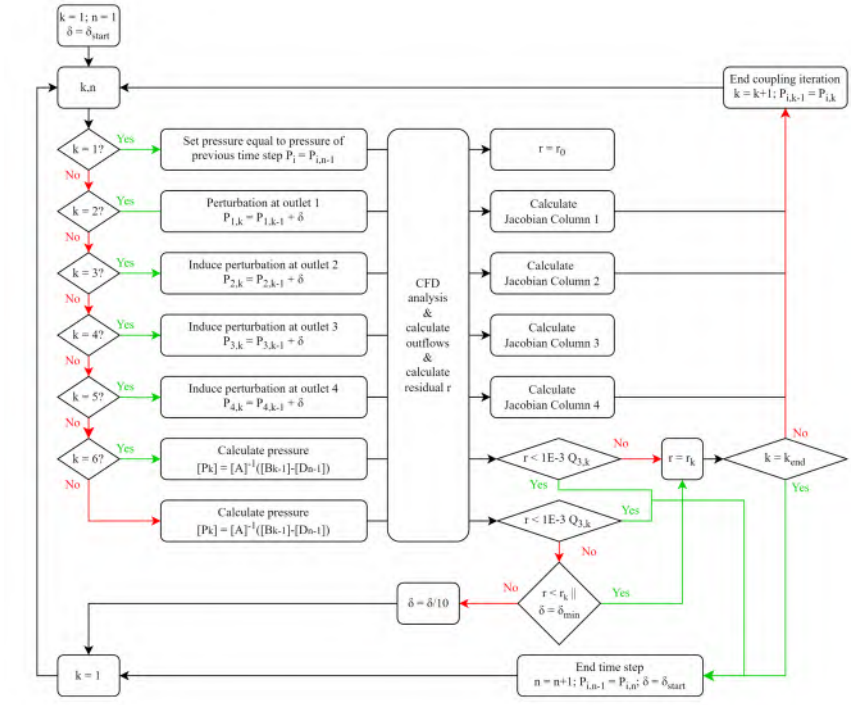


**Figure A.2:** schematic of the updated coupling algorithm with adapted convergence criterion and a variable pressure perturbation $\delta$

APPENDIX B

# Segmentation of 3D CSF volumes

In this chapter, the methods used to obtain the 3D CSF volumes comprising the cerebral ventricles, the cranial SAS, and the upper spinal SAS are explained. We, here, focus on the approach used for the computational models presented in chapter 5 and 6.

The first step was the semi-automatic extraction of the CSF volumes by applying the thresholding and region growing functions in Mimics (Materialize, Leuven, Belgium) on T2 MR images. T2 MR images are suitable for semi-automatic extraction because CSF is colored white, providing contrast with the surrounding gray tissues. We, however, could not use the resulting 3D volumes as direct input for the computational models because of multiple false connections between the ventricles and the cranial SAS and incomplete CSF conduits when applying higher thresholds (see figure B.1A). A high threshold means that only cells with high brightness are selected. To have all conduits intact (e.g. cerebral aqueduct) and remove the false connections, a lower threshold was imposed, and manual corrections were performed (see figure B.1B).

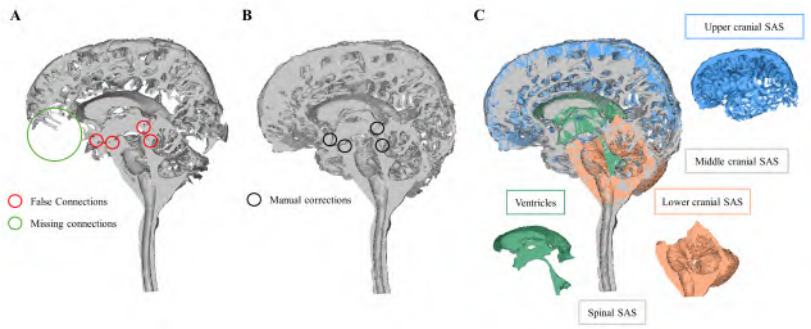


**Figure B.1:** Segmentation of 3D CSF space for the model presented in chapter 5 and 6. (A) 3D volume obtained through automatic segmentation (with high gray value threshold) with red circles indicating the resulting false connections between the ventricles and the cranial SAS. (B) 3D volume obtained through automatic segmentation (with lower gray value threshold) and manual corrections removing the false connections between the ventricles and the cranial SAS. (C) Division of the initial 3D volume into parts with removal of the cerebellar sulci (in lower cranial SAS) and segmented volumes protruding deep into the brain parenchyma (upper cranial SAS).

The resulting cranial SAS volume was complex and discontinuous with local expansions due to CSF seeping into the sulci of the cerebrum and the cerebellum and multiple holes due to local reductions of the SAS thickness. To facilitate meshing of the CSF domain and to ensure a reasonable computational cost, the complexity of extracted cranial SAS volume was reduced. First, the cerebellar sulci and the segmented volumes protruding deep into the brain parenchyma were manually removed as depicted in figure B.1C. Then, a uniform layer was added to the segmented geometry and the cerebral sulci were manually smoothed thereby only preserving the largest structures as shown in figure B.2. The thickness of the uniform layer was selected to be 2 mm (4 pixels) based on the width of the spinal SAS, which ranged between 1.5 and 3.5 mm. Imposing this uniform layer enforced a minimal thickness for the cranial SAS. As a result, the non-uniform cranial SAS was locally expanded in the regions surrounding the cerebrum whereas the effects of this layer closer to the craniocervical junction were limited because of widening of the cranial SAS. Because of the focus of the current work on the craniocervical junction, it was judged that the impact of these modifications to the cranial SAS on the evaluated variables would be minimal, and therefore this impact was not evaluated.

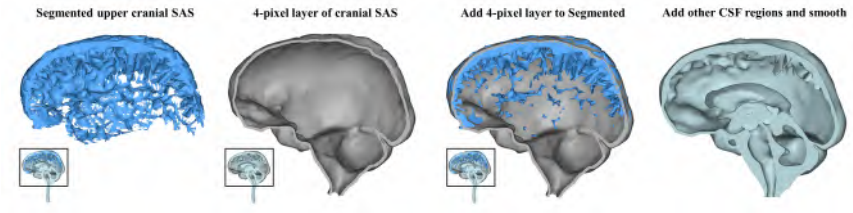


**Figure B.2:** A 4-pixel layer was added to the segmented volume of the upper cranial SAS. The union of those two volumes was thereafter combined with the volumes of the other CSF regions and the final geometry was smoothed to obtain the figure on the right.

APPENDIX C

# Mesh sensitivity study

This chapter provides additional information regarding the mesh sensitivity study performed to select the computational mesh in chapter 6. The mesh sensitivity study was conducted evaluating two different parameters: the maximal velocity in the cerebral aqueduct and the pressure difference between a plane in the lateral ventricles (lv) and the spinal SAS (see figure 6.1 for the location of these planes). Four different meshes are considered composed of 0.41 million, 1.14 million , 1.97 million, and 4.29 million volumes.

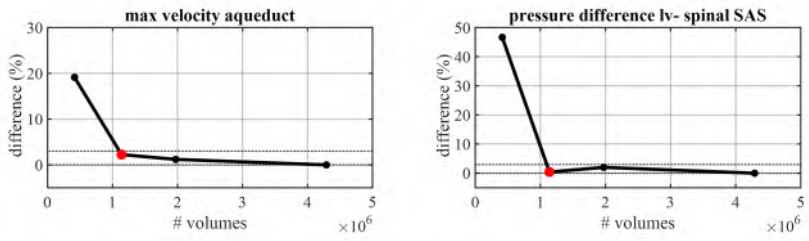


**Figure C.1:** Mesh sensitivity study curve with the % difference being a relative difference with respect to the results obtained for the finest mesh, which had 4.29 million volumes. The selected mesh is depicted in red.

In figure C.1, the % changes of these two parameters for each mesh compared to the finest mesh were evaluated showing a difference of less than 3% for the mesh with 1.14 million elements. The mesh

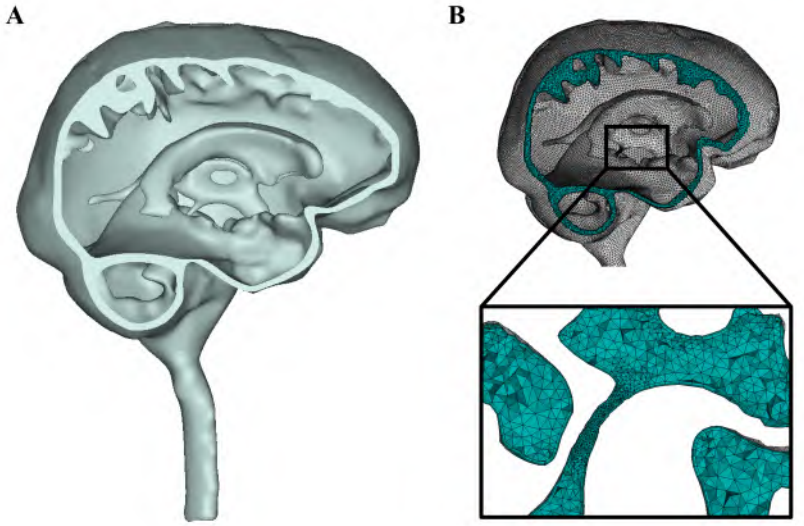


**Figure C.2:** (a) 3D geometry of model and (b) computational mesh with refinement in the cerebral aqueduct.

is visualized in figure C.2. In table C.1 the mesh properties of the selected mesh are presented.

**Table C.1:** Properties corresponding to the selected mesh

| | |
|---|---|
| **Global mesh size** | |
| Global element seed size | 3 |
| max element | |
| Min size limit | 0.5 |
| Elements in gap | 1 |
| Refinement | 5 |
| **Prism meshing parameters** | |
| Growth law | exponential |
| Height ratio | 2 |
| Number of layers | 3 |
| Total height | 0.6 |
| Min prism quality | 0.2 |
| Filet ratio | 1 |
| Max prism angle | 180 |
| Max height over base | 0.8 |
| Max height over base | 1 |
| Number of surface smoothing steps | 5 |
| Number of volume smoothing steps | 0 |

# Bibliography


[1] S. W. Bothwell, D. Janigro and A. Patabendige, 'Cerebrospinal fluid dynamics and intracranial pressure elevation in neurological diseases', *Fluids and Barriers of the CNS*, vol. 16, pp. 1–18, 1 2019.

[2] D. E. Sunny, M. Amoo, M. A. Breiki, E. D. W. Teng, J. Henry and M. Javadpour, 'Prevalence of incidental intracranial findings on magnetic resonance imaging: A systematic review and meta-analysis', *Acta Neurochirurgica*, vol. 164, pp. 2751–2765, 10 2022.

[3] A. F. Bezuidenhout, Y.-M. Chang, C. B. Heilman and R. A. Bhadelia, 'Headache in chiari malformation', *Neuroimaging Clinics of North America*, vol. 29, pp. 243–253, 2 2019.

[4] E. N. Kahn, K. M. Muraszko and C. O. Maher, 'Prevalence of chiari i malformation and syringomyelia', *Neurosurgery Clinics of North America*, vol. 26, pp. 501–507, 4 2015.

[5] B. Williams, 'On the pathogenesis of syringomyelia: A review', *Journal of the Royal Society of Medicine*, vol. 73, pp. 798–806, 11 1980.

[6] P. W. Carpenter, K. Berkouk and A. D. Lucey, 'Pressure wave propagation in fluid-filled co-axial elastic tubes part 2: Mechanisms for the pathogenesis of syringomyelia', *Journal of Biomechanical Engineering*, vol. 125, pp. 857–863, 6 2004.

[7] H. Dai, X. Jia, L. Pahren, J. Lee and B. Foreman, *Intracranial pressure monitoring signals after traumatic brain injury: A narrative overview and conceptual data science framework*, 2020.

[8] S. Y. Ilik, T. Otani, S. Yamada, Y. Watanabe and S. Wada, 'A subject-specific assessment of measurement errors and their correction in cerebrospinal fluid velocity maps using 4d flow mri', *Magnetic Resonance in Medicine*, vol. 87, pp. 2412–2423, 5 2022.

[9] V. Kurtcuoglu, K. Jain and B. A. Martin, 'Modelling of cerebrospinal fluid flow by computational fluid dynamics', in K. Miller, Ed. Springer International Publishing, 2019, pp. 215–241.

[10] Y. Lei, H. Han, F. Yuan, A. Javeed and Y. Zhao, 'The brain interstitial system: Anatomy, modeling, in vivo measurement, and applications', *Progress in Neurobiology*, vol. 157, pp. 230–246, 2017, New Perspectives on Healthy Aging.

[11] D. B. McMillan and R. J. Harris, 'Chapter f - nervous tissue', in *An Atlas of Comparative Vertebrate Histology*, D. B. McMillan and R. J. Harris, Eds., San Diego: Academic Press, 2018, pp. 141–170.

[12] F. H. Netter, 'Atlas of Human Anatomy E-Book : Digital EBook'. Elsevier, 2018.

[13] D. D. Kegel, J. Vastmans, H. Fehervary, B. Depreitere, J. V. Sloten and N. Famaey, 'Biomechanical characterization of human dura mater', *Journal of the Mechanical Behavior of Biomedical Materials*, vol. 79, pp. 122–134, 2018.

[14] A. B. Costanza and S. Abdi, 'Chapter 79 - epidural steroid injections', in *Current Therapy in Pain*, H. S. SMITH, Ed., Philadelphia: W.B. Saunders, 2009, pp. 582–587.

[15] M. W. Galper, T. P. Naidich, G. M. Kleinman, E. G. Stein and P. A. Lento, 'Chapter 8 - cranial meninges', in *Imaging of the Brain*, T. P. Naidich, M. Castillo, S. Cha and J. G. Smirniotopoulos, Eds., Philadelphia: W.B. Saunders, 2013, pp. 101–122.

[16] D. L. Felten, M. K. O'Banion and M. S. Maida, '6 - ventricles and the cerebrospinal fluid', in *Netter's Atlas of Neuroscience (Third Edition)*, D. L. Felten, M. K. O'Banion and M. S. Maida, Eds., Third Edition, Philadelphia: Elsevier, 2016, pp. 85–91.

[17] S. Rai, S. Srivastava, M. Kamath, B. V. Murlimanju, G. Parmar and G. Chebrolu, 'Delineation of subarachnoid cisterns using ct cisternography, ct brain positive and negative contrast, and a three dimensional mri sequence: A pictorial review', *Cureus*, vol. 14, e23741, 4 2022.

[18] P. Rea, 'Chapter 2 - essential anatomy and function of the brain', in *Essential Clinical Anatomy of the Nervous System*, P. Rea, Ed., San Diego: Academic Press, 2015, pp. 51–76.

[19] 'Gross anatomy', in *The Human Central Nervous System*. Berlin, Heidelberg: Springer Berlin Heidelberg, 2008, pp. 67–93.

[20] L. Sakka, G. Coll and J. Chazal, *Anatomy and physiology of cerebrospinal fluid*, 2011.

[21] J. L. Chazen *et al.*, 'Automated segmentation of mr imaging to determine normative central nervous system cerebrospinal fluid volumes in healthy volunteers', *Clinical Imaging*, vol. 43, pp. 132–135, 2017.

[22] L. R. Sass, M. Khani, G. C. Natividad, R. S. Tubbs, O. Baledent and B. A. Martin, 'A 3d subject-specific model of the spinal subarachnoid space with anatomically realistic ventral and dorsal spinal cord nerve rootlets', *Fluids and Barriers of the CNS*, vol. 14, p. 36, 1 2017.

[23] B. A. Martin and S. Heidari Pahlavian, 'Chapter 5 - anatomy and physiology of cerebrospinal fluid dynamics', in *Nervous System Drug Delivery*, R. R. Lonser, M. Sarntinoranont and K. Bankiewicz, Eds., Academic Press, 2019, pp. 73–89.

[24] R. L. Drake, H. G. 1.-1. (viaf)57675618, A. W. M. Mitchell and W. Vogl, 'Gray's anatomy for students', 2nd ed. Philadelphia, 2010.

[25] J. Li, J. Wang, X.-e. Wei, Y.-w. Zhao, F. Wang and Y.-h. Li, 'Examination of structural variations of the circle of willis by 3d time-of-flight magnetic resonance angiography', *Frontiers in Neuroscience*, vol. 14, 2020.

[26] R. Spector, S. R. Snodgrass and C. E. Johanson, 'A balanced view of the cerebrospinal fluid composition and functions: Focus on adult humans', *Experimental Neurology*, vol. 273, pp. 57–68, 2015.

[27] J. Shapey and A. Toma, 'Chapter 1 - cerebrospinal fluid physiology', in R. S. Tubbs, J. Iwanaga, E. B. Rizk, A. V. DAntoni and A. S. Dumont, Eds. Academic Press, 2023, pp. 1–15.

[28] J. J. Iliff *et al.*, 'A paravascular pathway facilitates csf flow through the brain parenchyma and the clearance of interstitial solutes, including amyloid ', *Science Translational Medicine*, vol. 4, 147ra111–147ra111, 147 2012, doi: 10.1126/scitranslmed.3003748.

[29] N. A. Jessen, A. S. F. Munk, I. Lundgaard and M. Nedergaard, 'The glymphatic system: A beginners guide', *Neurochemical Research*, vol. 40, pp. 2583–2599, 12 2015.

[30] G. Kellie, 'An account of the appearances observed in the dissection of two of three individuals presumed to have perished in the storm of the 3d, and whose bodies were discovered in the vicinity of leith on the morning of the 4th, november 1821; with some reflection', *Transactions. Medico-Chirurgical Society of Edinburgh*, vol. 1, pp. 84–122, 1824.

[31] M. Matsumae *et al.*, 'Changing the currently held concept of cerebrospinal fluid dynamics based on shared findings of cerebrospinal fluid motion in the cranial cavity using various types of magnetic resonance imaging techniques', *Neurologia Medico-Chirurgica*, vol. 59, pp. 133–146, 4 2019, CSF flow is not cicrculatory flow, but a combination of various directions of flow in the ventricles and SAS and the acceleartion of CSF motion differs depending on CSF space.

[32] T. O. Wichmann, H. H. Damkier and M. Pedersen, 'A brief overview of the cerebrospinal fluid system and its implications for brain and spinal cord diseases', *Frontiers in Human Neuroscience*, vol. 15, 2022.

[33] M. Klarica, M. Rado and D. Orekovi, 'The movement of cerebrospinal fluid and its relationship with substances behavior in cerebrospinal and interstitial fluid', *Neuroscience*, vol. 414, pp. 28–48, 2019.

[34] R. C. Rubin, E. S. Henderson, A. K. Ommaya, M. D. Walker and D. P. Rall, 'The production of cerebrospinal fluid in man and its modification by acetazolamide', *Journal of Neurosurgery*, vol. 25, no. 4, pp. 430–436, 1966.

[35] T. Brinker, E. Stopa, J. Morrison and P. Klinge, *A new look at cerebrospinal fluid circulation*, 2014.

[36] M. Pollay, 'The function and structure of the cerebrospinal fluid outflow system', *Cerebrospinal Fluid Research*, vol. 7, p. 9, 1 2010.

[37] K. WELCH and V. FRIEDMAN, 'The cerebrospinal fluid valves', *Brain*, vol. 83, pp. 454–469, 3 1960.

[38] H. F. Cserr, C. J. Harling-Berg, P. M. Knopf and H. F. Cserr, *Review drainage of brain extracellular fluid into blood and deep cervical lymph and its immunological significance*, 1992.

[39] M. Matsumae *et al.*, *Research into the physiology of cerebrospinal fluid reaches a new horizon: Intimate exchange between cerebrospinal fluid and interstitial fluid may contribute to maintenance of homeostasis in the central nervous system*, 2016.

[40] J. H. Ahn *et al.*, 'Meningeal lymphatic vessels at the skull base drain cerebrospinal fluid', *Nature*, vol. 572, pp. 62–66, 7767 2019.

[41] T. O. Wichmann, H. H. Damkier and M. Pedersen, 'A brief overview of the cerebrospinal fluid system and its implications for brain and spinal cord diseases', *Frontiers in Human Neuroscience*, vol. 15, 2022.

[42] R. A. Lloyd *et al.*, 'Respiratory cerebrospinal fluid flow is driven by the thoracic and lumbar spinal pressures', *Journal of Physiology*, vol. 598, pp. 5789–5805, 24 2020.

[43] E. Piersanti, M. E. Rognes and V. Vinje, 'Are brain displacements and pressures within the parenchyma induced by surface pressure differences? a computational modelling study', *PLOS ONE*, vol. 18, e0288668, 12 2023.

[44] L. Gergelé and R. Manet, 'Postural regulation of intracranial pressure: A critical review of the literature', in B. Depreitere, G. Meyfroidt and F. Güiza, Eds. Springer International Publishing, 2021, pp. 339–342.

[45] B. Magnæs, 'Clinical studies of cranial and spinal compliance and the craniospinal flow of cerebrospinal fluid', *British Journal of Neurosurgery*, vol. 3, pp. 659–668, 6 1989.

[46] R. W. Tain, A. M. Bagci, B. L. Lam, E. M. Sklar, B. Ertl-Wagner and N. Alperin, 'Determination of cranio-spinal canal compliance distribution by mri: Methodology and early application in idiopathic intracranial hypertension', *Journal of Magnetic Resonance Imaging*, vol. 34, pp. 1397–1404, 6 2011.

[47] S. Yamada *et al.*, 'Influence of respiration on cerebrospinal fluid movement using magnetic resonance spin labeling', *Fluids and Barriers of the CNS*, vol. 10, p. 36, 1 2013.

[48] G. Aktas *et al.*, 'Spinal csf flow in response to forced thoracic and abdominal respiration', *Fluids and Barriers of the CNS*, vol. 16, p. 10, 1 2019.

[49] B. Williams, 'Simultaneous cerebral and spinal fluid pressure recordings: I. technique, physiology, and normal results', *Acta Neurochirurgica*, vol. 58, pp. 167–185, 3 1981.

[50] K. Barami and S. Sood, *The cerebral venous system and the postural regulation of intracranial pressure: Implications in the management of patients with cerebrospinal fluid diversion*, 2016.

[51] P. Holmlund *et al.*, 'Venous collapse regulates intracranial pressure in upright body positions', *American Journal of Physiology - Regulatory Integrative and Comparative Physiology*, vol. 314, R377–R385, 3 2018.

[52] N. Alperin, S. G. Hushek, S. H. Lee, A. Sivaramakrishnan and T. Lichtor, 'Mri study of cerebral blood flow and csf flow dynamics in an upright posture: The effect of posture on the intracranial compliance and pressure', W. S. Poon *et al.*, Eds., Springer Vienna, 2005, pp. 177–181.

[53] M. Muccio *et al.*, 'Upright versus supine mri: Effects of body position on craniocervical csf flow', *Fluids and Barriers of the CNS*, vol. 18, p. 61, 1 2021.

[54] A. Zisakis, R. Sun, J. Pepper and G. Tsermoulas, 'Chiari malformation type 1 in adults', in C. D. Rocco, Ed. Springer International Publishing, 2023, pp. 149–173.

[55] N. S. Elliott, C. D. Bertram, B. A. Martin and A. R. Brodbelt, 'Syringomyelia: A review of the biomechanics', *Journal of Fluids and Structures*, vol. 40, pp. 1–24, 2013.

[56] S. Yildiz *et al.*, 'Quantifying the influence of respiration and cardiac pulsations on cerebrospinal fluid dynamics using real-time phase-contrast mri', *Journal of Magnetic Resonance Imaging*, vol. 46, pp. 431–439, 2 2017.

[57] A. C. Bunck *et al.*, 'Magnetic resonance 4d flow characteristics of cerebrospinal fluid at the craniocervical junction and the cervical spinal canal', *European Radiology*, vol. 21, pp. 1788–1796, 8 2011.

[58] A. C. Bunck *et al.*, 'Magnetic resonance 4d flow analysis of cerebrospinal fluid dynamics in chiari i malformation with and without syringomyelia', *European Radiology*, vol. 22, pp. 1860–1870, 9 2012.

[59] T. J. Buell, J. D. Heiss and E. H. Oldfield, 'Pathogenesis and cerebrospinal fluid hydrodynamics of the chiari i malformation', *Neurosurgery Clinics of North America*, vol. 26, pp. 495–499, 4 2015.

[60] J. Nash, J. S. Cheng, G. A. Meyer and B. F. Remler, 'Chiari type i malformation: Overview of diagnosis and treatment', *WMJ : official publication of the State Medical Society of Wisconsin*, vol. 101, pp. 35–40, 8 2002.

[61] A. M. Olszewski and M. R. Proctor, 'Headache, chiari i malformation and foramen magnum decompression', *Current Opinion in Pediatrics*, vol. 30, 6 2018.

[62] B. Williams, 'Syringomyelia.' *British Medical Journal*, vol. 1, p. 434, 5693 1970.

[63] T. Isu, Y. Iwasaki, M. Akino and H. Abe, 'Hydrosyringomyelia associated with a chiari i malformation in children and adolescents', *Neurosurgery*, vol. 26, 4 1990.

[64] G. Pinna, F. Alessandrini, A. Alfieri, M. Rossi and A. Bricolo, 'Cerebrospinal fluid flow dynamics study in chiari i malformation: Implications for syrinx formation', *Neurosurgical Focus FOC*, vol. 8, pp. 1–8, 3 2000.

[65] B. Williams, 'Simultaneous cerebral and spinal fluid pressure recordings: 2. cerebrospinal dissociation with lesions at the foramen magnum', *Acta Neurochirurgica*, vol. 59, pp. 123–142, 1 1981.

[66] T. H. Milhorat *et al.*, 'Chiari i malformation redefined: Clinical and radiographic findings for 364 symptomatic patients', *Neurosurgery*, vol. 44, 5 1999.

[67] M. Ball and A. Dayan, 'Pathogenesis of syringomyelia', *The Lancet*, vol. 300, pp. 799–801, 7781 1972.

[68] E. H. Oldfield, K. Muraszko, T. H. Shawker and N. J. Patronas, 'Pathophysiology of syringomyelia associated with chiari i malformation of the cerebellar tonsils: Implications for diagnosis and treatment', *Journal of Neurosurgery*, vol. 80, pp. 3–15, 1 1994.

[69] J. D. Heiss *et al.*, 'Elucidating the pathophysiology of syringomyelia', *Journal of Neurosurgery*, vol. 91, pp. 553–562, 4 1999.

[70] J. D. Heiss *et al.*, 'Pathophysiology of primary spinal syringomyelia: Clinical article', *Journal of Neurosurgery: Spine SPI*, vol. 17, pp. 367–380, 5 2012.

[71] C. D. Bertram and M. Heil, 'A poroelastic fluid/structure-interaction model of cerebrospinal fluid dynamics in the cord with syringomyelia and adjacent subarachnoid-space stenosis', *Journal of Biomechanical Engineering*, vol. 139, 1 2017.

[72] N. S. J. Elliott, D. A. Lockerby and A. R. Brodbelt, 'The pathogenesis of syringomyelia: A re-evaluation of the elastic-jump hypothesis', *Journal of Biomechanical Engineering*, vol. 131, 4 2009.

[73] B. A. Martin, R. Labuda, T. J. Royston, J. N. Oshinski, B. Iskandar and F. Loth, 'Spinal subarachnoid space pressure measurements in an in vitro spinal stenosis model: Implications on syringomyelia theories', *Journal of Biomechanical Engineering*, vol. 132, 11 2010.

[74] S. Butensky, S. Rodgers, S. Baron, S. Schneider and M. Mittler, 'Comparison of surgical outcomes in patients with chiari type i malformation receiving posterior fossa decompression with and without duraplasty', *Child's Nervous System*, vol. 36, pp. 1399–1405, 7 2020.

[75] S. Chotai and A. Medhkour, 'Surgical outcomes after posterior fossa decompression with and without duraplasty in chiari malformation-i', *Clinical Neurology and Neurosurgery*, vol. 125, pp. 182–188, 2014.

[76] B. Langridge, E. Phillips and D. Choi, *Chiari malformation type 1: A systematic review of natural history and conservative management*, 2017.

[77] O. Balédent *et al.*, 'Brain hydrodynamics study by phase-contrast magnetic resonance imaging transcranial color doppler', *Journal of Magnetic Resonance Imaging*, vol. 24, pp. 995–1004, 5 2006.

[78] G. Williams *et al.*, 'In vitro evaluation of cerebrospinal fluid velocity measurement in type i chiari malformation: Repeatability, reproducibility, and agreement using 2d phase contrast and 4d flow mri', *Fluids and Barriers of the CNS*, vol. 18, 1 2021.

[79] S. H. Pahlavian *et al.*, 'Accuracy of 4d flow measurement of cerebrospinal fluid dynamics in the cervical spine: An in vitro verification against numerical simulation', *Annals of Biomedical Engineering*, vol. 44, pp. 3202–3214, 11 2016.

[80] A. Almudayni *et al.*, 'Magnetic resonance imaging of the pulsing brain: A systematic review', *Magnetic Resonance Materials in Physics, Biology and Medicine*, vol. 36, pp. 3–14, 1 2023.

[81] S. H. Pahlavian, F. Loth, M. Luciano, J. Oshinski and B. A. Martin, 'Neural tissue motion impacts cerebrospinal fluid dynamics at the cervical medullary junction: A patient-specific moving-boundary computational model', *Annals of Biomedical Engineering*, vol. 43, pp. 2911–2923, 12 2015.

[82] R. Sacco, G. Guidoboni and A. G. Mauri, 'Mathematical and physical modeling principles of complex biological systems', in G. Guidoboni, A. Harris and R. Sacco, Eds. Springer International Publishing, 2019, pp. 3–20.

[83] W. Wakeland and B. Goldstein, 'A review of physiological simulation models of intracranial pressure dynamics', *Computers in Biology and Medicine*, vol. 38, pp. 1024–1041, 9 2008.

[84] A. Marmarou, K. Shulman and J. LaMorgese, 'Compartmental analysis of compliance and outflow resistance of the cerebrospinal fluid system', *Journal of Neurosurgery*, vol. 43, pp. 523–534, 5 1975.

[85] L. Geregele *et al.*, 'Dynamics of cerebrospinal fluid: From theoretical models to clinical applications', in K. Miller, Ed. Springer International Publishing, 2019, pp. 181–214.

[86] O. Hoffmann, 'Biomathematics of intracranial csf and haemodynamics. simulation and analysis with the aid of a mathematical model', in G. Csécsei, O. Hoffmann, N. Klug, A. Laun, R. Schönmayr and J. Zierski, Eds. Springer Vienna, 1987, pp. 117–130.

[87] M. Ursino, 'A mathematical study of human intracranial hydrodynamics part 1the cerebrospinal fluid pulse pressure', *Annals of Biomedical Engineering*, vol. 16, pp. 379–401, 4 1988.

[88] M. Czosnyka, S. Piechnik, H. K. Richards, P. Kirkpatrick, P. Smielewski and J. D. Pickard, 'Contribution of mathematical modelling to the interpretation of bedside tests of cerebrovascular autoregulation', *Journal of Neurology Neurosurgery and Psychiatry*, vol. 63, pp. 721–731, 6 1997.

[89] W. D. Lakin, S. A. Stevens, B. I. Tranmer and P. L. Penar, 'A whole-body mathematical model for intracranial pressure dynamics', *Journal of Mathematical Biology*, vol. 46, pp. 347–383, 4 2003.

[90] E. F. Toro *et al.*, 'Cerebrospinal fluid dynamics coupled to the global circulation in holistic setting: Mathematical models, numerical methods and applications', *International Journal for Numerical Methods in Biomedical Engineering*, vol. 38, 1 2022.

[91] A. A. Linninger, M. Xenos, B. Sweetman, S. Ponkshe, X. Guo and R. Penn, 'A mathematical model of blood, cerebrospinal fluid and brain dynamics', *Journal of Mathematical Biology*, vol. 59, pp. 729–759, 6 2009.

[92] C. D. Bertram, A. R. Brodbelt and M. A. Stoodley, 'The origins of syringomyelia: Numerical models of fluid/structure interactions in the spinal cord', *Journal of Biomechanical Engineering*, vol. 127, pp. 1099–1109, 7 2005.

[93] C. D. Bertram, L. E. Bilston and M. A. Stoodley, 'Tensile radial stress in the spinal cord related to arachnoiditis or tethering: A numerical model', *Medical and Biological Engineering and Computing*, vol. 46, pp. 701–707, 7 2008.

[94] C. D. Bertram, 'Evaluation by fluid/structure-interaction spinal-cord simulation of the effects of subarachnoid-space stenosis on an adjacent syrinx', *Journal of Biomechanical Engineering*, vol. 132, 6 2010.

[95] J. D. Anderson, 'Discretization of partial differential equations', in J. F. Wendt, Ed. Springer Berlin Heidelberg, 2009, pp. 87–104.

[96] H. K. Versteeg and W. Malalasekera, 'An introduction to computational fluid dynamics : the finite volume method', 2nd ed. Harlow, 2007.

[97] T. Krüger, H. Kusumaatmaja, A. Kuzmin, O. Shardt, G. Silva and E. M. Viggen, 'The lattice boltzmann equation', in T. Krüger, H. Kusumaatmaja, A. Kuzmin, O. Shardt, G. Silva and E. M. Viggen, Eds. Springer International Publishing, 2017, pp. 61–104.

[98] E. Jacobson, D. Fletcher, M. Morgan and I. Johnston, 'Fluid dynamics of the cerebral aqueduct', *Pediatric neurosurgery*, vol. 24, pp. 229–236, 1996.

[99] E. E. Jacobson, D. F. Fletcher, M. K. Morgan and I. H. Johnston, 'Computer modelling of the cerebrospinal fluid flow dynamics of aqueduct stenosis', *Medical and Biological Engineering and Computing*, vol. 37, pp. 59–63, 1 1999.

[100] L. Fin and R. Grebe, 'Three dimensional modeling of the cerebrospinal fluid dynamics and brain interactions in the aqueduct of sylvius', *Computer Methods in Biomechanics and Biomedical Engineering*, vol. 6, pp. 163–170, 3 2003, doi: 10.1080/1025584031000097933.

[101] V. Kurtcuoglu, D. Poulikakos and Y. Ventikos, 'Computational modeling of the mechanical behavior of the cerebrospinal fluid system', *Journal of Biomechanical Engineering*, vol. 127, pp. 264–269, 2 2004.

[102] V. Kurtcuoglu *et al.*, 'Computational investigation of subject-specific cerebrospinal fluid flow in the third ventricle and aqueduct of sylvius', *Journal of Biomechanics*, vol. 40, pp. 1235–1245, 6 2007.

[103] L. Howden *et al.*, 'Three-dimensional cerebrospinal fluid flow within the human ventricular system', *Computer Methods in Biomechanics and Biomedical Engineering*, vol. 11, pp. 123–133, 2 2008, doi: 10.1080/10255840701492118.

[104] B. Tully and Y. Ventikos, 'Coupling poroelasticity and cfd for cerebrospinal fluid hydrodynamics', *IEEE Transactions on Biomedical Engineering*, vol. 56, pp. 1644–1651, 6 2009.

[105] S. Cheng, K. Tan and L. E. Bilston, 'The effects of the interthalamic adhesion position on cerebrospinal fluid dynamics in the cerebral ventricles', *Journal of Biomechanics*, vol. 43, pp. 579–582, 3 2010.

[106] B. Siyahhan *et al.*, 'Flow induced by ependymal cilia dominates near-wall cerebrospinal fluid dynamics in the lateral ventricles', *Journal of The Royal Society Interface*, vol. 11, p. 20 131 189, 94 2014, doi: 10.1098/rsif.2013.1189.

[107] A. Farnoush, K. Tan, L. Juge, L. E. Bilston and S. Cheng, 'Effect of endoscopic third ventriculostomy on cerebrospinal fluid pressure in the cerebral ventricles', *Journal of Clinical Neuroscience*, vol. 23, pp. 63–67, 2016.

[108] J. C. Vardakis *et al.*, 'Investigating cerebral oedema using poroelasticity', *Medical Engineering and Physics*, vol. 38, pp. 48–57, 1 2016.

[109] P. Holmlund, S. Qvarlander, J. Malm and A. Eklund, 'Can pulsatile csf flow across the cerebral aqueduct cause ventriculomegaly? a prospective study of patients with communicating hydrocephalus', *Fluids and Barriers of the CNS*, vol. 16, p. 40, 1 2019.

[110] S. Gholampour and N. Fatouraee, 'Boundary conditions investigation to improve computer simulation of cerebrospinal fluid dynamics in hydrocephalus patients', *Communications Biology*, vol. 4, 1 2021.

[111] H. Yoshida *et al.*, 'Effect of cilia-induced surface velocity on cerebrospinal fluid exchange in the lateral ventricles', *Journal of The Royal Society Interface*, vol. 19, p. 20 220 321, 193 2022, doi: 10.1098/rsif.2022.0321.

[112] C. Bilgi, F. Amlani, H. Wei, N. Rizzi and N. M. Pahlevan, 'Thermal and postural effects on fluid mixing and irrigation patterns for intraventricular hemorrhage treatment', *Annals of Biomedical Engineering*, vol. 51, pp. 1270–1283, 6 2023.

[113] S. Maeda, T. Otani, S. Yamada, Y. Watanabe, S. Y. Ilik and S. Wada, 'Biomechanical effects of hyper-dynamic cerebrospinal fluid flow through the cerebral aqueduct in idiopathic normal pressure hydrocephalus patients', *Journal of Biomechanics*, vol. 156, p. 111 671, 2023.

[114] S. Gupta, M. Soellinger, P. Boesiger, D. Poulikakos and V. Kurtcuoglu, 'Three-dimensional computational modeling of subject-specific cerebrospinal fluid flow in the subarachnoid space', *Journal of Biomechanical Engineering*, vol. 131, 2 2009.

[115] S. Gupta *et al.*, 'Cerebrospinal fluid dynamics in the human cranial subarachnoid space: An overlooked mediator of cerebral disease. i. computational model', *Journal of The Royal Society Interface*, vol. 7, pp. 1195–1204, 49 2010, doi: 10.1098/rsif.2010.0033.

[116] A. Kuttler, T. Dimke, S. Kern, G. Helmlinger, D. Stanski and L. A. Finelli, 'Understanding pharmacokinetics using realistic computational models of fluid dynamics: Biosimulation of drug distribution within the csf space for intrathecal drugs', *Journal of Pharmacokinetics and Pharmacodynamics*, vol. 37, pp. 629–644, 6 2010.

[117] M. Khani *et al.*, 'Nonuniform moving boundary method for computational fluid dynamics simulation of intrathecal cerebrospinal flow distribution in a cynomolgus monkey', *Journal of Biomechanical Engineering*, vol. 139, 8 2017.

[118] E. K. Lindstrøm, J. Schreiner, G. A. Ringstad, V. Haughton, P. K. Eide and K.-A. Mardal, 'Comparison of phase-contrast mr and flow simulations for the study of csf dynamics in the cervical spine', *The Neuroradiology Journal*, vol. 31, pp. 292–298, 3 2018, doi: 10.1177/1971400918759812.

[119] S. Gholampour and M. Taher, 'Relationship of morphologic changes in the brain and spinal cord and disease symptoms with cerebrospinal fluid hydrodynamic changes in patients with chiari malformation type i', *World Neurosurgery*, vol. 116, e830–e839, 2018.

[120] M. Khani *et al.*, 'In vitro and numerical simulation of blood removal from cerebrospinal fluid: Comparison of lumbar drain to neurapheresis therapy', *Fluids and Barriers of the CNS*, vol. 17, 1 2020.

[121] K. Tangen, I. Nestorov, A. Verma, J. Sullivan, R. W. Holt and A. A. Linninger, 'In vivo intrathecal tracer dispersion in cynomolgus monkey validates wide biodistribution along neuraxis', *IEEE Transactions on Biomedical Engineering*, vol. 67, pp. 1122–1132, 4 2020.

[122] K. M. Tangen, Y. Hsu, D. C. Zhu and A. A. Linninger, 'Cns wide simulation of flow resistance and drug transport due to spinal microanatomy', *Journal of Biomechanics*, vol. 48, pp. 2144–2154, 10 2015.

[123] M. Khani *et al.*, 'Human in silico trials for parametric computational fluid dynamics investigation of cerebrospinal fluid drug delivery: Impact of injection location, injection protocol, and physiology', *Fluids and Barriers of the CNS*, vol. 19, 1 2022.

[124] 'Patient-specific computational fluid dynamic simulation of cerebrospinal fluid flow in the intracranial space', *Brain Research*, vol. 1790, 2022.

[125] A. A. Linninger, M. Xenos, D. C. Zhu, M. R. Somayaji, S. Kondapalli and R. D. Penn, 'Cerebrospinal fluid flow in the normal and hydrocephalic human brain', *IEEE Transactions on Biomedical Engineering*, vol. 54, pp. 291–302, 2 2007.

[126] Y. Hsu, H. D. M. Hettiarachchi, D. C. Zhu and A. A. Linninger, 'The frequency and magnitude of cerebrospinal fluid pulsations influence intrathecal drug distribution: Key factors for interpatient variability', *Anesthesia and Analgesia*, vol. 115, 2 2012.

[127] E. Abolfazli, N. Fatouraee and A. S. Seddighi, 'Effects of lumbar drainage on csf dynamics in subarachnoid hemorrhage condition: A computational study', *Computers in Biology and Medicine*, vol. 77, pp. 49–58, 2016.

[128] B. Sweetman and A. A. Linninger, 'Cerebrospinal fluid flow dynamics in the central nervous system', *Annals of Biomedical Engineering*, vol. 39, pp. 484–496, 1 2011.

[129] M. Causemann, V. Vinje and M. E. Rognes, 'Human intracranial pulsatility during the cardiac cycle: A computational modelling framework', *Fluids and Barriers of the CNS*, vol. 19, 1 2022.

[130] A. Roldan, O. Wieben, V. Haughton, T. Osswald and N. Chesler, 'Characterization of csf hydrodynamics in the presence and absence of tonsillar ectopia by means of computational flow analysis', *American Journal of Neuroradiology*, vol. 30, p. 941, 5 2009.

[131] G. Rutkowska, V. Haughton, S. Linge and K.-A. Mardal, 'Patient-specific 3d simulation of cyclic csf flow at the craniocervical region', *American Journal of Neuroradiology*, vol. 33, p. 1756, 9 2012.

[132] T. I. Yiallourou, J. R. Kröger, N. Stergiopulos, D. Maintz, B. A. Martin and A. C. Bunck, 'Comparison of 4d phase-contrast mri flow measurements to computational fluid dynamics simulations of cerebrospinal fluid motion in the cervical spine', *PLOS ONE*, vol. 7, e52284–, 12 2012.

[133] E. C. Clarke, D. F. Fletcher, M. A. Stoodley and L. E. Bilston, 'Computational fluid dynamics modelling of cerebrospinal fluid pressure in chiari malformation and syringomyelia', *Journal of Biomechanics*, vol. 46, pp. 1801–1809, 11 2013.

[134] K. H. Støverud, H. P. Langtangen, G. A. Ringstad, P. K. Eide and K. A. Mardal, 'Computational investigation of cerebrospinal fluid dynamics in the posterior cranial fossa and cervical subarachnoid space in patients with chiari i malformation', *PLoS ONE*, vol. 11, 10 2016.

[135] R. A. Lloyd, D. F. Fletcher, E. C. Clarke and L. E. Bilston, 'Chiari malformation may increase perivascular cerebrospinal fluid flow into the spinal cord: A subject-specific computational modelling study', *Journal of Biomechanics*, vol. 65, pp. 185–193, 2017.

[136] B. A. Martin, W. Kalata, N. Shaffer, P. Fischer, M. Luciano and F. Loth, 'Hydrodynamic and longitudinal impedance analysis of cerebrospinal fluid dynamics at the craniovertebral junction in type i chiari malformation', *PLoS ONE*, vol. 8, 10 2013.

[137] N. Shaffer *et al.*, 'Cerebrospinal fluid flow impedance is elevated in type i chiari malformation', *Journal of Biomechanical Engineering*, vol. 136, 2 2014.

[138] B. A. Martin *et al.*, 'Inter-operator reliability of magnetic resonance image-based computational fluid dynamics prediction of cerebrospinal fluid motion in the cervical spine', *Annals of Biomedical Engineering*, vol. 44, pp. 1524–1537, 5 2016.

[139] A. Ibrahimy, C. W. C. Huang, A. F. Bezuidenhout, P. A. Allen, R. A. Bhadelia and F. Loth, 'Association between resistance to cerebrospinal fluid flow near the foramen magnum and cough-associated headache in adult chiari malformation type i', *Journal of Biomechanical Engineering*, vol. 143, 5 2021.

[140] K. Berkouk, P. W. Carpenter and A. D. Lucey, 'Pressure wave propagation in fluid-filled co-axial elastic tubes part 1: Basic theory', *Journal of Biomechanical Engineering*, vol. 125, pp. 852–856, 6 2004.

[141] B. A. Martin and F. Loth, 'The influence of coughing on cerebrospinal fluid pressure in an in vitro syringomyelia model with spinal subarachnoid space stenosis', *Cerebrospinal Fluid Research*, vol. 6, p. 17, 1 2009.

[142] S. Vandenbulcke, T. D. Pauw, F. Dewaele, J. Degroote and P. Segers, 'Computational fluid dynamics model to predict the dynamical behavior of the cerebrospinal fluid through implementation of physiological boundary conditions', *Frontiers in Bioengineering and Biotechnology*, vol. 10, 2022.

[143] A. Benninghaus, O. Balédent, A. Lokossou, C. Castelar, S. Leonhardt and K. Radermacher, 'Enhanced in vitro model of the csf dynamics', *Fluids and Barriers of the CNS*, vol. 16, 1 2019.

[144] L. Chen, G. Elias, M. P. Yostos, B. Stimec, J. Fasel and K. Murphy, 'Pathways of cerebrospinal fluid outflow: A deeper understanding of resorption', *Neuroradiology*, vol. 57, pp. 139–147, 2 2015.

[145] N. Westerhof, J. W. Lankhaar and B. E. Westerhof, *The arterial windkessel*, 2009.

[146] N. Xiao, J. Alastruey and C. A. Figueroa, 'A systematic comparison between 1-d and 3-d hemodynamics in compliant arterial models', *International Journal for Numerical Methods in Biomedical Engineering*, vol. 30, pp. 204–231, 2 2014.

[147] S. Annerel, J. Degroote, T. Claessens and J. Vierendeels, 'Evaluation of a new implicit coupling algorithm for the partitioned fluid-structure interaction simulation of bileaflet mechanical heart valves', *IOP Conference Series: Materials Science and Engineering*, vol. 10, p. 012 124, 1 2010.

[148] V. Singh and R. Cheng, 'Neurovascular physiology and neurocritical care', in Elsevier B.V., 2021, vol. 176, pp. 71–80.

[149] P. K. Eide and E. Kerty, 'Static and pulsatile intracranial pressure in idiopathic intracranial hypertension', *Clinical Neurology and Neurosurgery*, vol. 113, pp. 123–128, 2 2011.

[150] G. Portella *et al.*, 'Continuous cerebral compliance monitoring in severe head injury: Its relationship with intracranial pressure and cerebral perfusion pressure', *Acta Neurochirurgica*, vol. 147, pp. 707–713, 7 2005.

[151] P. K. Eide, 'The correlation between pulsatile intracranial pressure and indices of intracranial pressure-volume reserve capacity: Results from ventricular infusion testing', *Journal of Neurosurgery*, vol. 125, pp. 1493–1503, 6 2016.

[152] M. E. Wagshul, P. K. Eide and J. R. Madsen, 'The pulsating brain: A review of experimental and clinical studies of intracranial pulsatility', *Fluids and Barriers of the CNS*, vol. 8, p. 5, 1 2011.

[153] 'Guidelines for the management of severe traumatic brain injury, fourth edition', *Neurosurgery*, vol. 80, pp. 6–15, 1 2017.

[154] *Guidelines for the management of severe traumatic brain injury: 2020 update of the decompressive craniectomy recommendations*, 2020.

[155] P. K. Eide, L. M. Valnes, E. K. Lindstrøm, K.-A. Mardal and G. Ringstad, 'Direction and magnitude of cerebrospinal fluid flow vary substantially across central nervous system diseases', *Fluids and Barriers of the CNS*, vol. 18, p. 16, 1 2021.

[156] V. Vinje *et al.*, 'Respiratory influence on cerebrospinal fluid flow  a computational study based on long-term intracranial pressure measurements', *Scientific Reports*, vol. 9, 1 2019.

[157] D. Greitz, 'Radiological assessment of hydrocephalus: New theories and implications for therapy', *Neurosurgical Review*, vol. 27, pp. 145–165, 3 2004.

[158] G. A. Bateman and S. H. Siddique, 'Cerebrospinal fluid absorption block at the vertex in chronic hydrocephalus: Obstructed arachnoid granulations or elevated venous pressure?', *Fluids and Barriers of the CNS*, vol. 11, 1 2014.

[159] V. Leinonen, R. Vanninen and T. Rauramaa, 'Cerebrospinal fluid circulation and hydrocephalus', in Elsevier B.V., 2018, vol. 145, pp. 39–50.

[160] G. H. du Boulay, 'Pulsatile movements in the csf pathways*', *British Journal of Radiology*, vol. 39, pp. 255–262, 460 1966.

[161] J. E. A. O'CONNELL, 'The vascular factor tn intracranial pressure and the maintenance of the cerebrospinal fluid circulation1', *Brain*, vol. 66, pp. 204–228, 3 1943.

[162] K. TAKIZAWA *et al.*, 'The choroid plexus of the lateral ventricle as the origin of csf pulsation is questionable', *Neurologia medico-chirurgica*, vol. 58, pp. 23–31, 1 2018.

[163] M. Soellinger, A. K. Rutz, S. Kozerke and P. Boesiger, '3d cine displacement-encoded mri of pulsatile brain motion', *Magnetic Resonance in Medicine*, vol. 61, pp. 153–162, 1 2009.

[164] S. J. Holdsworth, M. S. Rahimi, W. W. Ni, G. Zaharchuk and M. E. Moseley, 'Amplified magnetic resonance imaging (amri)', *Magnetic Resonance in Medicine*, vol. 75, pp. 2245–2254, 6 2016.

[165] I. Terem *et al.*, '3d amplified mri (amri)', *Magnetic Resonance in Medicine*, vol. 86, pp. 1674–1686, 3 2021.

[166] I. Terem *et al.*, 'Revealing sub-voxel motions of brain tissue using phase-based amplified mri (amri)', *Magnetic Resonance in Medicine*, vol. 80, pp. 2549–2559, 6 2018.

[167] J. Abderezaei *et al.*, 'Increased hindbrain motion in chiari malformation i patients measured through 3d amplified mri (3d amri)', *medRxiv*, p. 2022.10.25.22281481, 2022.

[168] N. Delaissé, T. Demeester, D. Fauconnier and J. Degroote, 'Surrogate-based acceleration of quasi-newton techniques for fluid-structure interaction simulations', *Computers and Structures*, vol. 260, p. 106 720, 2022.

[169] N. Delaissé, T. Demeester, R. Haelterman and J. Degroote, 'Quasi-newton methods for partitioned simulation of fluidstructure interaction reviewed in the generalized broyden framework', *Archives of Computational Methods in Engineering*, vol. 30, pp. 3271–3300, 5 2023.

[170] V. Kurtcuoglu, M. Soellinger, P. Summers, D. Poulikakos and P. Boesiger, 'Mixing and modes of mass transfer in the third cerebral ventricle: A computational analysis', *Journal of Biomechanical Engineering*, vol. 129, pp. 695–702, 5 2007.

[171] E. C. Clarke, M. A. Stoodley and L. E. Bilston, 'Changes in temporal flow characteristics of csf in chiari malformation type i with and without syringomyelia: Implications for theory of syrinx development - clinical article', *Journal of Neurosurgery*, vol. 118, pp. 1135–1140, 5 2013.

[172] S. Vandenbulcke, P. Condron, S. Safaei, S. Holdsworth, J. Degroote and P. Segers, 'A computational fluid dynamics study to assess the impact of coughing on cerebrospinal fluid dynamics in chiari type 1 malformation', *Scientific Reports*, vol. 14, p. 12 717, 1 2024.

[173] K. Jain, G. Ringstad, P. K. Eide and K. A. Mardal, 'Direct numerical simulation of transitional hydrodynamics of the cerebrospinal fluid in chiari i malformation: The role of craniovertebral junction', *International Journal for Numerical Methods in Biomedical Engineering*, vol. 33, 9 2017.

[174] S. Gholampour and H. Gholampour, 'Correlation of a new hydrodynamic index with other effective indexes in chiari i malformation patients with different associations', *Scientific Reports*, vol. 10, p. 15 907, 1 2020.

[175] S. Cheng, M. A. Stoodley, J. Wong, S. Hemley, D. F. Fletcher and L. E. Bilston, 'The presence of arachnoiditis affects the characteristics of csf flow in the spinal subarachnoid space: A modelling study', *Journal of Biomechanics*, vol. 45, pp. 1186–1191, 7 2012.

[176] S. O. Linge, V. Haughton, A. E. Løvgren, K. A. Mardal, A. Helgeland and H. P. Langtangen, 'Effect of tonsillar herniation on cyclic csf flow studied with computational flow analysis', *American Journal of Neuroradiology*, vol. 32, pp. 1474–1481, 8 2011.

[177] K. H. Støverud, H. P. Langtangen, V. Haughton and K.-A. Mardal, 'Csf pressure and velocity in obstructions of the subarachnoid spaces', *The Neuroradiology Journal*, vol. 26, pp. 218–226, 2 2013.

[178] S. Dreha-Kulaczewski, A. A. Joseph, K.-D. Merboldt, H.-C. Ludwig, J. Gärtner and J. Frahm, 'Identification of the upward movement of human csf in vivo and its relation to the brain venous system', *The Journal of Neuroscience*, vol. 37, p. 2395, 9 2017.

[179] P. L. Roux *et al.*, 'Consensus summary statement of the international multidisciplinary consensus conference on multimodality monitoring in neurocritical care', *Intensive Care Medicine*, vol. 40, pp. 1189–1209, 9 2014.

[180] G. N. Ocamoto *et al.*, 'Intracranial compliance concepts and assessment: A scoping review', *Frontiers in Neurology*, vol. 12, 2021.

[181] S. Gholampour, 'Why intracranial compliance is not utilized as a common practical tool in clinical practice', *Biomedicines*, vol. 11, no. 11, 2023.

[182] S. Annerel *et al.*, 'A fast strong coupling algorithm for the partitioned fluid-structure interaction simulation of bmhvs', *Computer Methods in Biomechanics and Biomedical Engineering*, vol. 15, pp. 1281–1312, 12 2012.